EUROPEAN ORGANISATION FOR NUCLEAR RESEARCH (CERN)

Submitted to: JHEP

CERN-EP-2021-217
21st January 2022

Measurements of Higgs boson production cross-sections in the $H \to \tau^+\tau^-$ decay channel in pp collisions at $\sqrt{s} = 13$ TeV with the ATLAS detector

The ATLAS Collaboration

Measurements of the production cross-sections of the Standard Model (SM) Higgs boson (H) decaying into a pair of τ-leptons are presented. The measurements use data collected with the ATLAS detector from pp collisions produced at the Large Hadron Collider at a centre-of-mass energy of $\sqrt{s} = 13$ TeV, corresponding to an integrated luminosity of 139 fb^{-1}. Leptonic ($\tau \to \ell\nu_\ell\nu_\tau$) and hadronic ($\tau \to$ hadrons ν_τ) decays of the τ-lepton are considered. All measurements account for the branching ratio of $H \to \tau\tau$ and are performed with a requirement $|y_H| < 2.5$, where y_H is the true Higgs boson rapidity. The cross-section of the $pp \to H \to \tau\tau$ process is measured to be $2.94 \pm 0.21(\text{stat})^{+0.37}_{-0.32}(\text{syst})$ pb, in agreement with the SM prediction of 3.17 ± 0.09 pb. Inclusive cross-sections are determined separately for the four dominant production modes: $2.65 \pm 0.41(\text{stat})^{+0.91}_{-0.67}(\text{syst})$ pb for gluon–gluon fusion, $0.197 \pm 0.028(\text{stat})^{+0.032}_{-0.026}(\text{syst})$ pb for vector-boson fusion, $0.115 \pm 0.058(\text{stat})^{+0.042}_{-0.040}(\text{syst})$ pb for vector-boson associated production, and $0.033 \pm 0.031(\text{stat})^{+0.022}_{-0.017}(\text{syst})$ pb for top-quark pair associated production. Measurements in exclusive regions of the phase space, using the simplified template cross-section framework, are also performed. All results are in agreement with the SM predictions.

Contents

1 Introduction

A particle consistent with the Standard Model (SM) Higgs boson [1–6] was discovered in 2012 by the ATLAS and CMS collaborations [7, 8] from the analysis of proton–proton (pp) collisions produced by the Large Hadron Collider (LHC) [9]. Since then, the analysis of data collected at centre-of-mass energies of 7 TeV, 8 TeV and 13 TeV in Runs 1 and 2 of the LHC[1] has led to the precise measurement of the Higgs boson mass, $m_H = 125.09\,\text{GeV}$ [10], and to the observation and measurement of the four main production modes (gluon–gluon fusion, vector-boson fusion, and associated production with either a weak gauge boson or a pair of top quarks) and of several decay channels of the Higgs boson predicted by the SM [11–25].

The decay into a $\tau^+\tau^-$ pair[2] has the largest branching fraction of all leptonic Higgs boson decays (6.3% [26, 27] for a mass of $m_H = 125.09\,\text{GeV}$). The large number of Higgs boson decays into $\tau\tau$ produced at the LHC ($\approx 500 \cdot 10^3$ during Run 2) offers a unique opportunity to study the Yukawa mechanism in detail. Measurements in this final state are, however, complicated at the experimental level, as the presence of two to four neutrinos[3] in the final state significantly degrades the resolution of the measured Higgs boson four-momentum, rendering the separation between the signal and the large background from $Z \to \tau\tau$ events difficult. This effect can be mitigated through the dedicated study of the Higgs production modes where the event topology differs drastically from that of Z + jets events, the two most sensitive being the production of the Higgs boson through vector-boson fusion (VBF) and its production through gluon–gluon fusion (ggF) with Higgs boson produced with a large transverse momentum.

The first evidence of the $\tau\tau$ decay of the Higgs boson was obtained by the ATLAS [28] and CMS [29] collaborations using data collected at centre-of-mass energies of 7 TeV and 8 TeV during Run 1 of the LHC. The combination [21] of these two results led to the first observation of the $\tau\tau$ decay of the Higgs boson. More recent measurements in the $H \to \tau\tau$ decay channel are documented in Refs. [30–32].

This paper presents measurements of the Higgs boson decaying into a di-τ pair with the ATLAS detector, using the full Run 2 LHC dataset. The $pp \to H \to \tau\tau$ process is measured inclusively, in the four dominant production modes simultaneously, and as a function of key properties of the event. This is achieved with an optimised categorisation of the collected events. Three di-τ final states are targeted: two hadronically decaying τ-leptons (τ_{had}, where the tau decays into hadrons plus a neutrino), denoted $\tau_{\text{had}}\tau_{\text{had}}$; one leptonically decaying τ-lepton (τ_{lep}) and one τ_{had}, denoted $\tau_{\text{lep}}\tau_{\text{had}}$;[4] and two τ_{lep} with different flavours, denoted $\tau_e\tau_\mu$. The remaining final states, with two same-flavour light leptons ($\tau_e\ \tau_e$ and $\tau_\mu\ \tau_\mu$), are not considered due to large uncertainties in $Z \to ee$ and $Z \to \mu\mu$ contributions to the expected background. The dominant background processes after the event selection are $Z \to \tau\tau$ decays, $t\bar{t}$ production, and processes with at least one jet misreconstructed as a τ_{had}. Smaller contributions to the background arise from events with $Z \to \ell\ell$ decays, two weak vector bosons VV (diboson), and $H \to WW^*$ decays. Templates of the estimated invariant mass of the $\tau\tau$ pairs are built for each process in the signal regions (SR) defined by the event selection and categorisation. The templates are used as input to a binned maximum-likelihood fit which allows the yields and kinematics of both the signal and the background processes to be measured. Control regions (CR) enter the fit as event counts and help determine the normalisation of the main backgrounds as well as constrain their uncertainties.

[1] Run 1 signifies the LHC data-taking period in the years 2010–2012 and Run 2 the one in 2015–2018.

[2] For simplicity, a $\tau^+\tau^-$ pair is denoted by $\tau\tau$ or di-τ throughout the paper.

[3] The number of neutrinos depends on the decay modes of the two τ-leptons.

[4] The $\tau_{\text{lep}}\tau_{\text{had}}$ categories can be split into $\tau_e\tau_{\text{had}}$ and $\tau_\mu\tau_{\text{had}}$ when distinguishing the light lepton's flavour is appropriate.

This work uses 139 fb^{-1} of pp collision data collected at a centre-of-mass energy of 13 TeV, to be compared with 36 fb^{-1} for the previous $H \to \tau\tau$ cross-section measurements [22]. It introduces a new reconstructed-event categorisation designed for the improved *stage 1.2* binning [33] of the simplified template cross-section (STXS) framework [27]. The treatment of ggF events with Higgs boson produced with a large transverse momentum is refined with three times more categories. Selected events are categorised with requirements on the transverse momentum of the reconstructed Higgs boson candidate ($p_{\mathrm{T}}(H)$) and on the potential additional hadronic jets. Two new categories targeting production modes where the Higgs boson is created in association with other objects are added, based on requirements on the kinematics and tagged flavour of the jets in the event. The first targets the production of a Higgs boson in association with a pair of top quarks ($t\bar{t}H$), where both top quarks and both τ-leptons decay hadronically, complementing the explorations in Ref. [34], and is denoted by $\mathrm{tt}(0\ell)H \to \tau_{\mathrm{had}}\tau_{\mathrm{had}}$ in the rest of this paper.[5] The second targets the production of a Higgs boson in association with a vector boson V (W, Z). This new category, referred to as V(had)H, focuses on events with a hadronic decay of the V boson while the production of $Z(\to \ell\ell)H$ and $W(\to \ell\nu)H$ events is studied separately [35]. Finally, the selection of VBF events was also improved by multivariate techniques.

In addition to the new extended categorisation, several improvements to the analysis methodology have been implemented: the object selection has been improved, multivariate discriminants have been optimised to enhance the purity of the SRs in the targeted Higgs boson production modes, the number of simulated background events has been increased significantly and the usage of the $Z \to \ell\ell$ control region has been refined. The latter relies on a new simplified implementation of the embedding technique [36, 37] which, instead of replacing the reconstructed electrons and muons from $Z \to \ell\ell$ events by equivalent simulated τ-lepton decay products, simply rescales their transverse momentum to that of an equivalent τ-lepton.

This document is organised as follows. Section 2 describes the ATLAS detector. This is followed in Section 3 by a description of the dataset and Monte Carlo (MC) simulated samples employed in the measurement. Section 4.1 details the reconstruction of the physics objects. The event selection and categorisation is described in Section 4.2. In Section 5, the estimation of the background processes is discussed with an emphasis on the simplified embedding technique to model $Z \to \tau\tau$ processes in Section 5.1 and the data-driven estimates of the processes with at least one jet misidentified as an electron, a muon or a τ_{had} in Section 5.2. Section 6 presents the systematic uncertainties affecting the measurement and their estimation. The details of the signal extraction fit are discussed in Section 7, and Section 8 presents the results of the measurement. Section 9 summarises the conclusions of this work.

2 The ATLAS detector

The ATLAS detector [38] at the LHC covers nearly the entire solid angle around the collision point.[6] It consists of an inner tracking detector surrounded by a thin superconducting solenoid, electromagnetic and hadron calorimeters, and a muon spectrometer incorporating three large superconducting air-core toroidal magnets.

[5] In this document, $\ell = e, \mu$. Therefore, 0ℓ indicates the absence of electrons or muons selected in the event.

[6] ATLAS uses a right-handed coordinate system with its origin at the nominal interaction point (IP) in the centre of the detector and the z-axis along the beam pipe. The x-axis points from the IP to the centre of the LHC ring, and the y-axis points upwards. Cylindrical coordinates (r, ϕ) are used in the transverse plane, ϕ being the azimuthal angle around the z-axis. The pseudorapidity is defined in terms of the polar angle θ as $\eta = -\ln\tan(\theta/2)$. Angular distance is measured in units of $\Delta R \equiv \sqrt{(\Delta\eta)^2 + (\Delta\phi)^2}$.

The inner-detector system (ID) is immersed in a 2 T axial magnetic field and provides charged-particle tracking in the range $|\eta| < 2.5$. The high-granularity silicon pixel detector covers the vertex region and typically provides four measurements per track, the first hit normally being in the insertable B-layer installed before Run 2 [39, 40]. It is followed by the silicon microstrip tracker, which usually provides eight measurements per track. These silicon detectors are complemented by the transition radiation tracker (TRT), which enables radially extended track reconstruction up to $|\eta| = 2.0$. The TRT also provides electron identification information based on the fraction of hits (typically 30 in total) above a higher energy-deposit threshold corresponding to transition radiation.

The calorimeter system covers the pseudorapidity range $|\eta| < 4.9$. Within the region $|\eta| < 3.2$, electromagnetic calorimetry is provided by barrel and endcap high-granularity lead/liquid-argon (LAr) calorimeters, with an additional thin LAr presampler covering $|\eta| < 1.8$ to correct for energy loss in material upstream of the calorimeters. Hadron calorimetry is provided by the steel/scintillator-tile calorimeter, segmented into three barrel structures within $|\eta| < 1.7$, and two copper/LAr hadron endcap calorimeters. The solid angle coverage is completed with forward copper/LAr and tungsten/LAr calorimeter modules optimised for electromagnetic and hadronic energy measurements respectively.

The muon spectrometer (MS) comprises separate trigger and high-precision tracking chambers measuring the deflection of muons in a magnetic field generated by the superconducting air-core toroidal magnets. The field integral of the toroids ranges between 2.0 and 6.0 T m across most of the detector. A set of precision chambers covers the region $|\eta| < 2.7$ with three layers of monitored drift tubes, complemented by cathode-strip chambers in the forward region, where the background is highest. The muon trigger system covers the range $|\eta| < 2.4$ with resistive-plate chambers in the barrel, and thin-gap chambers in the endcap regions.

Interesting events are selected by the first-level (L1) trigger system implemented in custom hardware, followed by selections made by algorithms implemented in software in the high-level trigger [41]. The first-level trigger accepts events from the 40 MHz bunch crossings at a rate below 100 kHz, which the high-level trigger reduces in order to record events to disk at about 1 kHz.

An extensive software suite [42] is used in the reconstruction and analysis of real and simulated data, in detector operations, and in the trigger and data acquisition systems of the experiment.

3 Data and simulated event samples

The data used in this analysis were collected using unprescaled single-lepton, dilepton or di-τ triggers [43–46] at a centre-of-mass energy of 13 TeV during the 2015–2018 LHC running periods. Events are selected for analysis only if they are of good quality and if all the relevant detector components are known to have been in good operating condition [47], which corresponds to a total integrated luminosity of 139.0 fb^{-1}.

MC simulated events are used to model most of the backgrounds from SM processes and the $H \to \tau\tau$ signal processes. A summary of all the generators used for the simulation of the signal and background processes is shown in Table 1. The same event generators as in Ref. [22] were used, but the number of simulated events in each sample was at least quadrupled, which is the factor by which the integrated luminosity grew since the previous publication. In addition, the total number of simulated $Z \to \tau\tau$ events was increased by a further factor of approximately four. This computationally expensive task helps to densely populate the phase space where $Z \to \tau\tau$ events are produced in association with several jets.

All samples of simulated events were processed through the ATLAS detector simulation [48] based on GEANT4 [49]. The effects of multiple interactions in the same and nearby bunch crossings (pile-up) were modelled by overlaying minimum-bias events, simulated using the soft QCD processes of PYTHIA 8.186 [50] with the A3 [51] set of tuned parameters and NNPDF2.3LO [52] parton distribution functions (PDF).

The decays and spin correlations for τ-leptons are handled by SHERPA for the samples it generated, and by PYTHIA for the other MC event generators. The decays and spin correlations have been included in PYTHIA version 8.150 [53], and have been thoroughly validated by comparisons with TAUOLA [54].

Table 1: Overview of the MC generators used for the main signal and background samples. The last column, labelled 'Normalisation', specifies the order of the cross-section calculation used for the normalisation of the simulated samples.

Process	Generator		PDF set		Tune	Normalisation
	ME	PS	ME	PS		
Higgs boson						
ggF	POWHEG BOX v2	PYTHIA 8	PDF4LHC15NNLO	CTEQ6L1	AZNLO	N^{3}LO QCD + NLO EW
VBF	POWHEG BOX v2	PYTHIA 8	PDF4LHC15NLO	CTEQ6L1	AZNLO	NNLO QCD + NLO EW
VH	POWHEG BOX v2	PYTHIA 8	PDF4LHC15NLO	CTEQ6L1	AZNLO	NNLO QCD + NLO EW
$t\bar{t}H$	POWHEG BOX v2	PYTHIA 8	NNPDF3.0NNLO	NNPDF2.3LO	A14	NLO QCD + NLO EW
tH	MADGRAPH5_aMC@NLO	PYTHIA 8	CT10	NNPDF2.3LO	A14	NLO
$b\bar{b}H$	POWHEG BOX v2	PYTHIA 8	NNPDF3.0NNLO	NNPDF2.3LO	A14	NLO
Background						
V + jets (QCD/EW)	SHERPA 2.2.1		NNPDF3.0NNLO		SHERPA	NNLO for QCD, LO for EW
$t\bar{t}$	POWHEG BOX v2	PYTHIA 8	NNPDF3.0NNLO	NNPDF2.3LO	A14	NNLO + NNLL
Single top	POWHEG BOX v2	PYTHIA 8	NNPDF3.0NNLO	NNPDF2.3LO	A14	NLO
Diboson	SHERPA 2.2.1		NNPDF3.0NNLO		SHERPA	NLO

3.1 Higgs boson simulation samples

The main Higgs boson production mode at the LHC is ggF with a total expected cross-section of 48.6 pb, followed by VBF (3.78 pb), associated VH (2.25 pb), associated $b\bar{b}H$ (0.64 pb) and $t\bar{t}H$ (0.51 pb) production. Simulated event samples for these production modes were generated using POWHEG BOX v2 [55–59]. The tH process was also considered, but with a cross-section of 0.092 pb its expected contribution was found to be negligible. It was simulated with the MADGRAPH5_aMC@NLO 2.6.2 [60] generator.

For the ggF sample the PDF4LHC15NNLO PDF set [61] was used, while VBF and VH production samples used the PDF4LHC15NLO PDF set. The $t\bar{t}H$ and $b\bar{b}H$ events were produced with the NNPDF3.0NLO PDF set [62], and tH events with the CT10 PDF set [63]. Parton shower (PS) and non-perturbative effects were modelled with PYTHIA 8.230 [64] with parameter values set according to the AZNLO tune [65], except for $t\bar{t}H$, $b\bar{b}H$ and tH events, which rely on the A14 tune [66].

Higgs boson production via gluon–gluon fusion was simulated at next-to-next-to-leading-order (NNLO) accuracy in QCD. The simulation achieves NNLO accuracy for arbitrary inclusive $gg \to H$ observables by reweighting the Higgs boson rapidity spectrum in HJ-MINLO [67–69] to that of HNNLO [70]. The gluon–gluon fusion prediction from the MC simulated samples is normalised to the next-to-next-to-next-to-leading-order (N^{3}LO) cross-section in QCD plus electroweak (EW) corrections at next-to-leading order (NLO) [27, 71–80].

Higgs boson production via vector-boson fusion was simulated at NLO accuracy in QCD. It is tuned to match calculations with effects due to finite heavy-quark masses and soft-gluon resummations up to next-to-next-to-leading logarithms (NNLL). The prediction from the MC simulated samples is normalised to an approximate-NNLO QCD cross-section with NLO electroweak corrections [81–83].

Higgs boson production in association with a vector boson was simulated at next-to-leading order accuracy for VH plus one-jet production. The loop-induced $gg \to ZH$ process was generated separately at leading order in QCD. The prediction from the MC simulated sample is normalised to cross-sections calculated at NNLO in QCD with NLO electroweak corrections for $pp \to VH$ and at NLO and next-to-leading-logarithm accuracy in QCD for $gg \to ZH$ [84–90].

The production of $t\bar{t}H$ events was simulated at NLO accuracy in QCD. The decays of bottom and charm hadrons were performed by EvtGen 1.6.0 [91]. The cross-section used to normalise the $t\bar{t}H$ process is calculated at NLO in QCD and electroweak couplings [27, 92–95]. The production of $b\bar{b}H$ and tH events was simulated at NLO. The prediction from the MC simulated samples is normalised to cross-sections calculated at NLO in QCD [96–98].

The normalisation of all Higgs boson samples accounts for the decay branching ratio calculated with HDECAY [26, 99, 100] and Prophecy4f [101–103]. A Higgs boson mass of 125.09 GeV is assumed in the calculation of the expected cross-sections throughout this measurement.

3.2 Background processes simulation samples

The QCD production of V + jets events was simulated with the Sherpa 2.2.1 [104] generator using NLO matrix elements for up to two partons, and LO matrix elements for up to four partons, calculated with the Comix [105] and OpenLoops [106–108] libraries. They were matched with the Sherpa parton shower [109] using the MEPS@NLO prescription [110–113] using the set of tuned parameters developed by the Sherpa authors. The NNPDF3.0nnlo set of PDFs [62] was used and the samples are normalised to a NNLO prediction [114].

Electroweak production of $\ell\ell jj$, $\ell\nu jj$ and $\nu\nu jj$ final states was generated with Sherpa 2.2.1, using LO matrix elements with up to two additional parton emissions. The matrix elements were merged with the Sherpa parton shower following the MEPS@LO prescription and using the set of tuned parameters developed by the Sherpa authors. Similarly to the QCD V + jets processes, the NNPDF3.0nnlo set of PDFs was employed. The samples were produced using the VBF approximation, which avoids an overlap with semileptonic diboson topologies by requiring a t-channel colour-singlet exchange. They are normalised using the Sherpa cross-section predictions.

QCD and electroweak predictions for V + jets events are grouped in the analysis and collectively referred to as V + jets in the rest of the paper.

The production of $t\bar{t}$ events was modelled by the Powheg Box v2 generator at NLO with the NNPDF3.0nlo PDF set and the h_{damp} parameter[7] set to $1.5\,m_{\text{top}}$ [115]. The events were interfaced to Pythia 8.230 to model the parton shower, hadronisation, and underlying event, with parameters set according to the A14 tune and using the NNPDF2.3lo set of PDFs. The decays of bottom and charm hadrons were performed by

[7] The h_{damp} parameter is a resummation damping factor and one of the parameters that controls the matching of Powheg matrix elements to the parton shower and thus effectively regulates the high-p_{T} radiation against which the $t\bar{t}$ system recoils.

EvtGen as for the $t\bar{t}H$ sample. The $t\bar{t}$ sample is normalised to the cross-section prediction at NNLO in QCD including the resummation of NNLL soft-gluon terms calculated using Top++ 2.0 [116–122].

Single-top s-channel (t-channel) production was modelled using the Powheg Box v2 [55–58] generator at NLO in QCD in the five-flavour (four-flavour) scheme with the NNPDF3.0nlo set of PDFs [62]. The events were interfaced with Pythia 8.230 [64] using the A14 tune [66] and the NNPDF2.3lo PDF set. The sample is normalised to the theory prediction calculated at NLO in QCD with Hathor 2.1 [123, 124].

Diboson production was simulated with the Sherpa 2.2.1 or 2.2.2 generator depending on the process. Fully leptonic final states and semileptonic final states, where one boson decays leptonically and the other hadronically, were generated using matrix elements at NLO accuracy in QCD for up to one additional parton and at LO accuracy for up to three additional parton emissions. Samples for the loop-induced processes $gg \to VV$ were generated using LO-accurate matrix elements for up to one additional parton emission for both the fully leptonic and semileptonic final states. The matrix element calculations were matched and merged with the Sherpa parton shower based on Catani–Seymour dipole factorisation [105, 109] using the MEPS@NLO prescription. The virtual QCD corrections were provided by the OpenLoops library. The NNPDF3.0nnlo set of PDFs was used [62], along with the dedicated set of tuned parton-shower parameters developed by the Sherpa authors. The samples are normalised to a NLO prediction [125].

The background originating from $H \to WW^*$ decays was modelled using the same simulation strategy as the $H \to \tau\tau$ signal.

4 Object and event selection

The topology of $H \to \tau\tau$ events requires the reconstruction of electrons, muons, visible products of hadronically decaying τ-leptons ($\tau_{\text{had-vis}}$), jets (along with their b-tagging properties) and missing transverse momentum. The numbers of reconstructed electrons, muons and $\tau_{\text{had-vis}}$ in each event are used to define the different channels of the analysis. Requirements on the number of additional jets in the event are used in the signal region categorisation and to suppress backgrounds.

4.1 Object reconstruction

Tracks measured in the ID are used to reconstruct interaction vertices [126], of which the one with the highest sum of squared transverse momenta of the associated tracks is selected as the primary vertex of the hard interaction.

Electrons are reconstructed from topological clusters of energy deposits in the electromagnetic calorimeter which are matched to a track reconstructed in the ID [127]. They are required to satisfy the 'Loose' identification criteria, to have $p_{\text{T}} > 15$ GeV, and to be in the fiducial volume of the ID and the high-granularity electromagnetic calorimeters, $|\eta_{\text{cluster}}| < 2.47$. The transition region between the barrel and endcap calorimeters ($1.37 < |\eta_{\text{cluster}}| < 1.52$) is excluded except for the $Z \to \ell\ell$ control region where it is kept to facilitate the embedding procedure (see Section 5.1). In the $\tau_e\tau_\mu$ and $\tau_e\tau_{\text{had}}$ channels, the selected electron is further required to satisfy the 'Medium' identification, which has an associated efficiency of 80% to 90%, and the 'Loose' isolation criterion [127] in the signal regions and most control regions, which has an efficiency of 90% for 15 GeV candidates, increasing to more than 98% for 30 GeV candidates. In the $\tau_e\tau_{\text{had}}$ channel, the requirement on the electron transverse momentum is further tightened by 1 GeV above

the nominal trigger p_{T} threshold for electrons matched to the single-electron trigger to ensure operation at the trigger's plateau efficiency. Similarly, in the $\tau_e\tau_\mu$ channel, the requirement is tightened if the event is accepted by the single-electron trigger or the electron–muon trigger. Table 2 summarises the exact requirements used depending on the data-taking period.

Table 2: Transverse momentum thresholds applied to the selected electrons, muons and $\tau_{\text{had-vis}}$ depending on the trigger signature and the data-taking period. The p_{T} thresholds of the ATLAS lowest unprescaled triggers during the Run 2 data-taking are reported in Refs. [128–131]. The electron and muon trigger menu evolution throughout the Run 2 data-taking is discussed in Refs. [43, 44].

Trigger signature	Data-taking period	p_{T} threshold [GeV] used in event selection
Single electron	2015	$p_{\mathrm{T}}(e) > 25$
	2016–2018	$p_{\mathrm{T}}(e) > 27$
Single muon	2015	$p_{\mathrm{T}}(\mu) > 21$
	2016–2018	$p_{\mathrm{T}}(\mu) > 27.3$
One electron, one muon	2015–2018	$p_{\mathrm{T}}(e) > 18$, $p_{\mathrm{T}}(\mu) > 14.7$
Two $\tau_{\text{had-vis}}$	2015–2018	$p_{\mathrm{T}}(\text{leading } \tau_{\text{had-vis}}) > 40$ $p_{\mathrm{T}}(\text{sub-leading } \tau_{\text{had-vis}}) > 30$

Muons are reconstructed from signals in the MS matched with tracks inside the ID. They are required to satisfy the 'Loose' identification criteria [132], corresponding to an efficiency above 97% for all muon candidates considered in this analysis, and to have $p_{\mathrm{T}} > 10\,\text{GeV}$ and $|\eta| < 2.5$. In the $\tau_e\tau_\mu$ and $\tau_\mu\tau_{\text{had}}$ channels, the selected muon in the signal regions is further required to satisfy a 'Tight' isolation criterion [132] based on track information. This requirement has an efficiency increasing from 85% to 99% for muons with transverse momentum increasing from 10 GeV to 50 GeV and above. In the $\tau_\mu\tau_{\text{had}}$ channel, the requirement on the muon transverse momentum is further tightened to select events in which the single-muon trigger operates with very high efficiency. Similarly, in the $\tau_e\tau_\mu$ channel, the requirement is further tightened if the event is accepted by the single-muon trigger or the electron–muon trigger. Table 2 summarises the requirements used depending on the data-taking period.

Decays of τ_{had} are composed of a neutrino and a set of visible decay products, most frequently one or three charged pions and up to two neutral pions and denoted by $\tau_{\text{had-vis}}$. The reconstruction of the $\tau_{\text{had-vis}}$ is seeded by jets reconstructed using the anti-k_t algorithm [133], using calibrated topological clusters [134] as inputs, with a radius parameter of $R = 0.4$ [135]. The jets form $\tau_{\text{had-vis}}$ candidates and are additionally required to have $p_{\mathrm{T}} > 10\,\text{GeV}$ and $|\eta| < 2.5$. Reconstructed tracks are matched to $\tau_{\text{had-vis}}$ candidates. A multivariate discriminant is used to assess whether these tracks are likely to have been produced by the charged τ_{had} decay products, and is used to reject tracks originating from other interactions, nearby jets, photon conversions or misreconstructed tracks. The $\tau_{\text{had-vis}}$ objects are required to have one or three associated tracks selected by this discriminant. Their charge (q) is defined as the sum of the measured charges of these associated tracks and must have $|q| = 1$. The $\tau_{\text{had-vis}}$ objects must also satisfy the requirements $p_{\mathrm{T}} > 20\,\text{GeV}$ and $|\eta| < 2.47$, excluding the region $1.37 < |\eta| < 1.52$. These requirements have an efficiency of about 85% (70%) for the majority of hadronic τ decays with one (three) associated tracks measured in simulated $Z \to \tau\tau$ events. The $\tau_{\text{had-vis}}$ energy scale is determined by combining

information from the associated tracks, calorimeter clusters and reconstructed neutral pions [136] using a multivariate regression technique [135] trained in MC samples.

To separate the $\tau_{\text{had-vis}}$ candidates produced by hadronic τ decays from those due to jets initiated by quarks or gluons, a recurrent neural network (RNN) identification algorithm [137] is constructed employing information from reconstructed charged-particle tracks and calorimeter energy clusters associated with $\tau_{\text{had-vis}}$ candidates, as well as high-level discriminating variables. A separate boosted decision tree discriminant ('eBDT') is also constructed to reject backgrounds arising from electrons misidentified as $\tau_{\text{had-vis}}$ (mainly from $Z \to ee$ events in the $\tau_e\tau_{\text{had}}$ channel in this analysis). This discriminant is built using information from the calorimeter and the tracking detector, most notably transition radiation information from the TRT system and variables sensitive to the ratio of the energy deposited in the calorimeter and the visible momentum measured from the reconstructed tracks. In addition, a very loose requirement on the RNN score (corresponding to a percent level efficiency loss for signal $\tau_{\text{had-vis}}$) is applied, as well as a dedicated muon veto criterion, designed to reject muons misreconstructed as $\tau_{\text{had-vis}}$ (typically due to large calorimeter energy deposits).

In the $\tau_{\text{had}}\tau_{\text{had}}$ channel, the reconstructed $\tau_{\text{had-vis}}$ objects are required to match the two $\tau_{\text{had-vis}}$ candidates of the di-τ trigger, thus defining the two selected $\tau_{\text{had-vis}}$ of the event. In the $\tau_{\text{lep}}\tau_{\text{had}}$ channel, the $\tau_{\text{had-vis}}$ candidate with the highest transverse momentum is the only one kept, and other ones are considered as jets. This minimum requirement is much looser than the final RNN selection, and leads to a small loss of signal events where a quark- or gluon-initiated jet is taken as the $\tau_{\text{had-vis}}$ candidate, quantified to be at the level of 2.5% (4%) for the ggF (VBF) production process. However, this strategy simplifies the treatment of the background processes with jets misidentified as $\tau_{\text{had-vis}}$. The estimation of this background relies on a control region defined by inverting the final RNN selection. Picking a minimum requirement aimed at recovering the majority of this signal efficiency loss would sacrifice 30% to 40% of the statistical power in the control region, and would consequently degrade the estimate of this background (see Section 5.2).

The $\tau_{\text{had-vis}}$ objects are further required to fulfil the 'Medium' identification criteria in the signal regions of the $\tau_{\text{lep}}\tau_{\text{had}}$ and $\tau_{\text{had}}\tau_{\text{had}}$ channels, which corresponds to an efficiency of 75% (60%) for candidates with 1 (3) associated track(s). In the $\tau_e\tau_{\text{had}}$ channel, for events where the $\tau_{\text{had-vis}}$ object has only one associated charged track, the $\tau_{\text{had-vis}}$ object is required to pass the 'Medium' working point of the eBDT algorithm, which corresponds to an 85% efficiency for candidates which already satisfy the identification requirement. The transverse momentum requirement for the $\tau_{\text{had-vis}}$ objects in the $\tau_{\text{had}}\tau_{\text{had}}$ final state is tightened to select events recorded with the $\tau_{\text{had-vis}}$ trigger operating at its plateau efficiency, as shown in Table 2. In the $\tau_{\text{lep}}\tau_{\text{had}}$ final state, the $\tau_{\text{had-vis}}$ transverse momentum requirement is also tightened to $p_{\text{T}} > 30\,\text{GeV}$ to improve background rejection.

Jets are reconstructed using a particle-flow algorithm [138] from noise-suppressed positive-energy topological clusters in the calorimeter using the anti-k_t algorithm with a radius parameter $R = 0.4$. Cleaning criteria are used to identify jets arising from non-collision backgrounds or noise in the calorimeters [139], and events containing such jets are removed. A jet vertex tagger (JVT) [140] is used to remove jets with $p_{\text{T}} < 60\,\text{GeV}$ and $|\eta| < 2.5$ that are identified as not being associated with the primary vertex of the hard interaction. Similarly, pile-up jets in the forward region are suppressed with a 'forward JVT' [141] algorithm, exploiting jet shapes and topological jet correlations in pile-up interactions, which is applied to all jets with $p_{\text{T}} < 60\,\text{GeV}$ and $|\eta| > 2.5$. Only jets with $p_{\text{T}} > 20\,\text{GeV}$ are considered.

Jets with $p_{\text{T}} > 20\,\text{GeV}$ and $|\eta| < 2.5$ containing b-hadrons are identified using the DL1r b-tagging algorithm [142, 143]. In the $\tau_e\tau_\mu$ and $\tau_{\text{lep}}\tau_{\text{had}}$ channels, the fixed 85% efficiency working point is used, while the 70% efficiency working point is used in the $\tau_{\text{had}}\tau_{\text{had}}$ channel (the target efficiencies being measured

in simulated $t\bar{t}$ events). Since the algorithm is used to veto b-tagged jets, the 70% efficiency working point offers a looser veto criterion which improves the sensitivity in the $\tau_{\text{had}}\tau_{\text{had}}$ channel where the backgrounds from $t\bar{t}$ events are less significant. The rejection factors for b-tagged jets initiated by c-quarks and light partons are 9.4 (2.6) and 390 (29) respectively for the 70% (85%) efficiency working point.

The reconstructed objects used in this analysis are not built from disjoint sets of tracks or calorimetric clusters. It is therefore possible that two different objects share most of their constituents. An overlap removal procedure is applied to resolve this ambiguity. This procedure is summarised in Table 3. It uses a definition of angular distance, $\Delta R_y = \sqrt{(\Delta y)^2 + (\Delta\phi)^2}$, that is based on the rapidities y of the objects.

Table 3: Criteria applied to overlapping reconstructed objects. The criteria are listed in the order they are applied.

Object to remove	Object to keep	Criteria
electron	electron	If they share the same track, the electron with the highest transverse momentum is kept.
$\tau_{\text{had-vis}}$	electron	If $\Delta R_y < 0.2$, the electron is kept.
$\tau_{\text{had-vis}}$	muon	If $\Delta R_y < 0.2$, the muon is kept.
electron	muon	If they share a track, the electron is removed if the muon is associated with a signature in the muon spectrometer, otherwise the muon is removed.
jet	electron	Any jet within $\Delta R_y = 0.2$ of an electron is removed.
jet	muon	Any jet within $\Delta R_y = 0.2$ of a muon is removed if it has fewer than three associated tracks.
electron	jet	Any electron within $\Delta R_y = 0.4$ of a jet is removed.
muon	jet	Any muon within $\Delta R_y = 0.4$ of a jet is removed.
jet	$\tau_{\text{had-vis}}$	Any jet within $\Delta R_y = 0.2$ of a $\tau_{\text{had-vis}}$ is removed.

The missing transverse momentum vector, $\vec{E}_{\text{T}}^{\text{miss}}$, is reconstructed as the negative vector sum of the transverse momenta of leptons, $\tau_{\text{had-vis}}$ and jets, and a 'soft-term'. The soft-term is calculated as the vectorial sum of the p_{T} of tracks matched to the primary vertex but not associated with a reconstructed lepton, $\tau_{\text{had-vis}}$ or jet [144]. The magnitude of $\vec{E}_{\text{T}}^{\text{miss}}$ is referred to as the missing transverse momentum, $E_{\text{T}}^{\text{miss}}$.

4.2 Event selection

Events are selected if they contain a $H \to \tau\tau$ candidate in one of the final states under study ($\tau_e\tau_\mu$, $\tau_{\text{lep}}\tau_{\text{had}}$, $\tau_{\text{had}}\tau_{\text{had}}$).

The Higgs boson candidate is formed by the vector momentum sum of the visible τ-lepton decay products and $\vec{E}_{\text{T}}^{\text{miss}}$. Its invariant mass ($m_{\tau\tau}^{\text{MMC}}$) is calculated using an advanced likelihood-based technique, the Missing Mass Calculator (MMC) [145], which relies on information about the τ-lepton candidate momenta, the presence of additional jets, $\vec{E}_{\text{T}}^{\text{miss}}$ and the type of τ-lepton decay. The addition of information about the number of reconstructed charged and neutral pions [136] in hadronic decays of the τ-leptons in new parameterisations for the likelihood function derived using $Z \to \tau\tau$ MC events are improvements with

respect to Ref. [22] and lead to a 1% absolute improvement on the width of the reconstructed mass distribution.

For each channel a series of selection criteria are applied to enhance the sensitivity to the SM Higgs boson signal and ensure a robust estimate of the invariant mass of the reconstructed $\tau^+\tau^-$ system. These are summarised in Table 4.

In the $\tau_e\tau_\mu$ channel, events must have a single reconstructed electron and a single reconstructed muon satisfying the criteria discussed in Section 4.1. In order to reject events coming from W+jets, Z+jets and top processes,[8] the charges of the two reconstructed leptons must be of opposite sign, the invariant mass of the $e\mu$ system ($m_{e\mu}$) must be between 30 GeV and 100 GeV, and the collinear mass[9] ($m_{\tau\tau}^{\text{coll}}$) must be greater than $m_Z - 25$ GeV. This last criterion ensures the selected dataset does not include any event considered in the signal regions of the ATLAS measurements of the $H \to WW^*$ process discussed in Ref. [147]. To further reduce backgrounds from top processes, events with a b-tagged jet are rejected. In addition, angular requirements are placed on $\Delta R_{e\mu}$ and $|\Delta\eta_{e\mu}|$. Finally, a $p_{\text{T}} > 40$ GeV requirement is applied to the leading jet in the event to suppress backgrounds, as the signal final states considered include at least one high-p_{T} jet.

In the $\tau_{\text{lep}}\tau_{\text{had}}$ channel, events must have a single reconstructed light lepton and a single reconstructed $\tau_{\text{had-vis}}$ satisfying the criteria discussed in Section 4.1. In order to reject events coming from W+jets and top processes, the charges of the reconstructed light lepton and the reconstructed $\tau_{\text{had-vis}}$ must be of opposite sign. The transverse mass of the lepton+$\tau_{\text{had-vis}}$ system (m_{T}) is required to be smaller than 70 GeV in order to efficiently suppress W+jets processes. To further reduce backgrounds from top processes, an explicit requirement is imposed to reject events with a b-tagged jet. In addition, angular requirements are placed on $\Delta R_{\ell\tau_{\text{had-vis}}}$ and $|\Delta\eta_{\ell\tau_{\text{had-vis}}}|$. The requirement on the leading jet transverse momentum in the event is the same as for the $\tau_e\tau_\mu$ channel.

In the $\tau_{\text{had}}\tau_{\text{had}}$ channel, events must have exactly two reconstructed $\tau_{\text{had-vis}}$ objects satisfying the criteria discussed in Section 4.1. In order to maintain low thresholds for the p_{T} of the $\tau_{\text{had-vis}}$, additional criteria for the angular separation of the two $\tau_{\text{had-vis}}$ and the presence of an additional jet in the event were added to the lowest unprescaled di-τ trigger during the Run 2 data-taking. The additional criteria were imposed on the regions-of-interest (ROI) defining the $\tau_{\text{had-vis}}$ candidates at the L1 trigger. In order to ensure that the ROIs of the two reconstructed $\tau_{\text{had-vis}}$ do not have overlapping cores, the criterion $\Delta R_{\tau_{\text{had-vis}}\tau_{\text{had-vis}}} > 0.6$ is applied. The extra-jet trigger criterion mentioned above translates into a requirement on the presence of at least one jet with $|\eta| < 3.2$ and p_{T} greater than 70 GeV. Similarly to the $\tau_e\tau_\mu$ and $\tau_{\text{lep}}\tau_{\text{had}}$ channels, the charges of the two reconstructed $\tau_{\text{had-vis}}$ must be of opposite sign in order to reject events coming from W+jets and top processes. Events with b-tagged jets are rejected, except for the $\text{tt}(0\ell)H \to \tau_{\text{had}}\tau_{\text{had}}$ signal region (see next Section 4.3).

Finally, criteria concerning $E_{\text{T}}^{\text{miss}}$ and the fraction of the τ-lepton's momentum carried by its visible decay products, computed with the $\vec{E}_{\text{T}}^{\text{miss}}$ components decomposed into the collinear approximation (defined as x_1 and x_2 for leading and sub-leading reconstructed visible τ-lepton candidates respectively) are applied to improve the invariant mass estimation in the three channels.

[8] In the following, 'top processes' in the text ('Top' in tables and figures) collectively refer to single and pair production of top quarks.

[9] The di-τ mass reconstructed in the collinear approximation assumes that the neutrinos from the τ-lepton decays propagate in the same direction as the visible decay products and that the missing transverse momentum is caused solely by those neutrinos [146].

Table 4: Summary of the event selection for all sub-channels. The electron and muon p_{T} thresholds correspond to the 2016–2018 dataset. In the $\tau_e\tau_\mu$ channel, events recorded with the electron trigger must satisfy $p_{\mathrm{T}}(e) > 27\,\mathrm{GeV}$ and $p_{\mathrm{T}}(\mu) > 10\,\mathrm{GeV}$, events recorded with the muon trigger must satisfy $p_{\mathrm{T}}(e) > 15\,\mathrm{GeV}$ and $p_{\mathrm{T}}(\mu) > 27.3\,\mathrm{GeV}$, and events recorded with the electron–muon trigger must satisfy $p_{\mathrm{T}}(e) > 18\,\mathrm{GeV}$ and $p_{\mathrm{T}}(\mu) > 14.7\,\mathrm{GeV}$. Thresholds for the 2015 dataset are given in Table 2. The b-veto requirement in the $\tau_{\mathrm{had}}\tau_{\mathrm{had}}$ channel is not applied in the $\mathrm{tt}(0\ell)H \to \tau_{\mathrm{had}}\tau_{\mathrm{had}}$ category. The quantities x_1 and x_2 are the momentum fractions carried by the visible decay products of the two τ-leptons in the collinear approximation, as described in the text.

Criteria	$\tau_e\tau_\mu$	$\tau_{\mathrm{lep}}\tau_{\mathrm{had}}$		$\tau_{\mathrm{had}}\tau_{\mathrm{had}}$
		$\tau_e\tau_{\mathrm{had}}$	$\tau_\mu\tau_{\mathrm{had}}$	
$N(e)$	1	1	0	0
$N(\mu)$	1	0	1	0
$N(\tau_{\text{had-vis}})$	0	1	1	2
$N(b\text{-jets})$	0 (85% WP)	0 (85% WP)	0 (85% WP)	0 (70% WP) ($\geq$ 1 or 2 in ttH categories)
$p_{\mathrm{T}}(e)$ [GeV]	> 15 to 27	> 27		
$p_{\mathrm{T}}(\mu)$ [GeV]	> 10 to 27.3		> 27.3	
$p_{\mathrm{T}}(\tau_{\text{had-vis}})$ [GeV]		> 30		> 40, 30
Identification	e/μ: Medium	$e/\mu/\tau_{\text{had-vis}}$: Medium		$\tau_{\text{had-vis}}$: Medium
Isolation	e: Loose, μ: Tight	e: Loose	μ: Tight	
Charge		Opposite charge		
$E_{\mathrm{T}}^{\mathrm{miss}}$ [GeV]		> 20		
Kinematics	$m_{\tau\tau}^{\mathrm{coll}} > m_Z - 25\,\mathrm{GeV}$ $30\,\mathrm{GeV} < m_{e\mu} < 100\,\mathrm{GeV}$	$m_{\mathrm{T}} < 70\,\mathrm{GeV}$		
Leading jet	$p_{\mathrm{T}} > 40\,\mathrm{GeV}$			$p_{\mathrm{T}} > 70\,\mathrm{GeV}$, $\lvert\eta\rvert < 3.2$
Angular	$\Delta R_{e\mu} < 2.0$ $\lvert\Delta\eta_{e\mu}\rvert < 1.5$	$\Delta R_{\ell\tau_{\text{had-vis}}} < 2.5$ $\lvert\Delta\eta_{\ell\tau_{\text{had-vis}}}\rvert < 1.5$		$0.6 < \Delta R_{\tau_{\text{had-vis}}\tau_{\text{had-vis}}} < 2.5$ $\lvert\Delta\eta_{\tau_{\text{had-vis}}\tau_{\text{had-vis}}}\rvert < 1.5$
Coll. app. x_1/x_2	$0.1 < x_1 < 1.0$ $0.1 < x_2 < 1.0$	$0.1 < x_1 < 1.4$ $0.1 < x_2 < 1.2$		$0.1 < x_1 < 1.4$ $0.1 < x_2 < 1.4$

Assuming SM predictions, 2922 $H \to \tau\tau$ events (331, 1408, and 1183 events in the $\tau_e\tau_\mu$, $\tau_{\text{lep}}\tau_{\text{had}}$, and $\tau_{\text{had}}\tau_{\text{had}}$ channels respectively) are expected to be reconstructed and satisfy the event selection from the $\approx 440 \cdot 10^3$ $H \to \tau\tau$ events that were produced with $|y_H| < 2.5$ during the LHC Run 2. In data, 204 442 events are selected.

4.3 Event categorisation

The categorisation of selected events targets the four dominant Higgs boson production modes (see Section 1), uses their unique and characteristic signatures and is designed to closely match the production bins within the *stage 1.2* of the STXS framework. Bins of the full *stage 1.2* scheme are merged to match the available sensitivity of the selected $H \to \tau\tau$ events. Both the STXS bins and the event categories are illustrated in Figure 1.

Requirements on the reconstructed Higgs boson transverse momentum, $p_{\text{T}}(H)$, and on properties of additional jets are described in the following. Events in the VBF, V(had)H and tt(0ℓ)$H \to \tau_{\text{had}}\tau_{\text{had}}$ categories are further split with BDT taggers into two subcategories, the first (suffixed _1) with enhanced signal fractions and the second (suffixed _0) containing the remaining events. All taggers are designed inclusively for all di-τ decay modes and the variables are chosen to avoid any potential bias in the $m_{\tau\tau}^{\text{MMC}}$ distribution. For each tagger, this is verified by comparing templates of the $m_{\tau\tau}^{\text{MMC}}$ distribution for signal and background processes between the relevant subcategories. The taggers are described in the following and their input variables are listed in Table 5.

tt(0ℓ)$H \to \tau_{\text{had}}\tau_{\text{had}}$ categorisation

The final state targeted in the tt(0ℓ)$H \to \tau_{\text{had}}\tau_{\text{had}}$ category includes six jets and two of these jets are initiated by the hadronisation of a b-quark. However, to enhance the signal acceptance, the selection allows exactly one of these two numbers to be off by one unit. Therefore, the event selection in the tt(0ℓ)$H \to \tau_{\text{had}}\tau_{\text{had}}$ category requires the presence of either six jets with p_{T} greater than 20 GeV including at least one b-tagged jet or five jets including at least two b-tagged jets. The events satisfying these criteria are not considered by the analysis reported in Ref. [34].

The signal-enhancing separation in this category uses two BDTs: one BDT is optimised to enhance $t\bar{t}H$ signal events over $Z \to \tau\tau$ background events, while the second BDT is optimised to enhance $t\bar{t}H$ signal events over $t\bar{t}$ background events. A variety of two-dimensional combinations of requirements on the two BDT scores were studied, using the expected counting-experiment statistical significance,[10] including an estimate of the systematic uncertainties in the background normalisations, as an estimator for their performance; none was found to outperform a simple rectangular requirement in the plane formed by the two BDT scores, and this was the requirement ultimately selected. Of all Higgs boson events selected in the ttH_0 (ttH_1) categories 74% (92%) are due to the $t\bar{t}H$ process.

All other event categories in the $\tau_{\text{had}}\tau_{\text{had}}$ channel require that no b-tagged jets with $p_{\text{T}} > 20$ GeV and $|\eta| < 2.5$ are present.

[10] The 'Poisson-Binomial model' in Ref. [148].

Table 5: Variables used in the four multivariate taggers employed in the analysis. For each tagger, the presence or absence of a • indicates whether the variable is used or not. The symbol τ stands for any reconstructed τ-lepton candidate (electron, muon or $\tau_{\text{had-vis}}$) as appropriate in each channel. The symbols $\tau\tau$ and jj indicate the vectorial sums of the momenta of two visible τ-lepton candidates and of the two leading jets, respectively. The Higgs boson candidate H is formed by the vector sum of the two τ-lepton candidates' momenta and $\vec{E}_{\text{T}}^{\text{miss}}$. The W candidate is built as the pair of non-b-tagged jets in the event with invariant mass closest to m_W. The top-quark candidate is built as the system of the W candidate and a b-tagged jet in the event with invariant mass closest to m_{top}.

	Variable	VBF	V(had)H	ttH vs $t\bar{t}$	ttH vs $Z \to \tau\tau$
Jet properties	Invariant mass of the two leading jets	•	•		
	$p_{\text{T}}(jj)$	•	•		
	Product of η of the two leading jets	•			
	Sub-leading jet p_{T}	•			
	Leading jet η				•
	Sub-leading jet η				•
	Scalar sum of all jets p_{T}			•	•
	Scalar sum of all b-tagged jets p_{T}				•
	Best W-candidate dijet invariant mass			•	•
	Best t-quark-candidate three-jet invariant mass			•	•
Angular distances	$\Delta\phi$ between the two leading jets	•			
	$\Delta\eta$ between the two leading jets	•	•		
	ΔR between the two leading jets		•		
	$\Delta R(\tau\tau, jj)$		•		
	$\Delta R(\tau,\, \tau)$		•	•	
	Smallest ΔR (any two jets)			•	
	$\lvert\Delta\eta(\tau,\tau)\rvert$			•	•
τ prop.	$p_{\text{T}}(\tau\tau)$			•	
	Sub-leading τ p_{T}				•
	Sub-leading τ η				•
H cand.	$p_{\text{T}}(Hjj)$	•	•		
	$p_{\text{T}}(H)/p_{\text{T}}(jj)$		•		
$\vec{E}_{\text{T}}^{\text{miss}}$	Missing transverse momentum $E_{\text{T}}^{\text{miss}}$		•	•	•
	Smallest $\Delta\phi$ $(\tau, \vec{E}_{\text{T}}^{\text{miss}})$				•

VBF categorisation

The VBF categories are designed to select Higgs bosons produced from the fusion of two vector bosons emitted by two quarks of the colliding protons. The scattered quarks give rise to two high-p_{T} jets with a large rapidity gap and therefore large invariant mass m_{jj}. This signature allows VBF events to be experimentally distinguished from the other Higgs production modes and $Z \to \tau\tau$ events.

To match the STXS $qq \to H$ particle-level $p_{\mathrm{T}}^{\mathrm{jet}}$ requirement and m_{jj} binning, events selected in the VBF categories must have $m_{jj} > 350\,\mathrm{GeV}$ and p_{T} of the sub-leading jet greater than 30 GeV. Additional selection criteria are applied to enhance the VBF Higgs production mode relative to the $Z \to \tau\tau$ background. The product of the pseudorapidities of the two leading jets ($\eta(j_0) \times \eta(j_1)$) is required to be negative (i.e. jets must be in opposite hemispheres of the detector). The absolute difference in pseudorapidity ($|\Delta\eta_{jj}|$) is required to be greater than 3. Finally, the visible decay products of the τ-leptons are required to be reconstructed in the rapidity gap between the VBF jets.

The VBF tagger is optimised by treating both the ggF $H \to \tau\tau$ and $Z \to \tau\tau$ events as backgrounds and relies solely on observables based on the kinematics of the two leading jets (see Table 5). While the expected contribution from ggF $H \to \tau\tau$ events is small, the considerably larger theoretical uncertainty associated with its cross-section prediction in this kinematic phase space can significantly enlarge the systematic uncertainty of the VBF production cross-section measurement.

The BDT score requirement used to define the categories was optimised to give the smallest uncertainty in the VBF cross-section, and provides a selection where the fraction of VBF events among all Higgs boson events is about 94% (63%) in the VBF_1 (VBF_0) region.

V(had)H categorisation

To match the STXS $qq \to V(\to qq)H$ particle-level $p_{\mathrm{T}}^{\mathrm{jet}}$ requirement and m_{jj} binning, events selected in the V(had) categories must satisfy $60\,\mathrm{GeV} < m_{jj} < 120\,\mathrm{GeV}$ and p_{T} of the sub-leading jet greater than 30 GeV.

The V(had)H tagger was trained by treating all Higgs events produced by processes other than VH as background. The BDT score requirement used to define the two categories was optimised to give the smallest uncertainty for the V(had)H cross-section, and provides a selection where the expected fraction of V(had)H among all Higgs boson events is 66% (24%) in the VH_1 (VH_0) category.

Boost categorisation

Events failing to meet the criteria of the VBF, V(had)H and ttH categories but having high-p_{T} Higgs candidates are considered for the 'boost' categories targeting ggF events with large Higgs boson transverse momentum. The reconstructed Higgs boson transverse momentum, $p_{\mathrm{T}}(H)$, is determined from the Higgs boson candidate defined by the vectorial sum of the momenta of the visible decay products of the τ-leptons and $\vec{E}_{\mathrm{T}}^{\mathrm{miss}}$. Events in the boost category must satisfy $p_{\mathrm{T}}(H) > 100\,\mathrm{GeV}$. To match the STXS $gg \to H$ particle-level requirements, events are further categorised by $p_{\mathrm{T}}(H)$ value and by the total number of jets with p_{T} greater than 30 GeV ($N_{\mathrm{jets}}(p_{\mathrm{T}} > 30\,\mathrm{GeV})$). Events with $p_{\mathrm{T}}(H) < 200\,\mathrm{GeV}$ are separated into 1-jet and ≥2-jet categories, while for $p_{\mathrm{T}}(H) > 200\,\mathrm{GeV}$ events with at least one jet are considered without further jet-multiplicity separation of the events. Table 6 describes the boost phase-space categorisation.

Table 6: Definition of the six categories in the boosted phase space.

$N_{\text{jets}}(p_{\text{T}} > 30\,\text{GeV})$	$p_{\text{T}}(H)$ bins in GeV			
	[100, 120]	[120, 200]	[200, 300]	[300, ∞[
Exactly 1	boost_0_1J	boost_1_1J	boost_2	boost_3
At least 2	boost_0_ge2J	boost_1_ge2J		

The three analysis channels are therefore split into six kinematic categories in the boost phase space for a total of eighteen categories in the fit performed for the cross-section measurement.

Summary

Nine bins of the STXS framework are targeted in the measurement presented in this paper and are illustrated in Figure 1. The expected signal yields for each of these bins is presented in Figure 2(a), while Figure 2(b) illustrates the relative population of these nine bins in each reconstruction category described in this section. Events selected in each reconstruction category are used to build templates of the $m_{\tau\tau}^{\text{MMC}}$ variable for each of the nine bins. As illustrated in Figure 2, ggF events produced with $p_{\text{T}}(H) < 200\,\text{GeV}$ and two additional jets forming a system with $m_{jj} > 350\,\text{GeV}$ are mainly reconstructed in the VBF_0 category (61%) and the boost_1_ge2J category (36%). It is difficult to select these events in only a single category but through the simultaneous usage of all the categories, their production rate can be measured. In contrast, the reconstructed ggF event candidates satisfying $60\,\text{GeV} < p_{\text{T}}(H) < 120\,\text{GeV}$ are further separated into those produced with a single jet (boost_0_1J) and those produced with two jets forming a system with $m_{jj} < 350\,\text{GeV}$ (boost_0_ge2J). However, the categorisation does not provide enough sensitivity to measure these two contributions individually and they are therefore combined.

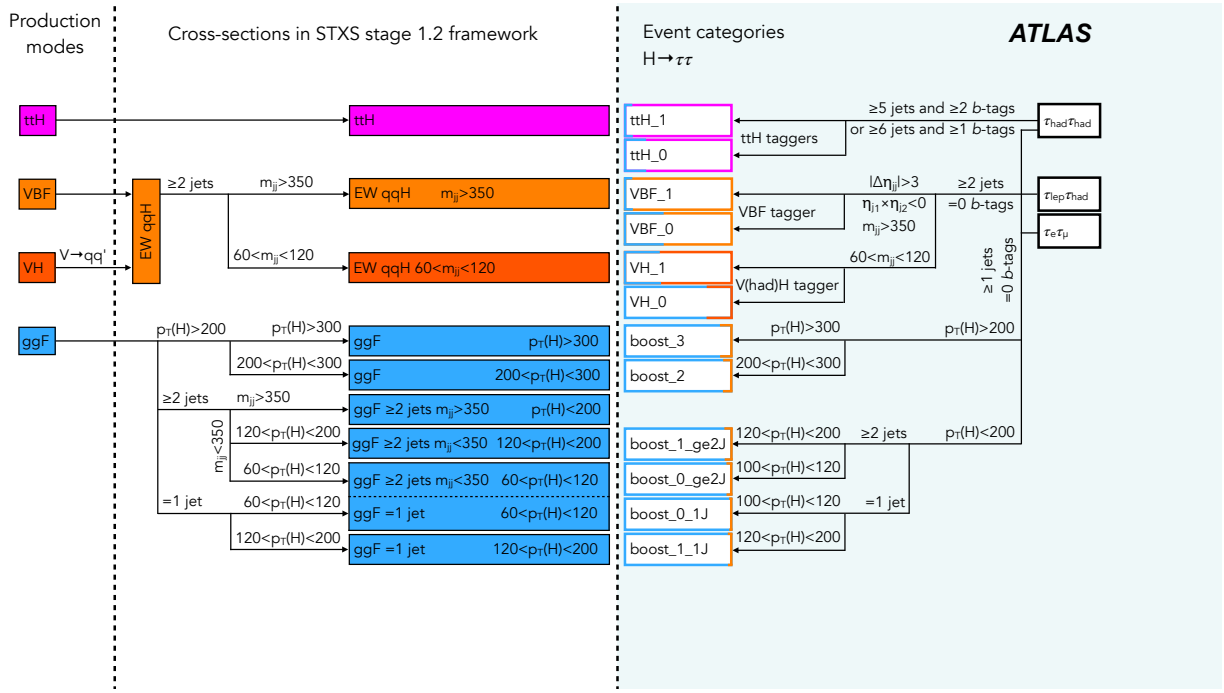

Figure 1: Sketch of the event categorisation and the targeted cross-sections in the STXS *stage 1.2* framework (bins). The relative contributions to each event category from the two most dominant STXS bins are indicated by the two colours used along the width of the category box. The requirements on $p_{\mathrm{T}}(H)$ and m_{jj} are given in units of GeV.

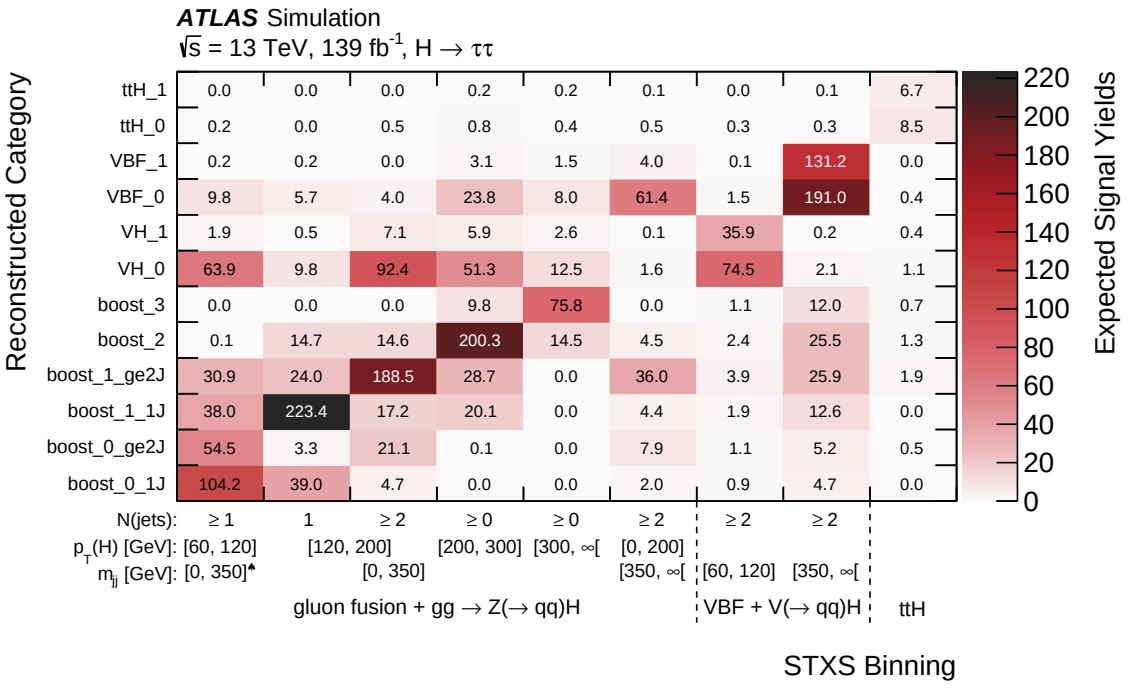

(a)

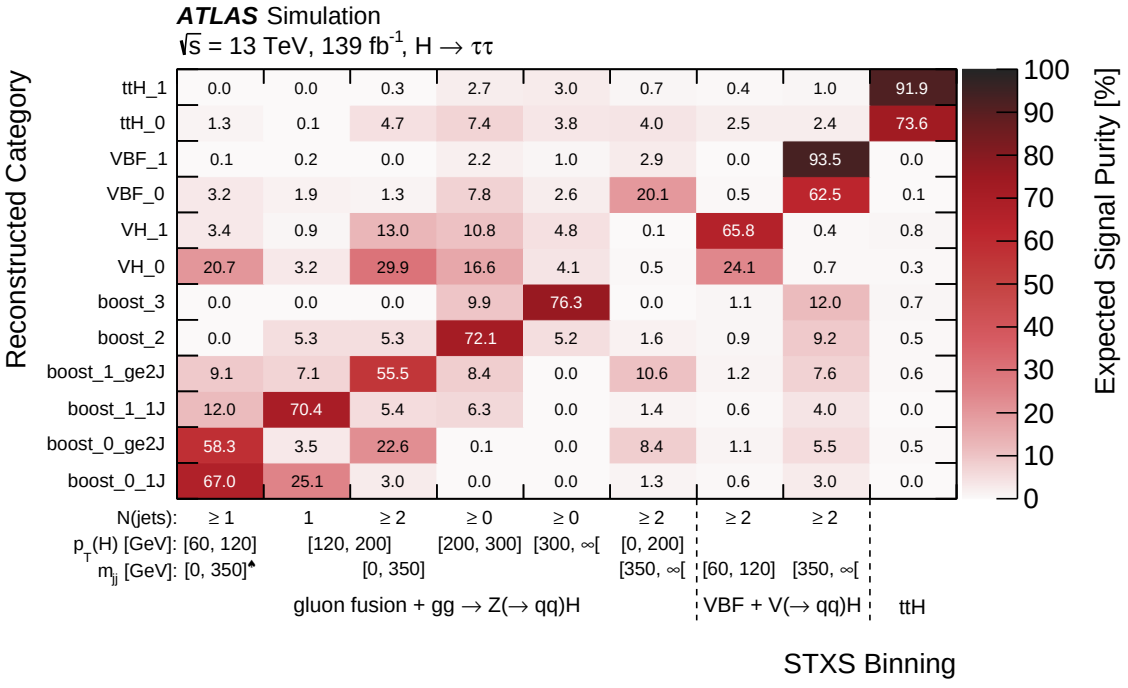

(b)

Figure 2: (a) Expected $H \to \tau\tau$ signal yield in each of the reconstructed-event categories of the analysis (y-axis) for each of the nine measured STXS bins (x-axis). (b) Relative contribution of each of the nine measured STXS bins to the total $H \to \tau\tau$ signal expectation in each reconstructed-event category. The spades symbol (♠) indicates that the criteria for m_{jj} only apply to events with at least two reconstructed jets. Yields are summed over the three di-τ decay channels ($\tau_e\tau_\mu$, $\tau_{\text{lep}}\tau_{\text{had}}$, $\tau_{\text{had}}\tau_{\text{had}}$).

5 Background modelling

The expectations from SM processes other than the $H \to \tau\tau$ signal in the phase space of the analysis are evaluated using a mixture of simulations and data-driven techniques. Processes with $\tau_{\text{had-vis}}$, prompt light leptons or light leptons from τ-lepton decays are estimated through simulations. Among these, $Z(\to \tau\tau)$ + jets and top processes are dominant, and dedicated control regions are employed to validate the simulations of both processes and to constrain their normalisation in the signal regions. For the $Z(\to \tau\tau)$ + jets background, a control region enriched in $Z(\to \ell\ell)$ + jets events is defined as described in Section 5.1. In the $\tau_e\tau_\mu$ and $\tau_{\text{lep}}\tau_{\text{had}}$ channels, control regions enriched in top-induced processes are defined by replacing the b-jet veto from the event selection (see Table 4) with a requirement of at least one b-tagged jet.

Using these control regions, the templates of the $m_{\tau\tau}^{\text{MMC}}$ observable from the simulations are checked in each event category (see Section 4.3). Very good agreement with the data is observed.

Smaller background contributions are due to diboson, $Z(\to \ell\ell)$ + jets and $H \to WW^*$ processes. They are normalised to their theoretical expectations. Contributions from light- and heavy-flavour jets misidentified as electrons, muons or $\tau_{\text{had-vis}}$, as well as non-prompt electrons or muons, collectively referred to as misidentified τ background, are estimated using data-driven techniques. Their estimation is detailed in Section 5.2.

Figure 3 illustrates the measured composition of the selected events in each category of the analysis.

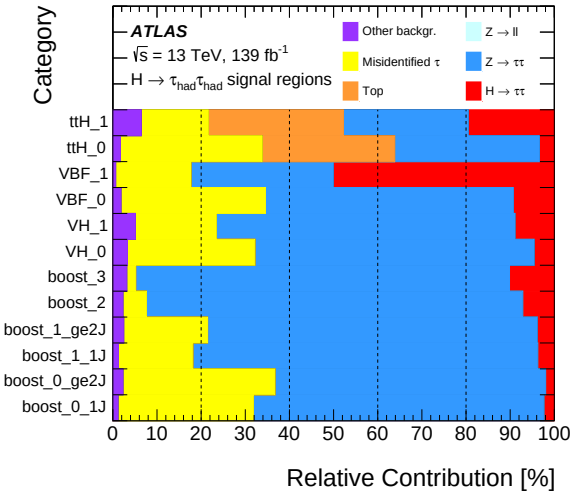

(a) $\tau_{\text{had}}\tau_{\text{had}}$

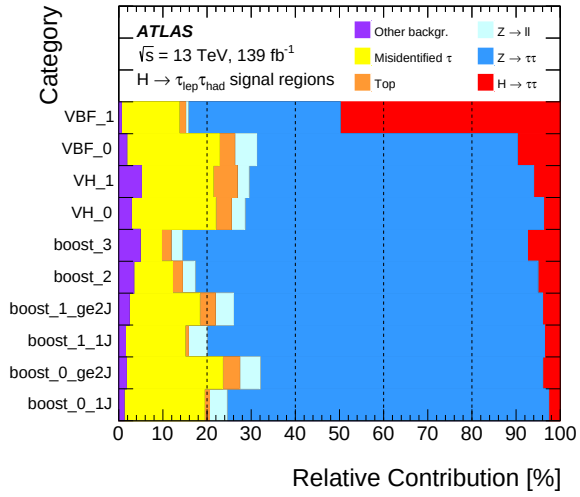

(b) $\tau_{\text{lep}}\tau_{\text{had}}$

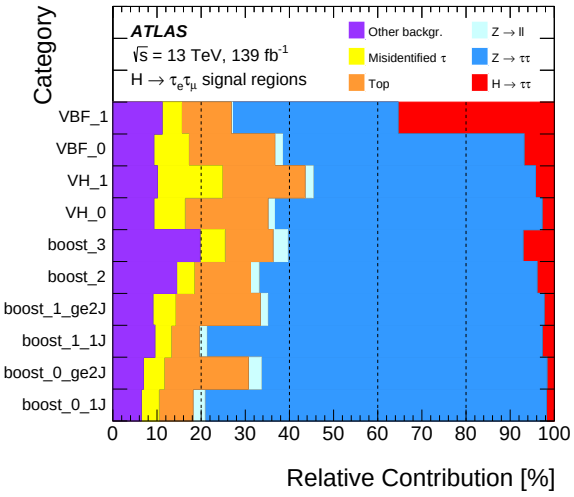

(c) $\tau_e\tau_\mu$

Figure 3: Relative contribution of each process to the total measured yields in each category of the analysis for the (a) $\tau_{\text{had}}\tau_{\text{had}}$, (b) $\tau_{\text{lep}}\tau_{\text{had}}$ and (c) $\tau_e\tau_\mu$ channels, within 100 GeV< $m_{\tau\tau}^{\text{MMC}}$ < 150 GeV. 'Other backgr.' includes diboson and $H \to WW^*$ processes.

5.1 $Z \to \tau\tau$ background modelling using $Z \to \ell\ell$ events

Events from the $Z(\to \tau\tau)$ + jets process form the dominant source of background in this measurement. They account for 79% of the background across all signal regions, and up to 90% of the background in the most boosted regime investigated in the analysis. They are estimated using MC simulations validated with data. The predictions from these MC simulations are corrected using dedicated control regions based on the $Z(\to \ell\ell)$ + jets process with kinematic properties of the events similar to those of the corresponding signal regions as explained in the following.

In order to mimic as well as possible the Z boson kinematics and the associated production of jets in $Z(\to \tau\tau)$ + jets events selected in the signal regions, the selected $Z(\to \ell\ell)$ + jets events are modified through a simplified implementation of the embedding procedure. The kinematic properties of the Z boson are reconstructed with a much better resolution in the $Z \to \ell\ell$ decay channel than in the $Z \to \tau\tau$ one due to the absence of neutrinos and the excellent momentum resolution of the ATLAS detector for electrons and muons. While the original method presented in Refs. [36, 37] relied on substituting the detector signatures of the objects before re-reconstructing the event, the simplified embedding consists of a rescaling of the transverse momentum of each reconstructed lepton through parameterisations, followed by a recomputation of all the relevant kinematic quantities in the analysis. The method used entails a significant reduction of complexity.

Embedding techniques are of particular interest in this analysis, where no statistically significant study of the $Z(\to \tau\tau)$ + jets background can be performed in data without looking at the signal regions. In this context, the simplified embedding can be applied to data events passing the $Z(\to \ell\ell)$ + jets selection, thus obtaining a $Z \to \tau\tau$ control region that is orthogonal to the signal region. This control region can also be used to measure the $Z \to \tau\tau$ normalisation in a phase space relevant to this measurement.

The $Z(\to \ell\ell)$ + jets events are selected using the single-lepton triggers and are required to have exactly two electrons or two muons with opposite charge. The selected electrons and muons must satisfy the identification and isolation criteria defined in Table 4. Additionally, the invariant mass of the dilepton system must be above 80 GeV. The selected sample contains about $9.3 \cdot 10^6$ data events and 99% of them are expected to come from $Z(\to \ell\ell)$ + jets processes. A small contribution from diboson and top processes with two electrons or two muons in the final state is also expected and the embedding procedure is also applied to them. Contributions from processes with jets misidentified as leptons were found to be negligible. Selected events in data and simulation are then randomly separated into three subsets to provide a statistically independent control region for each of the $\tau_e\tau_\mu$, $\tau_{\text{lep}}\tau_{\text{had}}$ and $\tau_{\text{had}}\tau_{\text{had}}$ signal regions.

Weights derived in simulations are applied to each event to remove the kinematic biases and normalisation effects introduced by the electron and muon trigger, reconstruction, identification, and isolation algorithms. The four-vectors of the reconstructed electrons and muons are used to pair each lepton in the $Z(\to \ell\ell)$ + jets event with a scaling term, which parameterises the effects of τ-lepton decay kinematics and of the energy calibration algorithms for τ-leptons with similar four-vectors. The scaling term is derived as a function of the transverse momentum and the pseudorapidity of the τ-lepton before it decays. The original four-vectors of the electrons and muons are scaled using this term so that they match those of the visible reconstructed decay products of either leptonically or hadronically decaying τ-leptons. The $Z(\to \ell\ell)$ + jets event yields are then reweighted to account for the expected efficiencies of the reconstruction, identification and calibration steps for the visible τ decay products.

The per-lepton weights assume collinearity of the τ-lepton and its visible decay products and cannot take into account any correlation between the Z boson decay products. All event variables used in the signal

region definitions are recalculated using the kinematics of the new final-state physics objects, and a weight is applied to each event to account for the expected trigger efficiency associated with these objects. The implementation of the new embedding procedure is validated by comparing $Z \to \ell\ell$ simulated events, after applying this procedure, with $Z \to \tau\tau$ simulations, where both the kinematic and spin-correlation effects are modelled correctly. Figure 4 shows good agreement between the distributions of the two samples for two illustrative cases and indicates that the assumptions made in calculating the weights have negligible impact on the relevant observables.

All uncertainties affecting the reconstructed physics objects used in embedding are propagated through the full procedure, including those associated with the parameterisations. Dedicated uncertainties affecting each control region are assigned to account for the differences in modelling observed between the $Z \to \tau\tau$ and embedded $Z \to \ell\ell$ MC predictions, which are expected to come from approximations associated with the simplified embedding procedure. These uncertainties are derived by studying the change in the data-to-simulation normalisation factors as events are moved between different control regions to cover the observed acceptance mismodeling. They are found to be at the 1% level and cover for the residual non-closure observed in Fig. 4.

Distributions for this control region, and a comparison with the embedding of all the simulated background processes, are shown in Figure 5. The observed discrepancies are consistent with the results reported in dedicated measurements of the Z+jets processes [149, 150]. The impact of this mismodelling on the analysis is alleviated by the use of control regions mimicking the event selection criteria after the embedding procedure is applied to data and simulated events.

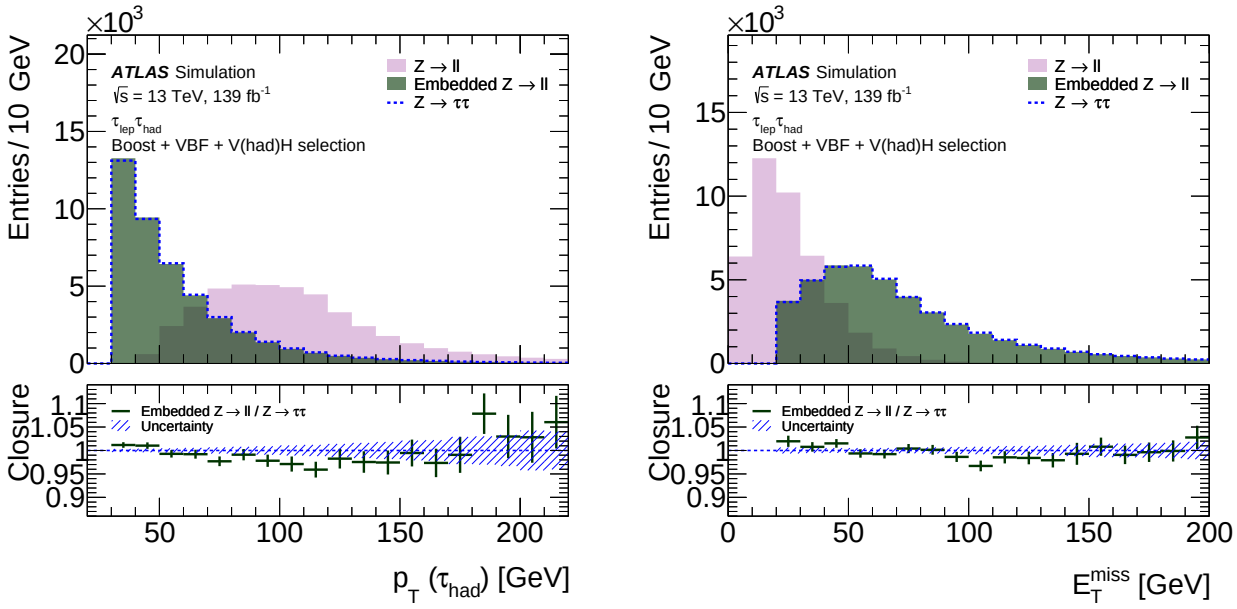

(a) p_{T} (τ_{had})

(b) $E_{\mathrm{T}}^{\mathrm{miss}}$

Figure 4: Comparison of kinematic quantities for $Z \to \ell\ell$ simulated events in the $\tau_{\mathrm{lep}}\tau_{\mathrm{had}}$ channel before (light purple histogram) and after (dark green histogram) the embedding procedure, in the boost, VBF and V(had)H phase spaces combined. The distribution for $Z \to \tau\tau$ simulated events (dashed blue line) is also shown. (a) p_{T} distribution of the simulated τ_{had} in the event. For the $Z \to \ell\ell$ events, the reconstructed lepton with the highest p_{T} in the event is shown. For the $Z \to \ell\ell$ events after the embedding procedure, a scaling term is applied to the p_{T} of the lepton chosen to mimic the τ_{had} as described in the text. (b) $E_{\mathrm{T}}^{\mathrm{miss}}$ distribution. The bottom panels display the ratio of embedded $Z \to \ell\ell$ events to $Z \to \tau\tau$ events. The error bars display the statistical uncertainties in the ratio and the dashed blue band illustrates the statistical uncertainty in the $Z \to \tau\tau$ simulation.

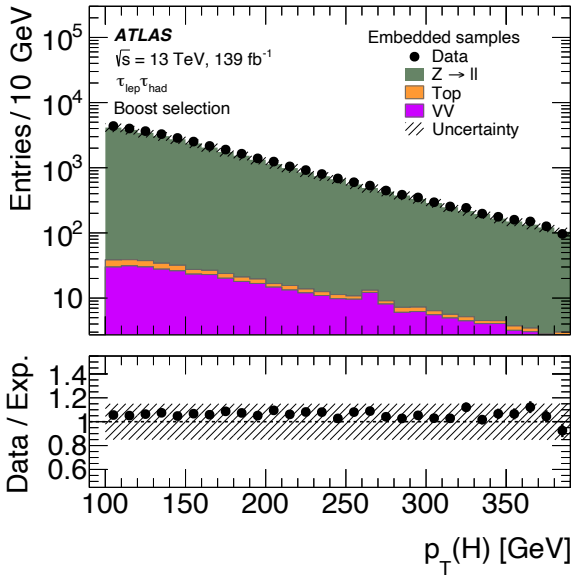

(a) $p_{\mathrm{T}}(H)$ in boost categories

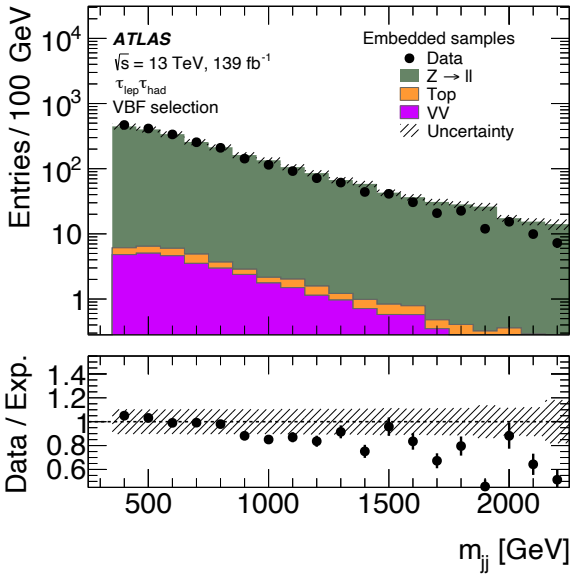

(b) m_{jj} in VBF categories

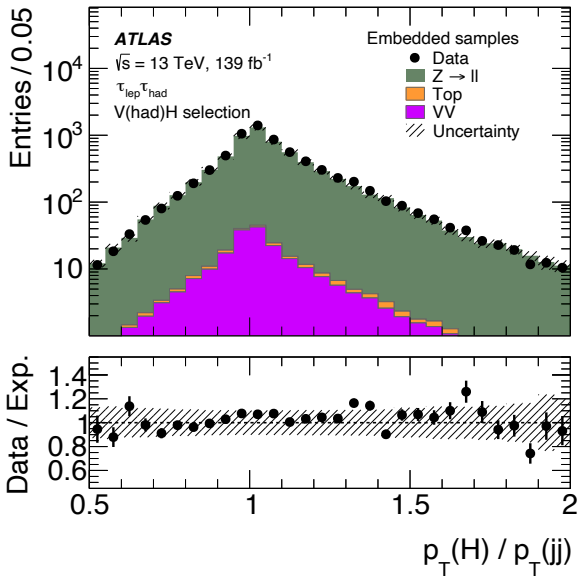

(c) $p_{\mathrm{T}}(H)/p_{\mathrm{T}}(jj)$ in V(had)H categories

Figure 5: Comparison between MC simulation prediction and data in the $Z(\rightarrow \ell\ell)$ + jets-enriched control regions. The embedding procedure is applied to the data and simulation samples to mimic the $\tau_{\mathrm{lep}}\tau_{\mathrm{had}}$ event selection: (a) $p_{\mathrm{T}}(H)$ in the boost categories, (b) m_{jj} in the VBF categories and (c) $p_{\mathrm{T}}(H)/p_{\mathrm{T}}(jj)$ in the V(had)H categories. The bottom panels show the level of agreement between the embedded data and the embedded simulation samples. The uncertainty is the sum in quadrature of the statistical uncertainty of the simulated events and the systematic uncertainties of the simulation. Only the acceptance uncertainties in each category are considered. The shape variations, translating to potential bin-by-bin changes, were estimated to be minor and are not displayed.

5.2 Data-driven estimate of misidentified τ processes

Processes with at least one jet misidentified as an electron, muon or τ_{had} are collectively referred to as misidentified τ background. They account for a fraction of the total background ranging from 5% to 25%, with less importance in the more boosted categories. They are evaluated in a similar fashion in the three channels of the analysis. First, data events are selected using the same criteria as for the SRs with the exception of the criteria for electron or muon identification and isolation and the criteria for $\tau_{\text{had-vis}}$ identification. These criteria are loosened or inverted depending on the specific methodology used in each channel. Then, transfer factors are computed in dedicated control regions. These factors are used to correct for the kinematic and normalisation differences between the events with altered isolation or identification criteria and the SRs.

In the $\tau_e\tau_\mu$ channel, the misidentified τ background is estimated using the matrix-method technique [151]. Data events are selected by removing the lepton isolation criteria from the nominal selection, and loosening the identification criteria for electrons. The expected number of fake leptons in the SR is computed from a system of equations relating the efficiencies for real (ϵ_{R}) and fake leptons (ϵ_{F}) to the observed event yields. The efficiencies are estimated separately for electrons and muons and are parameterised as a function of the p_{T} and η of the leptons. The real-lepton efficiencies ϵ_{R} are estimated using simulations, while the fake-lepton efficiencies ϵ_{F} are measured using data events selected to have two leptons of the same charge. For the latter, the contribution from events with real leptons is subtracted using MC simulations; they account for approximately 35% of the 1333 selected events.

Dedicated uncertainties estimated for these predictions account for: statistical uncertainties in the derived efficiencies (∼10%), dependencies of ϵ_{F} on the numbers of jets and b-tagged jets in the final state (∼35%), the dependency of ϵ_{R} on whether they are measured in $t\bar{t}$, $Z(\rightarrow \ell\ell)$ + jets or $Z(\rightarrow \tau\tau)$ + jets events (∼15%), and the uncertainty associated with the normalisation of the contribution from real leptons during the measurement of ϵ_{F} (∼15%).

In the $\tau_{\text{lep}}\tau_{\text{had}}$ channel, the misidentified τ background refers to events with a jet misidentified as a $\tau_{\text{had-vis}}$. Contributions with a real τ_{had} and a jet misidentified as an electron or a muon are estimated from simulations to be negligible. The misidentified τ background is evaluated using the fake-factor technique [152]. Data events are selected if they satisfy a very loose requirement on the $\tau_{\text{had-vis}}$ identification score but do not satisfy the 'Medium' working point criteria (such events are 'reverse-identified'). All other criteria of the nominal selection of the $\tau_{\text{lep}}\tau_{\text{had}}$ channel are applied. Residual contributions from processes with real $\tau_{\text{had-vis}}$ satisfying this requirement are evaluated using simulations and subtracted accordingly. They account for approximately 18% of the 136 500 selected events.

The distribution of the misidentified τ background component in the SR is obtained by multiplying the contribution of the data events selected by the reverse-identified criterion with a fake factor defined as the ratio of misidentified $\tau_{\text{had-vis}}$ that respectively pass or fail the 'Medium' working point of the $\tau_{\text{had-vis}}$ identification algorithm. These fake factors are parameterised as a function of the p_{T} and track multiplicity of the $\tau_{\text{had-vis}}$. Two sets of fake factors are derived in separate regions and then combined for the final estimate. The first set is derived in a region enriched in W+jets processes obtained by inverting the SR criterion for m_{T} (see Table 4). The second set is derived in a control region enriched in QCD multijet processes obtained by inverting the isolation criteria for the selected electron or muon. An estimate of the fraction of events expected to originate from QCD multijets is used to determine the relative weighting of both sets of fake factors; it is parameterised as a function of the p_{T} and η of the $\tau_{\text{had-vis}}$ candidate. This estimate is obtained by scaling the number of events in the second control region by the ratio of

events where the light lepton respectively fails or passes the isolation requirements, measured in another QCD-multijet-enriched region where the τ_{lep} and τ_{had} have the same charge.

Uncertainties in the fake factors are estimated, and account for statistical uncertainties in the fake factors and their relative weighting (∼15%), for uncertainties associated with the subtraction of the residual contributions from processes with real τ_{had} (∼10%), and for uncertainties in the flavour composition (∼10%), taken from comparisons between the predicted and observed backgrounds in a dedicated validation region.

In the $\tau_{\text{had}}\tau_{\text{had}}$ channel, the misidentified τ background is also determined using a fake-factor approach. The method differs slightly from the one used in the $\tau_{\text{lep}}\tau_{\text{had}}$ channel: the fake factors are parameterised to simultaneously account for processes with one or two jets misidentified as $\tau_{\text{had-vis}}$. Additionally, the reconstructed $\tau_{\text{had-vis}}$ candidates are matched to their high-level-trigger counterparts. The fake factors are estimated in the W+jets-enriched region defined for the $\tau_{\text{lep}}\tau_{\text{had}}$ channel, but with the addition of the trigger-matching requirement in the $\tau_{\text{had-vis}}$ definition.

Two alternative sets of fake factors are computed in control regions defined with two $\tau_{\text{had-vis}}$. The first alternative set is derived by inverting the requirement on the $\Delta\eta(\tau_{\text{had-vis}}, \tau_{\text{had-vis}})$ variable with respect to the signal region. The second is derived by requiring the charges of the two $\tau_{\text{had-vis}}$ to have the same sign. The difference between these two alternative sets and the nominal fake factors derived in the W+jets-enriched control region is used to estimate the uncertainty in the composition of the misidentified τ background (∼15%). Two additional uncertainties in the misidentified τ background estimate in the $\tau_{\text{had}}\tau_{\text{had}}$ channel are considered: the statistical uncertainty of the fake-factor calculation (∼15%), and uncertainties related to the parameterisation choice for the fake factors (∼5%).

In the $\tau_e\tau_\mu$ and $\tau_{\text{lep}}\tau_{\text{had}}$ channels, the analysis employs control regions enriched in top processes. In these control regions, heavy-flavour jets misidentified as electrons or muons represent 70% to 80% of the expected contributions for the $\tau_e\tau_\mu$ channel, while for the $\tau_{\text{lep}}\tau_{\text{had}}$ channel about 25% of misidentified $\tau_{\text{had-vis}}$ originate from heavy-flavour jets. To estimate these contributions, the data-driven estimate described above is repeated with the b-jet veto replaced by a b-tagged jet requirement to mimic the control region selection.

The modelling of the misidentified τ background was validated in dedicated regions for each channel. In the $\tau_{\text{had}}\tau_{\text{had}}$ channel, the validation region selects events with $\Delta\eta(\tau_{\text{had-vis}}, \tau_{\text{had-vis}}) > 2.0$. In the $\tau_{\text{lep}}\tau_{\text{had}}$ channel, the validation region contains events with a light lepton and $\tau_{\text{had-vis}}$ of the same charge. Finally, events with same-charge leptons are used as the validation region for the $\tau_e\tau_\mu$ channel. Figure 6 illustrates the modelling of the misidentified τ background in the validation region for each channel. Good agreement between the observed data and the prediction is seen in all cases.

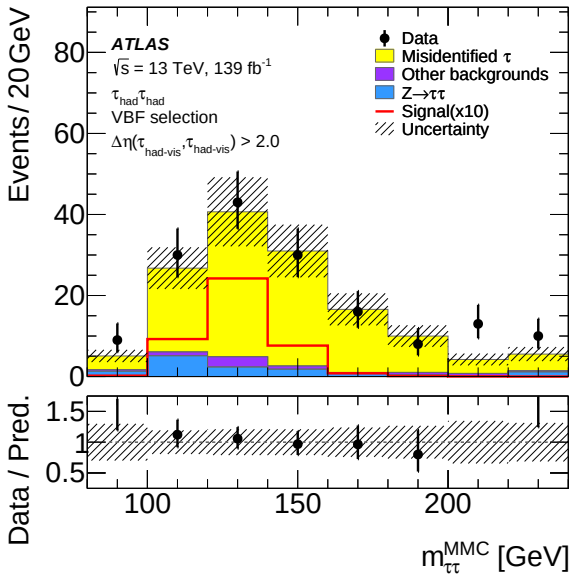

(a) $\tau_{\text{had}}\tau_{\text{had}}$

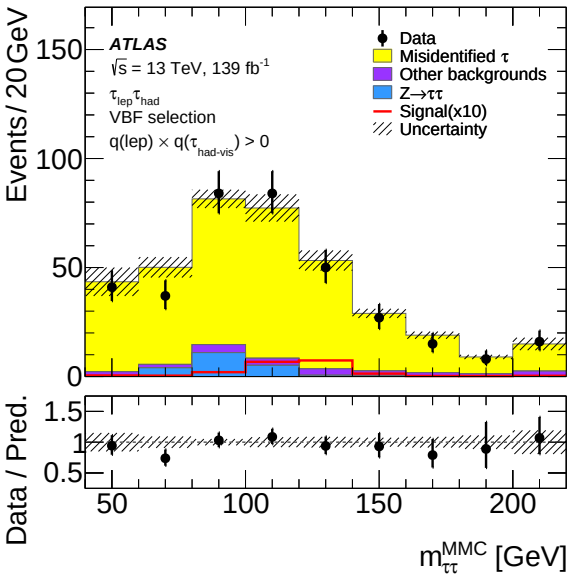

(b) $\tau_{\text{lep}}\tau_{\text{had}}$

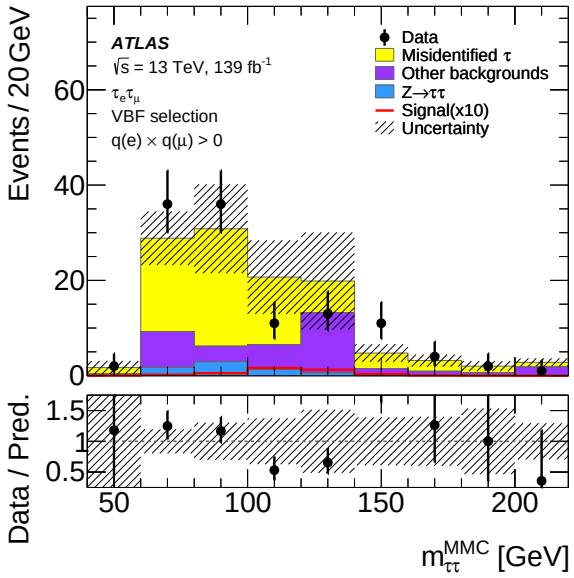

(c) $\tau_e\tau_\mu$

Figure 6: Validation of the data-driven estimate of the processes with jets misidentified as $\tau_{\text{had-vis}}$ in the VBF categories: (a) events with $\Delta\eta(\tau_{\text{had-vis}}, \tau_{\text{had-vis}}) > 2.0$ in the $\tau_{\text{had}}\tau_{\text{had}}$ final state, (b) events with a light lepton and $\tau_{\text{had-vis}}$ of the same charge in the $\tau_{\text{lep}}\tau_{\text{had}}$ channel, and (c) events with same-charge leptons in the $\tau_e\tau_\mu$ final state. The hashed band represents the statistical uncertainty due to the limited size of the simulated samples and the systematic uncertainty of the data-driven estimate.

6 Systematic uncertainties

Systematic uncertainties affect the yields in the various signal and control regions as well as the distribution shape of the main fit observable ($m_{\tau\tau}^{\text{MMC}}$). They can be assigned to three main groups: the experimental uncertainties, the theoretical uncertainties for the backgrounds and the theoretical uncertainties for the signal. They are detailed in the following sections. Their impact on the measured $pp \to H \to \tau\tau$ cross-section is summarised in Table 7. Systematic uncertainty sources are parameterised in the statistical analysis using nuisance parameters with Gaussian priors (see Section 7).

Table 7: Summary of the different sources of uncertainty in decreasing order of their impact on $\sigma(pp \to H \to \tau\tau)$. Their observed and expected fractional impacts, both computed by the fit, are given, relative to the $\sigma(pp \to H \to \tau\tau)$ value. Experimental uncertainties for reconstructed objects combine efficiency and energy/momentum scale and resolution uncertainties. Background sample size includes the bin-by-bin statistical uncertainties in the simulated backgrounds as well as statistical uncertainties in misidentified τ backgrounds, which are estimated using data.

Source of uncertainty	Impact on $\Delta\sigma / \sigma(pp \to H \to \tau\tau)$ [%]	
	Observed	Expected
Theoretical uncertainty in signal	8.7	8.5
Jet and $\vec{E}_{\text{T}}^{\text{miss}}$	4.5	4.2
Background sample size	4.0	3.7
Hadronic τ decays	2.1	2.1
Misidentified τ	2.0	2.0
Luminosity	1.8	1.8
Theoretical uncertainty in Z + jets processes	1.7	1.2
Theoretical uncertainty in top processes	1.1	1.1
Flavour tagging	0.4	0.5
Electrons and muons	0.4	0.4
Total systematic uncertainty	12.0	11.4
Data sample size	7.2	6.7
Total	13.9	13.2

6.1 Experimental uncertainties

In addition to the object misidentification rate already discussed in Section 5.2, experimental systematic uncertainties include those on the trigger, reconstruction, identification and isolation efficiencies for the final-state particle candidates, and their energy scale and resolution. These uncertainties affect the shape of the $m_{\tau\tau}^{\text{MMC}}$ distribution, the background yields and the signal cross-section through their effects on the acceptance and the migration between different event categories.

The dominant experimental uncertainties in the measurement of the $pp \to H \to \tau\tau$ cross-section are related to the jet energy scale and resolution, to the $\tau_{\text{had-vis}}$ candidate identification and energy scale, and to the object misidentification rates, as shown in Table 7. The uncertainties related to the reconstruction and identification of electrons and muons and the jet b-tagging efficiency have only a minor impact on the measurement.

The jet energy scale uncertainty consists of components related to the in situ calibration of jets as well as pile-up, the extrapolation to higher transverse momentum, and uncertainties related to the different responses to quark- and gluon-initiated jets. The latter is of particular importance and covers both the uncertainties in the response of the detector to particular jet flavours and the uncertainty in the response due to the unknown fractions of quark- and gluon-initiated jets within the sample. The jet energy scale uncertainty for central jets ($|\eta| < 1.2$) varies from 1% for a wide range of jet p_{T} (250 GeV $< p_{\mathrm{T}} <$ 2000 GeV), to 5% for very low p_{T} jets (20 GeV) and 3.5% for very high p_{T} jets ($>$ 2.5 TeV). The relative jet energy resolution is measured in a dedicated analysis [153] and ranges from (24 ± 5)% at 20 GeV to (6 ± 0.5)% at 300 GeV.

The uncertainties in the $\tau_{\text{had-vis}}$ identification efficiency are in the range of 2% to 6%, while the trigger efficiency and the eBDT efficiency uncertainties are of the order of 1% to 1.5% and 1% to 2%, respectively. All these uncertainties are parameterised as a function of the $\tau_{\text{had-vis}}$ p_{T} and number of associated tracks (identification and trigger efficiency) or τ decay mode (eBDT efficiency). As this analysis is highly sensitive to the $\tau_{\text{had-vis}}$ reconstruction efficiency uncertainty due to the introduction of the $Z \to \ell\ell$ control regions, this efficiency is left as a free parameter in the fit and measured in situ; the associated uncertainty is found to be at the 2% level. For the $\tau_{\text{had-vis}}$ energy scale, the total uncertainty is in the range of 1% to 4%, arising from a combination of measurements: a direct measurement with $Z \to \tau\tau \to \mu\tau_{\text{had-vis}} + 3\,\nu$ events, measurements of the calorimeter response to single particles, and comparisons between simulations using different detector geometries or GEANT4 physics lists. This uncertainty is also parameterised as a function of the $\tau_{\text{had-vis}}$ p_{T} and number of associated tracks [135].

All of the above uncertainties affecting the different hard objects are propagated through the $\vec{E}_{\mathrm{T}}^{\mathrm{miss}}$ calculation. Additional uncertainties associated with the scale and resolution of the soft-term of the $\vec{E}_{\mathrm{T}}^{\mathrm{miss}}$ [144] are also considered.

The luminosity uncertainty is considered only for the background samples whose normalisations are not determined in data (diboson, $Z \to \ell\ell$, non-($H \to \tau\tau$) Higgs) and to derive the signal cross-sections from the measured yields. The uncertainty in the combined 2015–2018 integrated luminosity is 1.7% [154], obtained using the LUCID-2 detector [155] for the primary luminosity measurements.

6.2 Background theoretical uncertainties

Theoretical uncertainties are considered for the two main background contributions in this analysis: Z + jets and $t\bar{t}$. The normalisation of these backgrounds is determined in the fit to the data in the signal and control regions (see Section 7). The theoretical uncertainties of Z + jets and $t\bar{t}$ are therefore parameterised to account for the migration across the analysis regions and to account for their impact on the $m_{\tau\tau}^{\mathrm{MMC}}$ templates in each region.

For Z + jets, uncertainties were considered for renormalisation (μ_{r}), factorisation (μ_{f}) and resummation scale (μ_{q}) variations, for the jet-to-parton matching scheme (CKKW), for variations in the choice of α_{s} value, and for the choice of PDFs. Uncertainties from missing higher orders were evaluated [156] using six variations of the QCD μ_{r} and μ_{f} scales in the matrix elements by factors of 0.5 and 2, avoiding the extreme variations in opposite directions. Uncertainties in the nominal PDF set were evaluated using 100 replica variations; an uncertainty is derived in each bin of the $m_{\tau\tau}^{\mathrm{MMC}}$ templates by evaluating the $\pm 1\sigma$ spread of the 100 replica variations. The effect of the uncertainty in the strong coupling constant α_{s} was assessed by variations of ±0.001. The resummation scale uncertainties were estimated using generator-level parameterisations derived from samples with μ_{q} varied by factors of 2 and 0.5 from its nominal value. Similarly, the jet-to-parton matching uncertainties were estimated using generator-level

parameterisations derived from samples with the CKKW parameter set to 15 GeV and 30 GeV, compared to the nominal value of 20 GeV.

For $t\bar{t}$, uncertainties were considered for the choice of matrix element and parton shower generators, the choice of model for initial- and final-state radiation (ISR and FSR respectively), and the choice of PDFs. The uncertainty due to ISR was estimated by simultaneously varying the h_{damp} parameter and the μ_{r} and μ_{f} scales, and propagating the α_{s} uncertainties through the Var3c parameter of the A14 tune as described in Ref. [157]. The impact of FSR was evaluated by varying the μ_{r} scale for emissions from the parton shower by factors of 2 and 0.5. The impact of using a different matrix element was evaluated by comparing the nominal $t\bar{t}$ sample with an event sample produced using MadGraph5_aMC@NLO 2.6.0 instead of Powheg Box v2 but keeping the same parton shower model. The impact of using a different parton shower and hadronisation model was evaluated by comparing the nominal $t\bar{t}$ sample with an event sample which was interfaced with Herwig 7.04 [158, 159] instead of Pythia 8 and used the H7UE set of tuned parameters [159] and the MMHT2014lo PDF set [160].

The NNPDF3.0lo replicas were used to evaluate the PDF uncertainties for the nominal PDF. For both Z + jets and $t\bar{t}$, the central value of the PDF was additionally compared with the central values of the CT14nnlo [161] and MMHT2014nnlo [160] PDF sets.

Theory uncertainties in Z + jets and $t\bar{t}$ predictions represent a sub-leading contribution, compared to signal theoretical uncertainties and experimental uncertainties (see Table 7).

For renormalisation and factorisation scale variations and PDF uncertainties, their impact on the extrapolation factor between each SR and its corresponding $Z \to \ell\ell$ control region, and on the shape of the $m_{\tau\tau}^{\text{MMC}}$ distribution, is treated as uncorrelated across the different categories. This choice is driven by the structure of the statistical analysis, which employs a dedicated control region to constrain the Z + jets prediction in each signal region.

6.3 Signal theoretical uncertainties

Signal theoretical uncertainties are the dominant source of uncertainty for this analysis. For each signal process, several sources of uncertainty are considered, including the uncertainty in the total inclusive cross-section (evaluated only for the $pp \to H \to \tau\tau$ cross-section measurement), the parton-shower and hadronisation model effect and the migration uncertainties among the STXS bins. The migration uncertainties stem from the determination of the kinematic quantities used in the STXS framework as well the expected relative contribution of each process in the signal regions. These uncertainties can affect signal acceptance in the various SRs as well as the $m_{\tau\tau}^{\text{MMC}}$ shape. For all production modes, uncertainties are estimated for the PDF and α_{s}, the parton shower and hadronisation model, and missing higher orders in the matrix element calculation. PDF and α_{s} uncertainties were estimated using the PDF4LHC15nlo set of eigenvectors. The impact of using a different parton shower and hadronisation model is evaluated by comparing the nominal sample with an event sample which was interfaced with Herwig 7 instead of Pythia 8. The effects on the signal expectations are treated as uncorrelated between the production modes, and the comparison leads to the largest uncertainty in the $pp \to H \to \tau\tau$ cross-section measurement. Uncertainties from missing higher orders are calculated following the methodology outlined in Refs. [27, 162] and are determined as follows.

For the ggF process, 15 main sources of uncertainty were considered. Four of these are jet-multiplicity-related uncertainties due to missing high-order corrections, and are estimated using the approach described

in Refs. [27, 163]. Three uncertainties parameterise the uncertainties in modelling the Higgs boson p_{T} and the 0-jet bin, one of which encapsulates the treatment of the top-quark mass in the loop corrections. Three uncertainties take into account dijet mass migrations across the STXS bin boundaries. Finally, three uncertainties are considered for the modelling of the ggF process in the VBF phase space. Two of them are derived using the method described in Ref. [164], from the study of the selection of exactly two or at least three jets. The third one is derived from the comparison of the Powheg prediction with MadGraph5_aMC@NLO samples using the FxFx prescriptions [165] to merge the jet multiplicities and it also applies to the VH phase space. As the ggF process in the VBF phase space is difficult to model, the impact of increasing its contribution in the VBF_1 category was estimated. Doubling its contribution induced a 7% shift in the apparent VBF production cross-section.

For the VBF and VH processes, ten uncertainties related to the STXS categorisation were considered: one related to the inclusive cross-section of the process, one related to the two-jet requirement, one related to the Higgs boson p_{T} selection at 200 GeV, one related to the p_{T} balance between the Higgs boson and the dijet system in events with two or three jets, and six uncertainties taking into account dijet mass migrations across the STXS bin boundaries.

For the $t\bar{t}H$ process, six other uncertainties are included: one related to the inclusive cross-section of the process, and five migration uncertainties related to Higgs boson p_{T} boundaries in the STXS scheme.

7 Statistical analysis

A statistical analysis of the collected data is performed to measure the $pp \to H \to \tau\tau$ cross-sections. The procedure relies on a likelihood function constructed as the product of Poisson probability terms over the bins of the input distributions, with parameters of interest (POIs) estimated by maximising the likelihood. The likelihood function comprises 32 signal regions and 36 control regions. In each signal region, Poisson terms describe the expected event counts in each bin of the $m_{\tau\tau}^{\mathrm{MMC}}$ distribution, while in each control region a single Poisson term describes the total expected event yield in that region. Figure 7 illustrates the usage of the signal and control regions in the construction of the likelihood function. The test statistic is constructed from the profile likelihood ratio and the confidence intervals on the the parameters of interest are derived unsing the asymptotic approximation [166].

The normalisation of the $Z \to \tau\tau$ background is left as a freely floating parameter in the fit in several regions. Each signal region in the boost, VBF and V(had)H categories is paired with an associated embedded $Z \to \ell\ell$ control region and both share a common $Z \to \tau\tau$ normalisation factor. Additionally, a common $Z \to \tau\tau$ normalisation factor is shared between the ttH_0 and ttH_1 signal regions. In total, 31 floating normalisation factors are defined in order to constrain the yields of the $Z \to \tau\tau$ background in the signal regions. The normalisation of the top processes is also allowed to float freely with six normalisation factors defined for boost, VBF, and V(had)H signal regions in the $\tau_e\tau_\mu$ and $\tau_{\mathrm{lep}}\tau_{\mathrm{had}}$ channels separately and one for the ttH categories in the $\tau_{\mathrm{had}}\tau_{\mathrm{had}}$ channel. The other backgrounds are normalised to their expected cross-section and the integrated luminosity of the recorded data.

In the signal regions, a smoothing procedure is applied to remove potentially large local fluctuations in the $m_{\tau\tau}^{\mathrm{MMC}}$ templates caused by the limited size of the MC samples used to build the templates.

The uncertainties affecting the model (see Section 6) are constrained by Gaussian probability terms and are treated as nuisance parameters. The $m_{\tau\tau}^{\mathrm{MMC}}$ template of uncertainties that are subject to large statistical

fluctuations is smoothed, and uncertainties that have a negligible impact on the final results are pruned away sample-by-sample and region-by-region.

The $m_{\tau\tau}^{\text{MMC}}$ discriminant distributions in each SR are binned in a way that maximises the significance of each targeted signal production mode, taking into account the full uncertainties. Effectively, this leads to a fine binning near the resonant $Z \to \tau\tau$ peak with coarser binning further away from it.

Three different measurements are performed. They include the branching ratio of $H \to \tau\tau$ and are performed with true Higgs boson rapidity $|y_H| < 2.5$. They differ in the definition of the POIs (see also Figure 1):

1. $pp \to H \to \tau\tau$ *cross-section*: a single POI, corresponding to the $pp \to H \to \tau\tau$ cross-section, is estimated by the fit. In the likelihood function, the signal yields in each category are parameterised as the product of the $pp \to H \to \tau\tau$ cross-section, the integrated luminosity and the efficiency (including the acceptance of the ATLAS detector) of the selection for a SM Higgs boson with a mass of 125.09 GeV. In this measurement, the relative contributions to the $pp \to H \to \tau\tau$ cross-section from the various production modes are fixed to the SM predictions.

2. *Cross-sections per production mode*: four POIs, corresponding to the cross-sections of the four dominant production modes (ggF, VBF, VH, $t\bar{t}H$) of the Higgs boson, are estimated by the fit. In this configuration, the event yields in the likelihood function are the sum of those from each individual production mode, parameterised as a function of the POI similarly to the way for the first measurement.

3. *Reduced Simplified Template Cross-Sections*: nine POIs, corresponding to the cross-sections of merged bins of the STXS *stage 1.2* framework shown in Figure 2, to which this analysis is sensitive, are determined by the fit. The cross-sections for $t\bar{t}H$ production and for VBF + $qq \to V(\to qq)H$ production are measured. The latter is measured for events with particle-level dijet mass between 60 GeV and 120 GeV or above 350 GeV. In addition, the cross-section of ggF production is measured in six bins of the phase space. One of them is a combination of two bins in the *stage 1.2* prescription: events with one jet and intermediate $p_{\text{T}}(H)$ (60 to 120 GeV) are measured together with events with two or more jets, low m_{jj} (< 350 GeV) and the same intermediate $p_{\text{T}}(H)$.

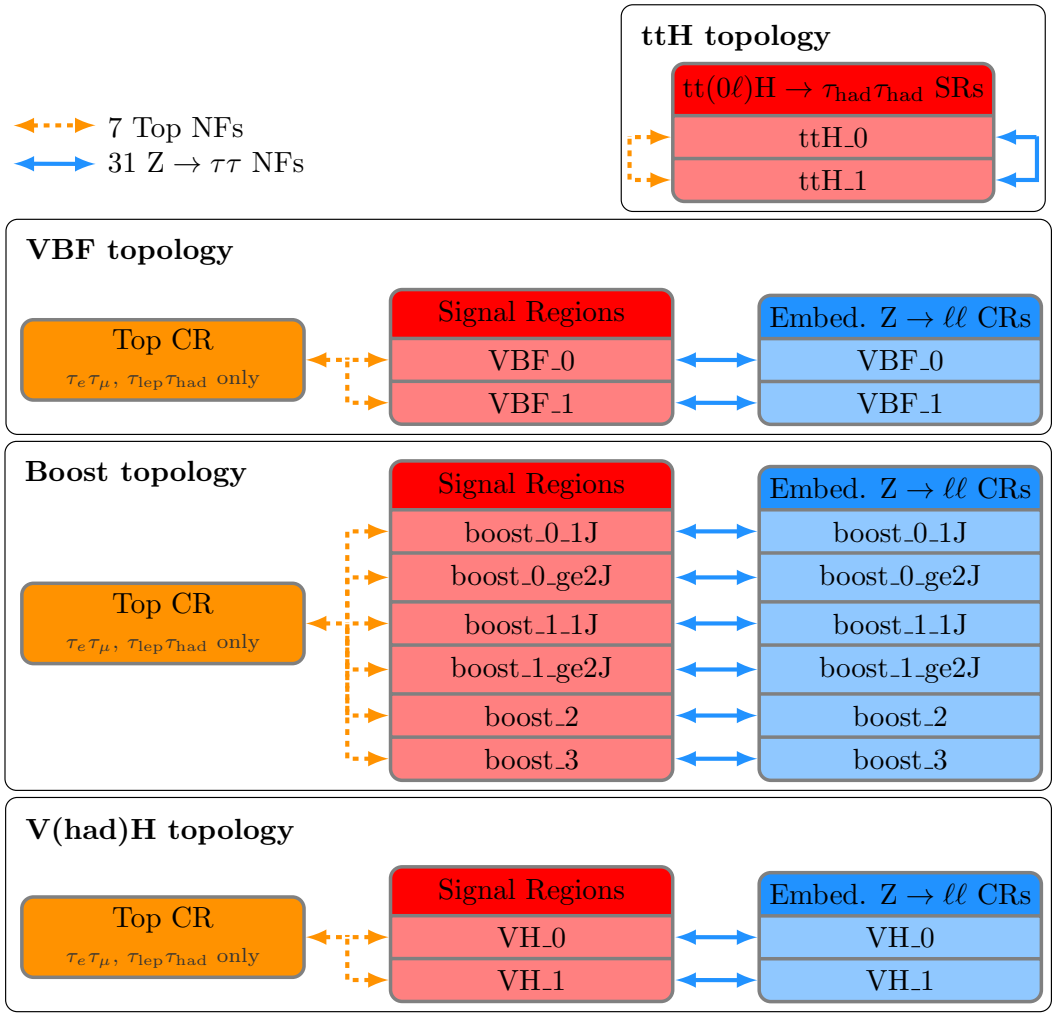

Figure 7: Graphical representation of the regions considered in the likelihood function and the normalisation factors (NFs) defined in the analysis. The four unfilled black boxes represent the four main topologies targeted in this measurement. Within each unfilled black box, the dark filled coloured boxes represent from left to right, the Top control regions, the signal regions and the $Z \to \ell\ell$ control regions. When applicable the subcategories are represented by a light filled colour. Each blue solid arrowed-line represents a normalisation factor that applies to the $Z(\to \tau\tau)$ + jets process in the signal regions and to the $Z(\to \ell\ell)$ + jets process in the $Z \to \ell\ell$ control regions. Each orange dashed arrowed-line represents a normalisation factor that applies to the top processes in the signal regions and to the top processes in the Top control regions. The arrow ends of each line indicate which regions are connected by each normalisation factor. In the likelihood function, there are signal regions and $Z \to \ell\ell$ control region for each final state in the VBF, boost and V(had)H topologies. Therefore, the ten signal regions and $Z \to \ell\ell$ control regions are repeated three times. The Top control regions are only used in the $\tau_e\tau_\mu$ and $\tau_{\text{lep}}\tau_{\text{had}}$ final states. Additionally, only one Top control region is considered by each topology.

8 Results

The results of the statistical analysis (see Section 7) performed for the $pp \to H \to \tau\tau$ cross-section measurement are presented in Figures 8 to 11. Additional figures displaying the results of the total cross-section measurement with the binning used in the statistical analysis are available in the appendix. The observed event yields and predictions as computed by the fit in the signal regions of the analysis are reported in Tables 8 to 13. Excellent agreement is observed between the data and the expectations. All measurements include the branching ratio of $H \to \tau\tau$ and are performed with true Higgs boson rapidity $|y_H| < 2.5$.

The $pp \to H \to \tau\tau$ cross-section is measured to be $2.94 \pm 0.21(\text{stat})^{+0.37}_{-0.32}(\text{syst})$ pb, in agreement with the SM predictions (3.17 ± 0.09 pb) with a p-value of 0.58.

The measurement is also performed in the $\tau_{\text{had}}\tau_{\text{had}}$, $\tau_{\text{lep}}\tau_{\text{had}}$ and $\tau_e\tau_\mu$ final states separately and in the boost, VBF, V(had)H and tt(0ℓ)$H \to \tau_{\text{had}}\tau_{\text{had}}$ categories. The results are illustrated in Figure 12. The p-values for the compatibility of the measurements are 0.30 across τ-lepton decay modes and 0.72 across kinematic categories.

The same dataset is subsequently used to measure the production cross-section for the Higgs boson in the four dominant production mechanisms. The results are illustrated in Figure 13(a) and reported in Table 14 with a breakdown of the uncertainties. They are all consistent with the SM predictions, with a p-value of 0.98. The measurement establishes the observation of the VBF production of the Higgs boson in the di-τ decay channel with an observed (expected) significance of 5.3σ (6.2σ).

The VBF production cross-section measurement is the most precise of the four dominant production mechanisms. The theoretical uncertainties in VBF production are smaller than in the other channels, and the VBF_1 categories represent the best combination of high signal yields and purity in this measurement. The measured VBF cross-section is $0.197 \pm 0.028(\text{stat})^{+0.032}_{-0.026}(\text{syst})$ pb. The second most precisely measured cross-section is that of ggF, $2.7 \pm 0.4(\text{stat})^{+0.9}_{-0.6}(\text{syst})$ pb, corresponding to an observed (expected) significance of 3.9σ (4.6σ). The VH and $t\bar{t}H$ production modes are determined with lower precision. The measured VH cross-section is $0.12 \pm 0.06(\text{stat}) \pm 0.04(\text{syst})$ pb, while the $t\bar{t}H$ cross-section is $0.033^{+0.033}_{-0.029}(\text{stat})^{+0.022}_{-0.017}(\text{syst})$ pb. Figure 13(b) illustrates the observed correlation between the measured cross-section parameters in the fit. The ggF cross-section exhibits an anti-correlation of 24% and 29% with the VBF and VH cross-sections respectively. This is caused by a significant contribution of ggF events to the VBF_0, VH_0 and VH_1 categories as illustrated by Figure 2. The simultaneous measurement of the cross-sections of the four dominant production modes is compatible with the SM expectations, with a p-value of 0.88.

Finally, the $pp \to H \to \tau\tau$ cross-sections are measured as a function of $p_{\text{T}}(H)$, $N_{\text{jets}}(p_{\text{T}} > 30\,\text{GeV})$ and m_{jj} in a reduced set of the bins of the *stage 1.2* of the STXS framework. The results, illustrated in Figure 14(a), are reported in Table 15. They are in very good agreement with the SM expectations. The gluon–gluon fusion + $gg \to Z(\to qq)H$ production mode is measured in four $p_{\text{T}}(H)$ intervals starting at 60 GeV. For $p_{\text{T}}(H)$ values between 120 GeV and 200 GeV, the measurements are further separated depending on the number of jets in the event. The best precision is obtained in the $p_{\text{T}}(H)$ interval between 200 GeV and 300 GeV and in the $p_{\text{T}}(H)$ regime above 300 GeV. The cross-sections are determined with an uncertainty of 37% and 42% respectively.

The EW production mode includes the VBF and $qq \to V(\to qq)H$ processes and is measured in m_{jj} intervals. In the interval with m_{jj} between 60 GeV and 120 GeV, the measurement has an uncertainty of

63%. The EW production mode for events with m_{jj} greater than 120 GeV is measured with an uncertainty of 26% and is the most precise cross-section determined within the simplified template cross-section framework in this paper. It exhibits an anti-correlation of approximately 40% with the cross-section for gluon–gluon fusion events produced in the same interval ($m_{jj} > 350$ GeV) as illustrated on Figure 14(b).

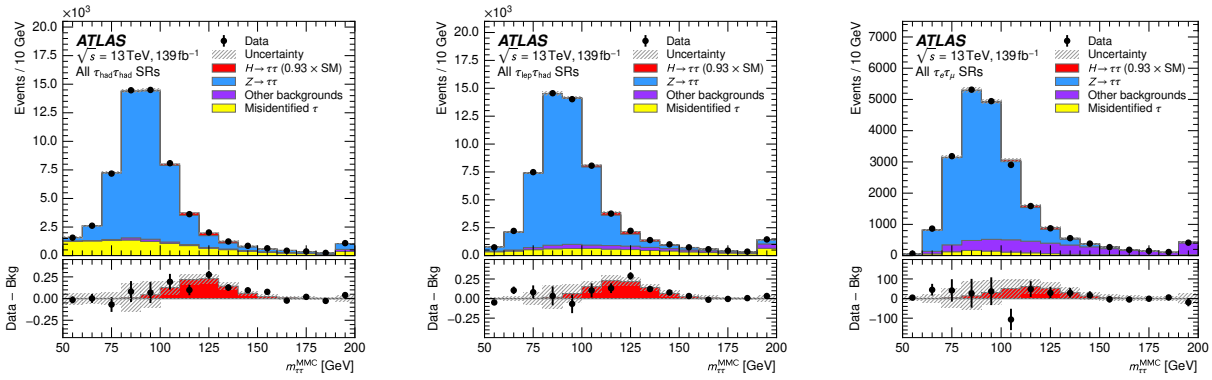

(a) $\tau_{\text{had}}\tau_{\text{had}}$ (b) $\tau_{\text{lep}}\tau_{\text{had}}$ (c) $\tau_e\tau_\mu$

Figure 8: Distribution of the reconstructed di-τ invariant mass ($m_{\tau\tau}^{\text{MMC}}$) for all events in the (a) $\tau_{\text{had}}\tau_{\text{had}}$, (b) $\tau_{\text{lep}}\tau_{\text{had}}$ and (c) $\tau_e\tau_\mu$ signal regions. The bottom panel shows the differences between the numbers of observed data events and expected background events (black points). The observed Higgs boson signal, corresponding to $(\sigma \times B)/(\sigma \times B)_{\text{SM}} = 0.93$, is shown with a filled red histogram. Entries with values above the x-axis range are shown in the last bin of each distributions. The dashed band indicates the total uncertainty on the total predicted yields. The prediction for each sample is determined from the likelihood fit performed to measure the $pp \to H \to \tau\tau$ cross-section.

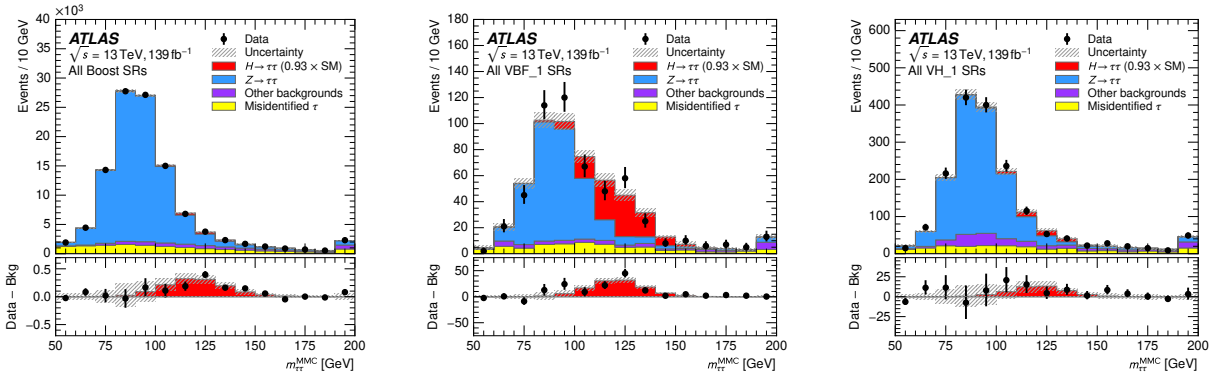

(a) boost (b) VBF_1 (c) VH_1

Figure 9: Distribution of the reconstructed di-τ invariant mass ($m_{\tau\tau}^{\text{MMC}}$) for all events in the (a) boost, (b) VBF_1 and (c) VH_1 signal regions. The bottom panel shows the differences between the numbers of observed data events and expected background events (black points). The observed Higgs boson signal, corresponding to $(\sigma \times B)/(\sigma \times B)_{\text{SM}} = 0.93$, is shown with a filled red histogram. Entries with values above the x-axis range are shown in the last bin of each distributions. The dashed band indicates the total uncertainty on the total predicted yields. The prediction for each sample is determined from the likelihood fit performed to measure the $pp \to H \to \tau\tau$ cross-section.

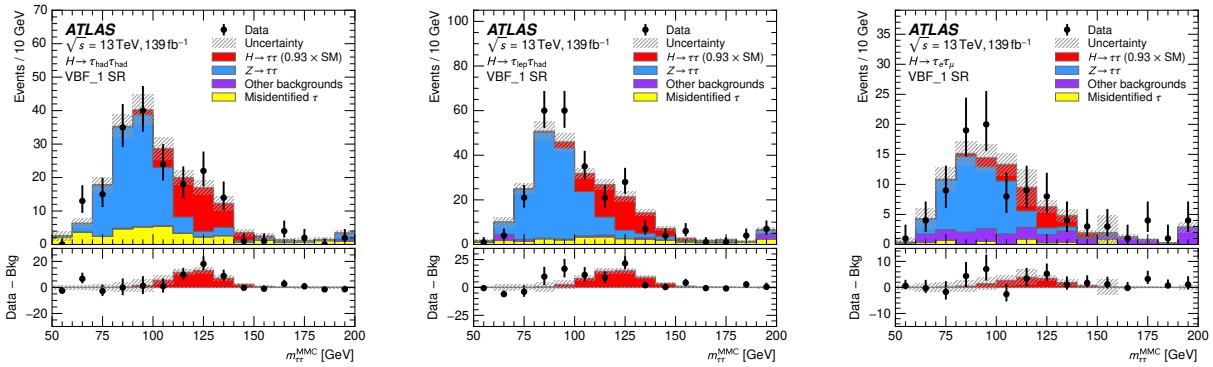

(a) $\tau_{\text{had}}\tau_{\text{had}}$ (b) $\tau_{\text{lep}}\tau_{\text{had}}$ (c) $\tau_e\tau_\mu$

Figure 10: Distribution of the reconstructed di-τ invariant mass ($m_{\tau\tau}^{\text{MMC}}$) for all events in the VBF_1 categories of (a) $\tau_{\text{had}}\tau_{\text{had}}$, (b) $\tau_{\text{lep}}\tau_{\text{had}}$ and (c) $\tau_e\tau_\mu$ signal regions. The bottom panel shows the differences between the numbers of observed data events and expected background events (black points). The observed Higgs boson signal, corresponding to $(\sigma \times B)/(\sigma \times B)_{\text{SM}} = 0.93$, is shown with a filled red histogram. Entries with values above the x-axis range are shown in the last bin of each distributions. The dashed band indicates the total uncertainty on the total predicted yields. The prediction for each sample is determined from the likelihood fit performed to measure the $pp \to H \to \tau\tau$ cross-section.

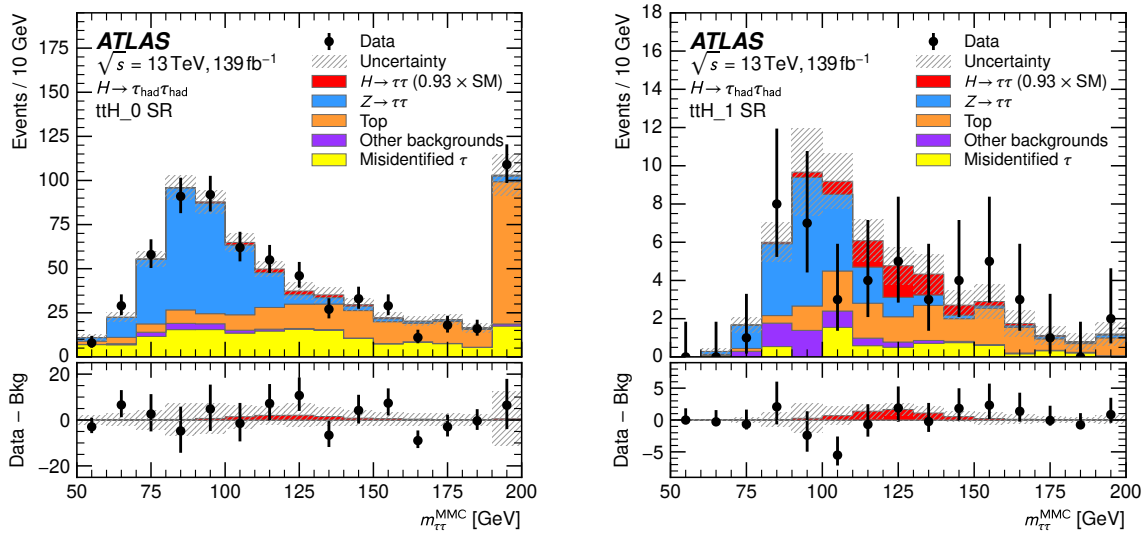

(a) ttH_0 (b) ttH_1

Figure 11: Distribution of the reconstructed di-τ invariant mass ($m_{\tau\tau}^{\text{MMC}}$) for all events in the (a) ttH_0 and (b) ttH_1 categories of the $\tau_{\text{had}}\tau_{\text{had}}$ channel. The bottom panel shows the differences between the numbers of observed data events and expected background events (black points). The observed Higgs boson signal, corresponding to $(\sigma \times B)/(\sigma \times B)_{\text{SM}} = 0.93$, is shown with a filled red histogram. Entries with values above the x-axis range are shown in the last bin of each distributions. The dashed band indicates the total uncertainty on the total predicted yields. The prediction for each sample is determined from the likelihood fit performed to measure the $pp \to H \to \tau\tau$ cross-section.

Table 8: Observed event yields and predictions as computed by the fit in the VBF, V(had)H and tt(0ℓ)$H \to \tau_{\text{had}}\tau_{\text{had}}$ signal regions of the $\tau_{\text{had}}\tau_{\text{had}}$ channel. In the VBF and V(had)H categories, the top processes are estimated with the other backgrounds (diboson, $H \to WW^*$) by the fit. Uncertainties include statistical and systematic components. The prediction for each sample is determined from the likelihood fit performed to measure the $pp \to H \to \tau\tau$ cross-section.

	VBF $\tau_{\text{had}}\tau_{\text{had}}$		V(had)H $\tau_{\text{had}}\tau_{\text{had}}$		tt(0ℓ)$H \to \tau_{\text{had}}\tau_{\text{had}}$	
	VBF_0	VBF_1	VH_0	VH_1	ttH_0	ttH_1
$Z \to \tau\tau$	2051 ± 50	114.9 ± 10.8	4636 ± 84	539 ± 24	265 ± 24	20 ± 4
Fake	1027 ± 68	39.6 ± 5.3	1627 ± 110	112 ± 10	182 ± 17	6.5 ± 1.7
Top					239 ± 26	15.2 ± 3.4
Other backgrounds	57.1 ± 5.2	1.7 ± 0.6	209 ± 12	43.13 ± 2.93	16.4 ± 0.5	5.0 ± 0.5
ggF, $H \to \tau\tau$	38.5 ± 9.5	3.2 ± 1.8	72 ± 14	6.8 ± 1.7	1.96 ± 0.41	0.42 ± 0.08
VBF, $H \to \tau\tau$	72 ± 10	40 ± 5	8.1 ± 1.3	0.5 ± 0.1	0.23 ± 0.03	< 0.01
$WH, H \to \tau\tau$	1.00 ± 0.14	< 0.01	15.2 ± 2.5	9.8 ± 1.5	0.24 ± 0.03	0.034 ± 0.005
$ZH, H \to \tau\tau$	0.8 ± 0.1	< 0.01	12.4 ± 2.3	5.4 ± 1.1	0.69 ± 0.15	0.15 ± 0.02
$t\bar{t}H, H \to \tau\tau$	0.19 ± 0.03	< 0.01	0.52 ± 0.07	0.22 ± 0.03	7.0 ± 1.6	5.4 ± 1.3
$tH, H \to \tau\tau$	0.41 ± 0.06		0.25 ± 0.03	0.07 ± 0.01	0.92 ± 0.13	0.41 ± 0.06
$bbH, H \to \tau\tau$	0.10 ± 0.02		0.14 ± 0.02	0.015 ± 0.002	0.27 ± 0.04	0.09 ± 0.02
Total background	3135 ± 84	156 ± 12	6472 ± 136	694 ± 26	703 ± 33	46.7 ± 5.3
Total signal	113 ± 15	43.6 ± 5.2	109 ± 16	23.0 ± 3.2	12 ± 2	6.6 ± 1.4
Total	3248 ± 84	200 ± 12	6580 ± 135	717 ± 26	715 ± 33	53.3 ± 5.5
Data	3318	197	6532	720	727	49

Table 9: Observed event yields and predictions as computed by the fit in the VBF and V(had)H signal regions of the $\tau_{\text{lep}}\tau_{\text{had}}$ channel. Uncertainties include statistical and systematic components. The prediction for each sample is determined from the likelihood fit performed to measure the $pp \to H \to \tau\tau$ cross-section.

	VBF $\tau_{\text{lep}}\tau_{\text{had}}$		V(had)H $\tau_{\text{lep}}\tau_{\text{had}}$	
	VBF_0	VBF_1	VH_0	VH_1
$Z \to \tau\tau$	2362 ± 59	162 ± 12	6724 ± 112	535 ± 23
Fake	611 ± 49	30 ± 3	1315 ± 126	80 ± 8
Top	107 ± 12	5.3 ± 1.5	243 ± 25	27 ± 5
Other backgrounds	139 ± 17	5.8 ± 2.4	396 ± 39	50 ± 4
ggF, $H \to \tau\tau$	71 ± 28	3.5 ± 1.2	87.3 ± 20.3	5.1 ± 2.2
VBF, $H \to \tau\tau$	84.4 ± 11.2	52 ± 6	9.3 ± 1.6	0.5 ± 0.2
$WH, H \to \tau\tau$	0.83 ± 0.11	0.011 ± 0.002	17.4 ± 2.6	8.1 ± 1.2
$ZH, H \to \tau\tau$	0.86 ± 0.12	< 0.01	13.3 ± 2.5	5.0 ± 0.9
$t\bar{t}H, H \to \tau\tau$	0.10 ± 0.01	< 0.01	0.35 ± 0.05	0.13 ± 0.02
$tH, H \to \tau\tau$	0.26 ± 0.04	0.023 ± 0.003	0.17 ± 0.03	0.030 ± 0.004
$bbH, H \to \tau\tau$	0.09 ± 0.01		0.16 ± 0.02	
Total background	3219 ± 75	203 ± 13	8677 ± 143	692 ± 24
Total signal	158 ± 30	56 ± 7	129 ± 23	19 ± 3
Total	3377 ± 76	259 ± 13	8806 ± 143	711 ± 24
Data	3402	267	8780	743

Table 10: Observed event yields and predictions as computed by the fit in the VBF and V(had)H signal regions of the $\tau_e\tau_\mu$ channel. Uncertainties include statistical and systematic components. The prediction for each sample is determined from the likelihood fit performed to measure the $pp \to H \to \tau\tau$ cross-section.

	VBF $\tau_e\tau_\mu$		V(had)H $\tau_e\tau_\mu$	
	VBF_0	VBF_1	VH_0	VH_1
$Z \to \tau\tau$	820 ± 29	49.3 ± 6.5	2424 ± 58	186 ± 13
Fake	90 ± 21	3.3 ± 5.3	214 ± 42	33 ± 14
Top	165 ± 15	9 ± 2	346 ± 29	33 ± 5
Other backgrounds	96.1 ± 8.5	11.9 ± 1.6	259 ± 23	28 ± 2
ggF, $H \to \tau\tau$	12.7 ± 3.2	1.04 ± 0.31	26 ± 5	1.8 ± 0.6
VBF, $H \to \tau\tau$	23 ± 3	14.3 ± 1.8	2.41 ± 0.43	0.13 ± 0.02
$WH, H \to \tau\tau$	0.21 ± 0.03		4.3 ± 0.7	2.45 ± 0.42
$ZH, H \to \tau\tau$	0.14 ± 0.02		3.6 ± 0.8	1.5 ± 0.3
$t\bar{t}H, H \to \tau\tau$	< 0.01	< 0.01	0.08 ± 0.01	0.021 ± 0.003
$tH, H \to \tau\tau$	0.13 ± 0.02	0.014 ± 0.002	0.038 ± 0.005	0.018 ± 0.002
$bbH, H \to \tau\tau$	0.026 ± 0.004		0.046 ± 0.006	
Total background	1154 ± 35	66.4 ± 8.5	3230 ± 63	280 ± 18
Total signal	51.9 ± 5.4	22.4 ± 1.8	50 ± 7	7.1 ± 0.9
Total	1206 ± 35	88.8 ± 8.6	3280 ± 63	287 ± 18
Data	1215	98	3277	286

Table 11: Observed event yields and predictions as computed by the fit in the boost signal regions of the $\tau_{\text{had}}\tau_{\text{had}}$ channel. Uncertainties include statistical and systematic components. The prediction for each sample is determined from the likelihood fit performed to measure the $pp \to H \to \tau\tau$ cross-section.

	Boost $\tau_{\text{had}}\tau_{\text{had}}$					
$p_{\text{T}}(H)$ [GeV]	[100, 120]		[120, 200]		[200, 300]	[300, ∞[
$N_{\text{jets}}(p_{\text{T}} > 30\,\text{GeV})$	= 1	≥ 2	= 1	≥ 2	≥ 1	≥ 1
$Z \to \tau\tau$	5635 ± 115	2640 ± 67	11 863 ± 134	10 076 ± 125	7252 ± 93	973 ± 30
Fake	3388 ± 224	1729 ± 118	2312 ± 155	2072 ± 140	293 ± 32	54 ± 20
Other backgrounds	61 ± 9	74.2 ± 11.3	116 ± 19	251 ± 14	157.3 ± 10.5	53.6 ± 5.5
ggF, $H \to \tau\tau$	54.4 ± 9.7	23.1 ± 4.1	112.8 ± 20.5	109.1 ± 20.6	96.2 ± 17.2	30 ± 7
VBF, $H \to \tau\tau$	11.3 ± 2.0	5.8 ± 0.9	27.6 ± 4.7	24.6 ± 4.2	23.7 ± 3.6	7.3 ± 1.1
$WH, H \to \tau\tau$	2.1 ± 0.6	1.5 ± 0.3	3.8 ± 1.1	7.0 ± 1.1	4.6 ± 0.7	2.5 ± 0.7
$ZH, H \to \tau\tau$	1.4 ± 0.3	1.1 ± 0.3	2.7 ± 0.9	5.3 ± 1.0	3.7 ± 0.5	1.5 ± 0.2
$t\bar{t}H, H \to \tau\tau$	< 0.01	0.27 ± 0.04	< 0.01	1.01 ± 0.14	0.8 ± 0.1	0.35 ± 0.05
$tH, H \to \tau\tau$	0.023 ± 0.003	0.06 ± 0.01	0.029 ± 0.004	0.30 ± 0.04	0.39 ± 0.05	0.09 ± 0.01
$bbH, H \to \tau\tau$	0.19 ± 0.03	0.07 ± 0.01	0.21 ± 0.03	0.30 ± 0.04	0.21 ± 0.03	0.05 ± 0.01
Total background	9084 ± 244	4444 ± 132	14 291 ± 199	12 398 ± 188	7702 ± 96	1080 ± 32
Total signal	69.5 ± 11.0	32 ± 5	147 ± 23	148 ± 22	130 ± 18	41.7 ± 7.2
Total	9153.5 ± 243.5	4476 ± 132	14 438 ± 198	12 546 ± 187	7832 ± 95	1122 ± 32
Data	9163	4503	14389	12585	7800	1124

Table 12: Observed event yields and predictions as computed by the fit in the boost signal regions of the $\tau_{\text{lep}}\tau_{\text{had}}$ channel. Uncertainties include statistical and systematic components. The prediction for each sample is determined from the likelihood fit performed to measure the $pp \to H \to \tau\tau$ cross-section.

	Boost $\tau_{\text{lep}}\tau_{\text{had}}$					
$p_{\text{T}}(H)$ [GeV]	[100, 120]		[120, 200]		[200, 300]	[300, ∞[
$N_{\text{jets}}(p_{\text{T}} > 30\,\text{GeV})$	= 1	≥ 2	= 1	≥ 2	≥ 1	≥ 1
$Z \to \tau\tau$	5583 ± 100	3228 ± 69	10 927 ± 130	9546 ± 118	7195 ± 92	2413 ± 46
Fake	1119 ± 58	832 ± 44	1324 ± 76	1434 ± 81	536 ± 35	139 ± 12
Top	65 ± 7	123 ± 16	81 ± 13	317 ± 25	129 ± 12	52 ± 8
Other backgrounds	214 ± 40	177 ± 22	374 ± 40	447 ± 33	300 ± 17	164 ± 6
ggF, $H \to \tau\tau$	45.4 ± 11.6	44.8 ± 15.2	99.5 ± 19.7	123.5 ± 29.4	91.2 ± 24.4	33.5 ± 8.9
VBF, $H \to \tau\tau$	12.1 ± 2.0	7.2 ± 1.1	26.9 ± 4.1	23.6 ± 3.7	21.6 ± 3.2	8.6 ± 1.4
$WH, H \to \tau\tau$	1.7 ± 0.3	2.2 ± 0.6	3.5 ± 2.0	6.5 ± 1.2	4.4 ± 0.8	3.3 ± 1.0
$ZH, H \to \tau\tau$	1.2 ± 0.3	1.3 ± 0.2	2.4 ± 0.3	4.7 ± 0.6	3.0 ± 0.4	1.8 ± 0.2
$t\bar{t}H, H \to \tau\tau$	< 0.01	0.11 ± 0.01	< 0.01	0.55 ± 0.08	0.35 ± 0.05	0.22 ± 0.03
$tH, H \to \tau\tau$	< 0.01	0.09 ± 0.01	0.018 ± 0.002	0.28 ± 0.04	0.17 ± 0.02	0.042 ± 0.006
$bbH, H \to \tau\tau$	0.13 ± 0.02	0.13 ± 0.02	0.17 ± 0.02	0.21 ± 0.03	0.12 ± 0.02	0.04 ± 0.01
Total background	6981 ± 112	4360 ± 82	12 706 ± 143	11 743 ± 135	8160 ± 94	2768 ± 49
Total signal	61 ± 13	56.1 ± 15.5	133 ± 22	160 ± 31	121.6 ± 25.1	47.8 ± 9.2
Total	7042 ± 112	4416 ± 81	12 839 ± 143	11 903 ± 134	8281 ± 93	2816 ± 49
Data	7094	4374	12779	11 886	8236	2848

Table 13: Observed event yields and predictions as computed by the fit in the boost signal regions of the $\tau_e\tau_\mu$ channel. Uncertainties include statistical and systematic components. The prediction for each sample is determined from the likelihood fit performed to measure the $pp \to H \to \tau\tau$ cross-section.

	Boost $\tau_e\tau_\mu$																	
$p_{\mathrm{T}}(H)$ [GeV]	[100, 120]						[120, 200]						[200, 300]			[300, ∞[		
$N_{\mathrm{jets}}(p_{\mathrm{T}} > 30\,\mathrm{GeV})$	= 1			≥ 2			= 1			≥ 2			≥ 1			≥ 1		
$Z \to \tau\tau$	2642	±	64	1523	±	42	3913	±	69	3453	±	68	1734	±	37	469	±	20
Fake	101	±	31	85	±	23	117	±	36	179	±	42	88	±	24	37	±	13
Top	101	±	8	187	±	20	157	±	11	569	±	44	258	±	16	104	±	11
Other backgrounds	118	±	17	101	±	16	273	±	14	325	±	30	294	±	8	173	±	5
ggF, $H \to \tau\tau$	16.6	±	3.2	11	±	2	35	±	7	36.8	±	7.1	25.5	±	4.6	8.7	±	2.2
VBF, $H \to \tau\tau$	3.4	±	0.6	2.2	±	0.3	8.7	±	1.6	7.8	±	1.1	6.2	±	0.9	2.1	±	0.3
$WH, H \to \tau\tau$	0.44	±	0.06	0.57	±	0.13	1.35	±	0.56	2.22	±	0.57	1.29	±	0.18	0.87	±	0.35
$ZH, H \to \tau\tau$	0.29	±	0.04	0.33	±	0.05	0.73	±	0.10	1.57	±	0.22	0.85	±	0.12	0.41	±	0.06
$t\bar{t}H, H \to \tau\tau$	< 0.01			0.029	±	0.004	< 0.01			0.20	±	0.03	0.08	±	0.01	0.07	±	0.01
$tH, H \to \tau\tau$				0.08	±	0.01	0.025	±	0.003	0.13	±	0.02	0.11	±	0.02	0.033	±	0.005
$bbH, H \to \tau\tau$	0.038	±	0.005	0.026	±	0.004	0.06	±	0.01	0.11	±	0.01	0.06	±	0.01	0.017	±	0.002
Total background	2952	±	65	1890	±	47	4439	±	70	4506	±	75	2357	±	43	777	±	25
Total signal	30	±	4	20	±	3	65	±	9	69	±	10	51	±	7	18	±	3
Total	2982	±	65	1910	±	47	4504	±	70	4575	±	75	2407	±	42	795	±	25
Data	2973			1877			4458			4594			2325			743		

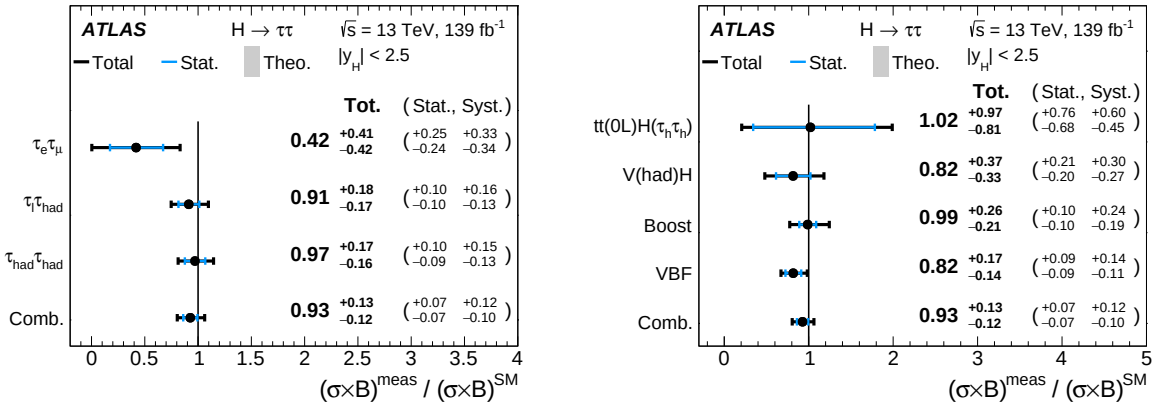

(a) (b)

Figure 12: The measured values for $\sigma_H \times B(H \to \tau\tau)$ relative to the SM expectations when only the data of (a) individual channels or (b) individual categories are used. The total $\pm 1\sigma$ uncertainty in the measurement is indicated by the black error bars, with the individual contribution from the statistical uncertainty in blue. The results have been extracted performing a fit for the inclusive cross-section measurement.

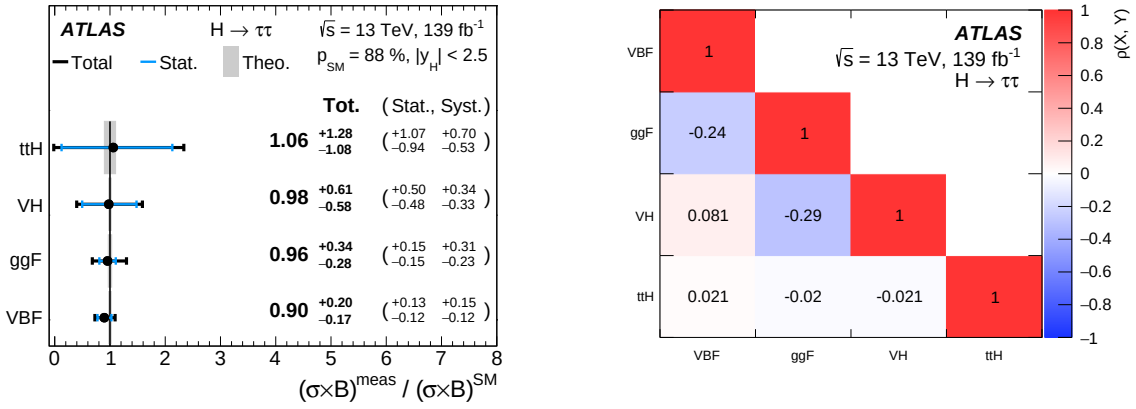

(a) (b)

Figure 13: (a) The measured values for $\sigma_H \times B(H \to \tau\tau)$ relative to the SM expectations in the four dominant production modes. The total $\pm 1\sigma$ uncertainty in the measurement is indicated by the black error bars, with the individual contribution from the statistical uncertainty in blue. (b) The measured correlations between each parameter of interest in the measurement of the cross-sections per production mode. The results have been extracted performing a fit for the production mode cross-section measurements. The measured values for $\sigma_H \times B(H \to \tau\tau)$ along with the corresponding correlation matrix are available in the HEPData repository [167].

Table 14: Best-fit values and uncertainties for the $pp \to H \to \tau\tau$ cross-section measurement and the measurement in the four dominant production modes. All measurements include the branching ratio of $H \to \tau\tau$ and refers to true Higgs boson rapidity $|y_H| < 2.5$. The SM predictions for each region, computed using the inclusive cross-section calculations and the simulated event samples are also shown. The contributions to the total uncertainty in the measurements from statistical (Stat. unc.) or systematic uncertainties (Syst. unc.) in the signal prediction (Th. sig.), background prediction (Th. bkg.), and in experimental performance (Exp.) are given separately. Each uncertainty is reported as the average of its upward and downward fluctuations. The total systematic uncertainty, equal to the difference in quadrature between the total uncertainty and the statistical uncertainty, differs from the sum in quadrature of the Th. sig., Th. bkg., and Exp. systematic uncertainties due to correlations.

Production Mode	SM prediction	Result	Stat. unc.	Syst. unc. [pb]		
	[pb]	[pb]	[pb]	Th. sig.	Th. bkg.	Exp.
$t\bar{t}H$	0.0313 ± 0.0032	0.033 ± 0.037	± 0.031	± 0.010	± 0.010	± 0.010
VH	0.1176 ± 0.0025	0.115 ± 0.070	± 0.058	± 0.016	± 0.005	± 0.021
ggF	2.77 ± 0.09	2.65 ± 0.85	± 0.41	± 0.56	± 0.07	± 0.45
VBF	0.220 ± 0.005	0.197 ± 0.041	± 0.028	± 0.024	± 0.005	± 0.012
$pp \to H$	3.17 ± 0.09	2.94 ± 0.41	± 0.21	± 0.26	± 0.05	± 0.19

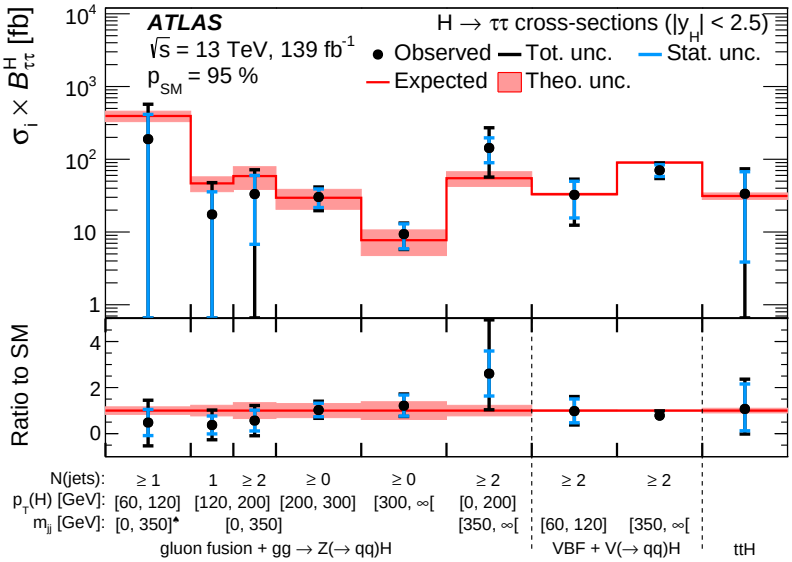

(a)

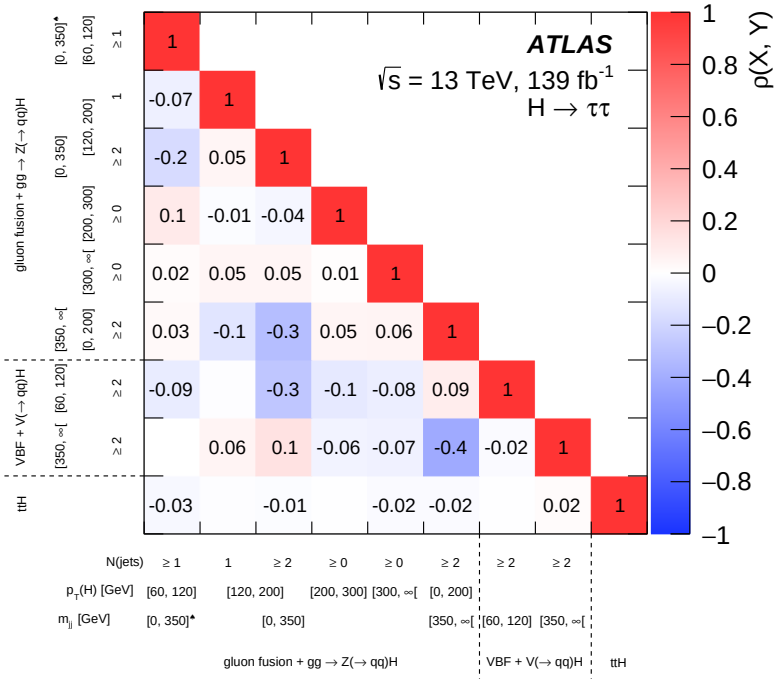

(b)

Figure 14: (a) The measured values for $\sigma_H \times B(H \to \tau\tau)$ relative to the SM expectations in the nine fiducial volumes defined in the STXS measurement. Also shown is the result from the combined fit. The total $\pm 1\sigma$ uncertainty in the measurement is indicated by the black error bars, with the individual contribution from the statistical uncertainty in blue. (b) The measured correlations between each pair of parameters of interest in the STXS measurement. The spades symbol (♠) indicates that the criteria for m_{jj} only apply to events with at least two reconstructed jets. The measured values for $\sigma_H \times B(H \to \tau\tau)$ along with the corresponding correlation matrix are available in the HEPData repository [167].

Table 15: Best-fit values and uncertainties for the $pp \to H \to \tau\tau$ cross-sections, in the reduced *stage 1.2* STXS scheme described in the text. The EW production mode includes vector-boson fusion and $qq \to V(\to qq)H$ processes. All measurements include the branching ratio of $H \to \tau\tau$ and refers to true Higgs boson rapidity $|y_H| < 2.5$. The SM predictions for each region, computed using the inclusive cross-section calculations and the simulated event samples are also shown. The contributions to the total uncertainty in the measurements from statistical (Stat. unc.) or systematic uncertainties (Syst. unc.) in the signal prediction (Th. sig.), background prediction (Th. bkg.), and in experimental performance (Exp.) are given separately. Each uncertainty is reported as the average of its upward and downward fluctuations. The total systematic uncertainty, equal to the difference in quadrature between the total uncertainty and the statistical uncertainty, differs from the sum in quadrature of the Th. sig., Th. bkg., and Exp. systematic uncertainties due to correlations. The spades symbol (♠) indicates that the criteria for m_{jj} only apply to events with at least two reconstructed jets.

STXS bin				SM prediction	Result	Stat. unc.	Syst. unc. [fb]		
Process	m_{jj} [GeV]	$p_{\mathrm{T}}(H)$ [GeV]	N_{jets}	[fb]	[fb]	[fb]	Th. sig.	Th. bkg.	Exp.
ggF + $gg \to Z(\to qq)H$	[0, 350]♠	[60, 120]	≥ 1	394 ± 60	189 ± 390	±220	±59	±152	±240
		[120, 200]	$= 1$	47 ± 11	17 ± 30	±18	±4	±4	±16
	[0, 350]	[120, 200]	≥ 2	59 ± 20	33 ± 39	±27	±10	±10	±23
		[200, 300]	≥ 0	30 ± 9	30.3 ± 11.0	±8.6	±2.9	±0.8	±5.6
		[300, ∞[	≥ 0	7.7 ± 3.0	9.35 ± 3.80	±3.50	±1.00	±0.22	±1.20
	[350, ∞[	[0, 200]	≥ 2	55 ± 13	143 ± 110	±54	±58	±6	±71
EW	[60, 120]		≥ 2	33.1 ± 1.1	32 ± 20	±17	±4	±2	±6
	[350, ∞[		≥ 2	90.1 ± 2.2	71 ± 17	±13	±10	±2	±4
$t\bar{t}H$				31.3 ± 3.2	34 ± 37	±32	±7	±10	±8

9 Conclusion

Measurements of production cross-sections for Standard Model Higgs bosons decaying into a pair of τ-leptons are presented. The measurements use data collected by the ATLAS experiment from proton–proton collisions in Run 2 of the LHC. The data correspond to an integrated luminosity of 139 fb^{-1}.

All measurements include the branching ratio of $H \to \tau\tau$ and refer to true Higgs boson rapidity $|y_H| < 2.5$. The $pp \to H \to \tau\tau$ cross-section is measured to be $2.94 \pm 0.21(\text{stat})^{+0.37}_{-0.32}(\text{syst})$ pb, in agreement with the SM prediction of 3.17 ± 0.09 pb. The observed (expected) uncertainty in the $pp \to H \to \tau\tau$ cross-section determination was reduced from $^{+28}_{-25}$ % ($^{+27}_{-24}$ %) in the measurement reported in Ref. [22] to ±13.9% (±13.2%) in this work. In particular, the impact of the systematic uncertainties was reduced by approximately a factor of two from ±21.5% to ±12%.

Cross-sections are determined separately for the four main production modes: $2.65 \pm 0.41(\text{stat})^{+0.91}_{-0.67}(\text{syst})$ pb for the gluon–gluon fusion mode, $0.197 \pm 0.028(\text{stat})^{+0.032}_{-0.026}(\text{syst})$ pb for the vector-boson fusion mode, $0.115 \pm 0.058(\text{stat})^{+0.042}_{-0.040}(\text{syst})$ pb for production with a vector boson, and $0.033 \pm 0.031(\text{stat})^{+0.022}_{-0.017}(\text{syst})$ pb for production with a top-quark pair.

Measurements are also performed as a function of key kinematic properties of the reconstructed event. Cross-sections of the production of a Higgs boson decaying into τ-leptons are measured as a function of the Higgs boson transverse momentum, the number of jets produced in association with the Higgs boson, and the invariant mass of the two leading jets when applicable. They represent the most detailed study of Higgs boson production in the di-τ decay channel to date. The measurements attain an uncertainty of ±24% for electroweak production with two jets of invariant mass greater than 350 GeV. The ggF production mode is measured with an uncertainty of ±36% and ±40% when the Higgs boson transverse momentum is between 200 and 300 GeV and above 300 GeV respectively. All measurements are in agreement with the Standard Model predictions.

Acknowledgements

We thank CERN for the very successful operation of the LHC, as well as the support staff from our institutions without whom ATLAS could not be operated efficiently.

We acknowledge the support of ANPCyT, Argentina; YerPhI, Armenia; ARC, Australia; BMWFW and FWF, Austria; ANAS, Azerbaijan; SSTC, Belarus; CNPq and FAPESP, Brazil; NSERC, NRC and CFI, Canada; CERN; ANID, Chile; CAS, MOST and NSFC, China; Minciencias, Colombia; MSMT CR, MPO CR and VSC CR, Czech Republic; DNRF and DNSRC, Denmark; IN2P3-CNRS and CEA-DRF/IRFU, France; SRNSFG, Georgia; BMBF, HGF and MPG, Germany; GSRI, Greece; RGC and Hong Kong SAR, China; ISF and Benoziyo Center, Israel; INFN, Italy; MEXT and JSPS, Japan; CNRST, Morocco; NWO, Netherlands; RCN, Norway; MEiN, Poland; FCT, Portugal; MNE/IFA, Romania; JINR; MES of Russia and NRC KI, Russian Federation; MESTD, Serbia; MSSR, Slovakia; ARRS and MIZŠ, Slovenia; DSI/NRF, South Africa; MICINN, Spain; SRC and Wallenberg Foundation, Sweden; SERI, SNSF and Cantons of Bern and Geneva, Switzerland; MOST, Taiwan; TAEK, Turkey; STFC, United Kingdom; DOE and NSF, United States of America. In addition, individual groups and members have received support from BCKDF, CANARIE, Compute Canada and CRC, Canada; COST, ERC, ERDF, Horizon 2020 and Marie Skłodowska-Curie Actions, European Union; Investissements d'Avenir Labex, Investissements d'Avenir Idex and ANR, France; DFG and AvH Foundation, Germany; Herakleitos, Thales and Aristeia programmes

co-financed by EU-ESF and the Greek NSRF, Greece; BSF-NSF and GIF, Israel; Norwegian Financial Mechanism 2014-2021, Norway; NCN and NAWA, Poland; La Caixa Banking Foundation, CERCA Programme Generalitat de Catalunya and PROMETEO and GenT Programmes Generalitat Valenciana, Spain; Göran Gustafssons Stiftelse, Sweden; The Royal Society and Leverhulme Trust, United Kingdom.

The crucial computing support from all WLCG partners is acknowledged gratefully, in particular from CERN, the ATLAS Tier-1 facilities at TRIUMF (Canada), NDGF (Denmark, Norway, Sweden), CC-IN2P3 (France), KIT/GridKA (Germany), INFN-CNAF (Italy), NL-T1 (Netherlands), PIC (Spain), ASGC (Taiwan), RAL (UK) and BNL (USA), the Tier-2 facilities worldwide and large non-WLCG resource providers. Major contributors of computing resources are listed in Ref. [168].

Appendix

Figures 15 to 20 show all distributions that enter the likelihood fit with the best-fit parameters derived from the fit with a single parameter of interest (inclusive cross-section measurement).

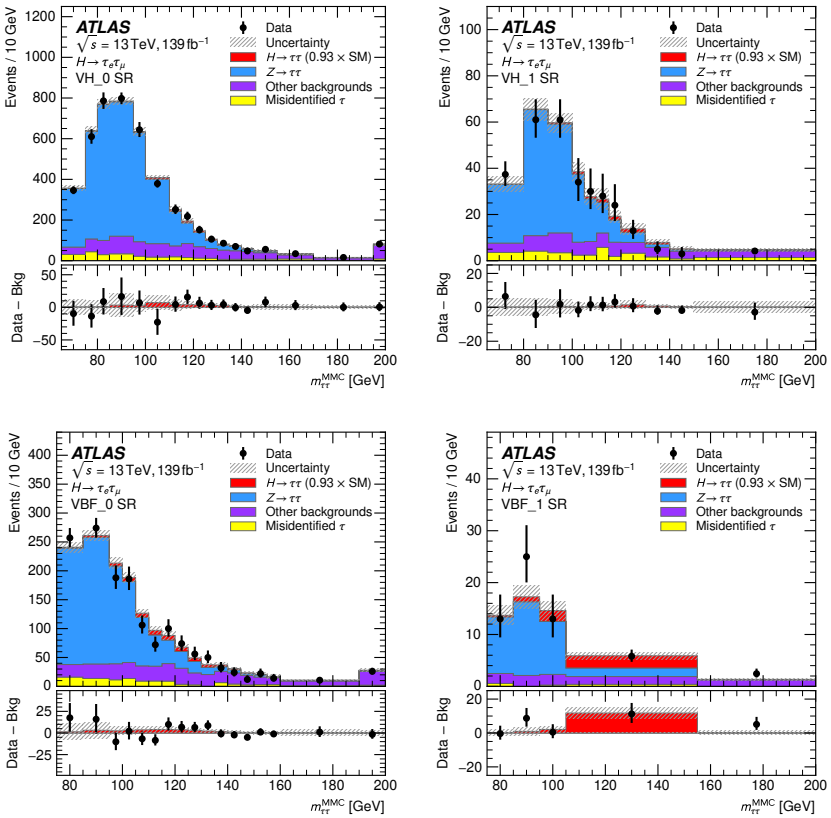

Figure 15: Distribution of the reconstructed di-τ invariant mass ($m_{\tau\tau}^{\mathrm{MMC}}$) for all events in the V(had)H and VBF categories of the $\tau_e\tau_\mu$ channel. The bottom panel shows the differences between the numbers of observed data events and expected background events (black points). The observed Higgs boson signal, corresponding to $(\sigma\times B)/(\sigma\times B)_{\mathrm{SM}} = 0.93$, is shown with a filled red histogram. Entries with values above the x-axis range are shown in the last bin of each distributions. The dashed band indicates the total uncertainty on the total predicted yields. The prediction for each sample is determined from the likelihood fit performed to measure the $pp\to H\to\tau\tau$ cross-section.

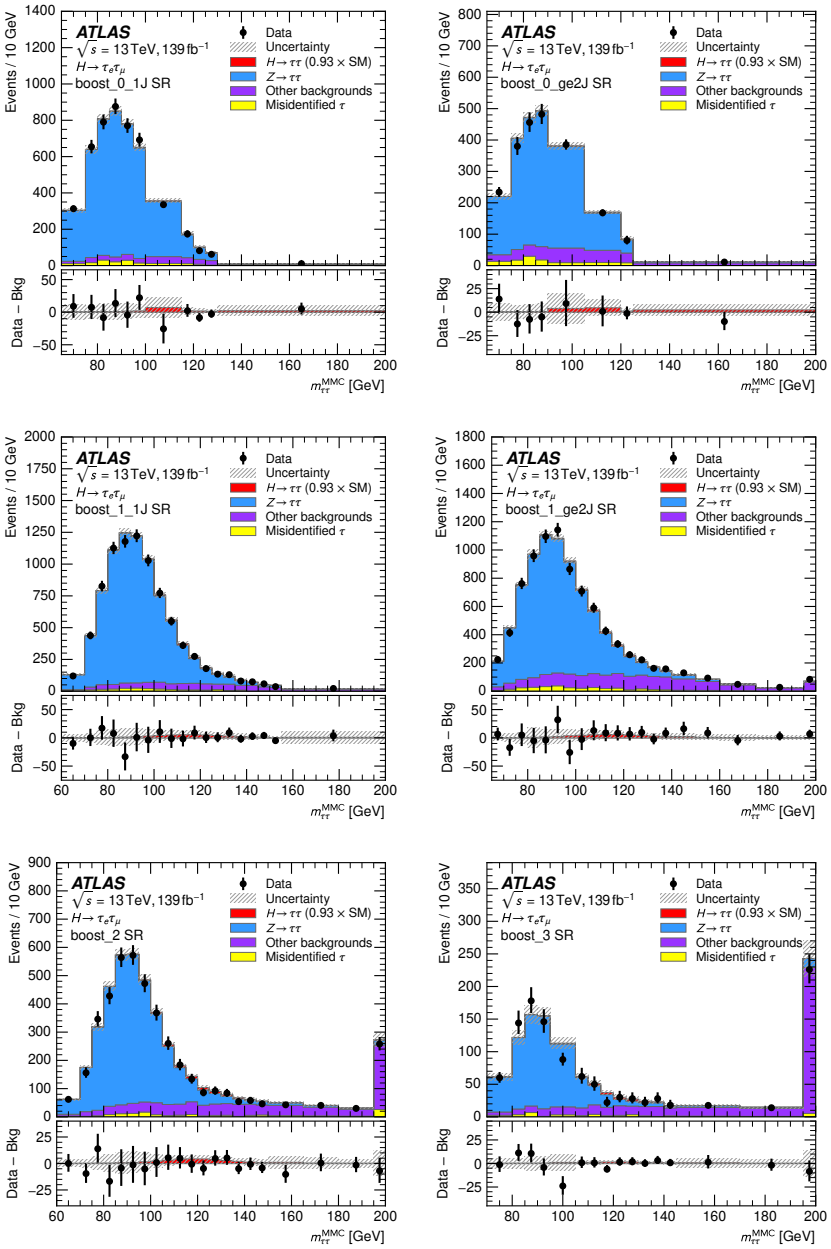

Figure 16: Distribution of the reconstructed di-τ invariant mass ($m_{\tau\tau}^{\mathrm{MMC}}$) for all events in the boost categories of the $\tau_e\tau_\mu$ channel. The bottom panel shows the differences between the numbers of observed data events and expected background events (black points). The observed Higgs boson signal, corresponding to $(\sigma \times B)/(\sigma \times B)_{\mathrm{SM}} = 0.93$, is shown with a filled red histogram. Entries with values above the x-axis range are shown in the last bin of each distributions. The dashed band indicates the total uncertainty on the total predicted yields. The prediction for each sample is determined from the likelihood fit performed to measure the $pp \to H \to \tau\tau$ cross-section.

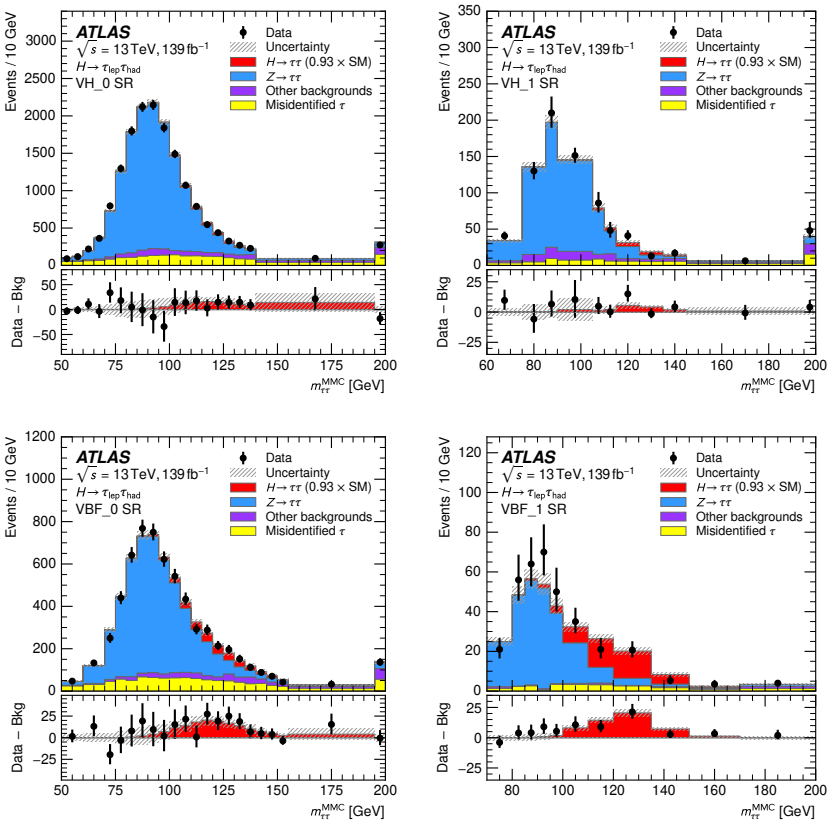

Figure 17: Distribution of the reconstructed di-τ invariant mass ($m_{\tau\tau}^{\text{MMC}}$) for all events in the V(had)H and VBF categories of the $\tau_{\text{lep}}\tau_{\text{had}}$ channel. The bottom panel shows the differences between the numbers of observed data events and expected background events (black points). The observed Higgs boson signal, corresponding to $(\sigma \times B)/(\sigma \times B)_{\text{SM}} = 0.93$, is shown with a filled red histogram. Entries with values above the x-axis range are shown in the last bin of each distributions. The dashed band indicates the total uncertainty on the total predicted yields. The prediction for each sample is determined from the likelihood fit performed to measure the $pp \to H \to \tau\tau$ cross-section.

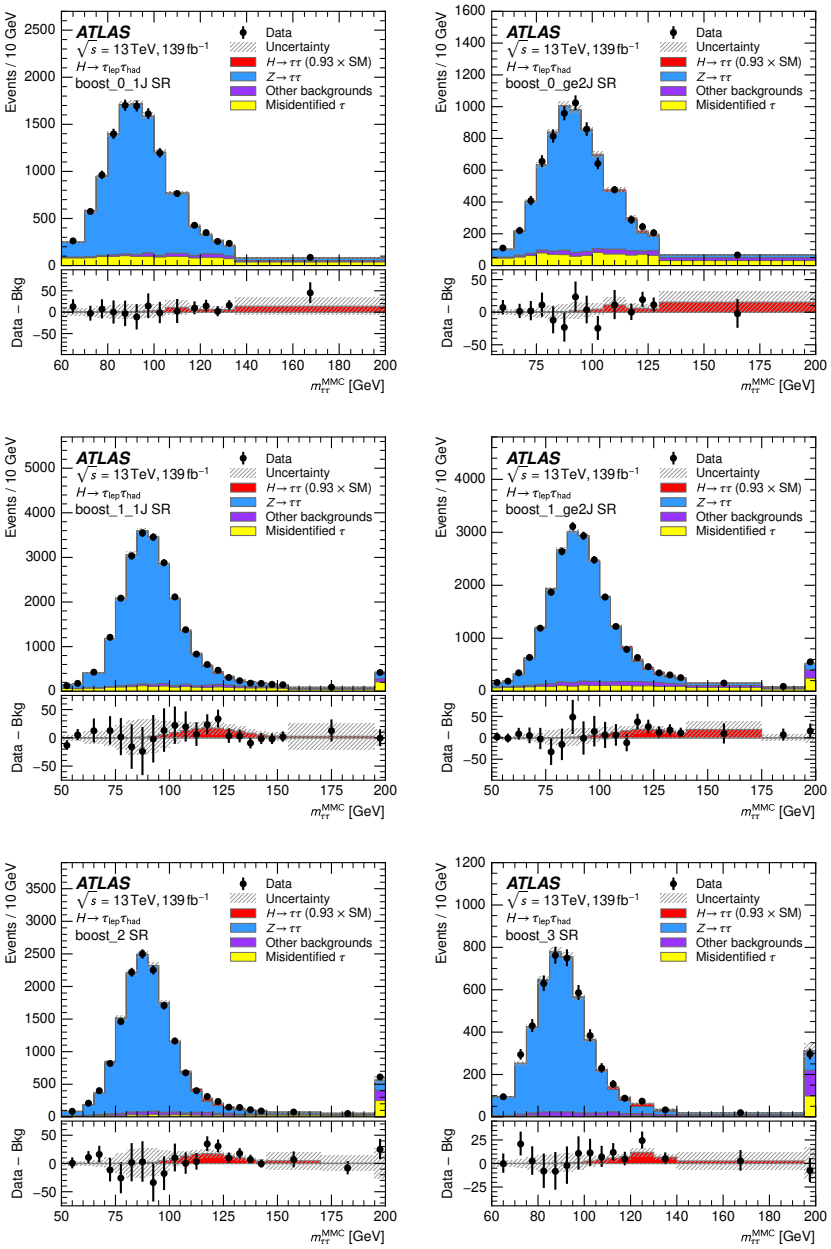

Figure 18: Distribution of the reconstructed di-τ invariant mass ($m_{\tau\tau}^{\mathrm{MMC}}$) for all events in the boost categories of the $\tau_{\mathrm{lep}}\tau_{\mathrm{had}}$ channel. The bottom panel shows the differences between the numbers of observed data events and expected background events (black points). The observed Higgs boson signal, corresponding to $(\sigma \times B)/(\sigma \times B)_{\mathrm{SM}} = 0.93$, is shown with a filled red histogram. Entries with values above the x-axis range are shown in the last bin of each distributions. The dashed band indicates the total uncertainty on the total predicted yields. The prediction for each sample is determined from the likelihood fit performed to measure the $pp \to H \to \tau\tau$ cross-section.

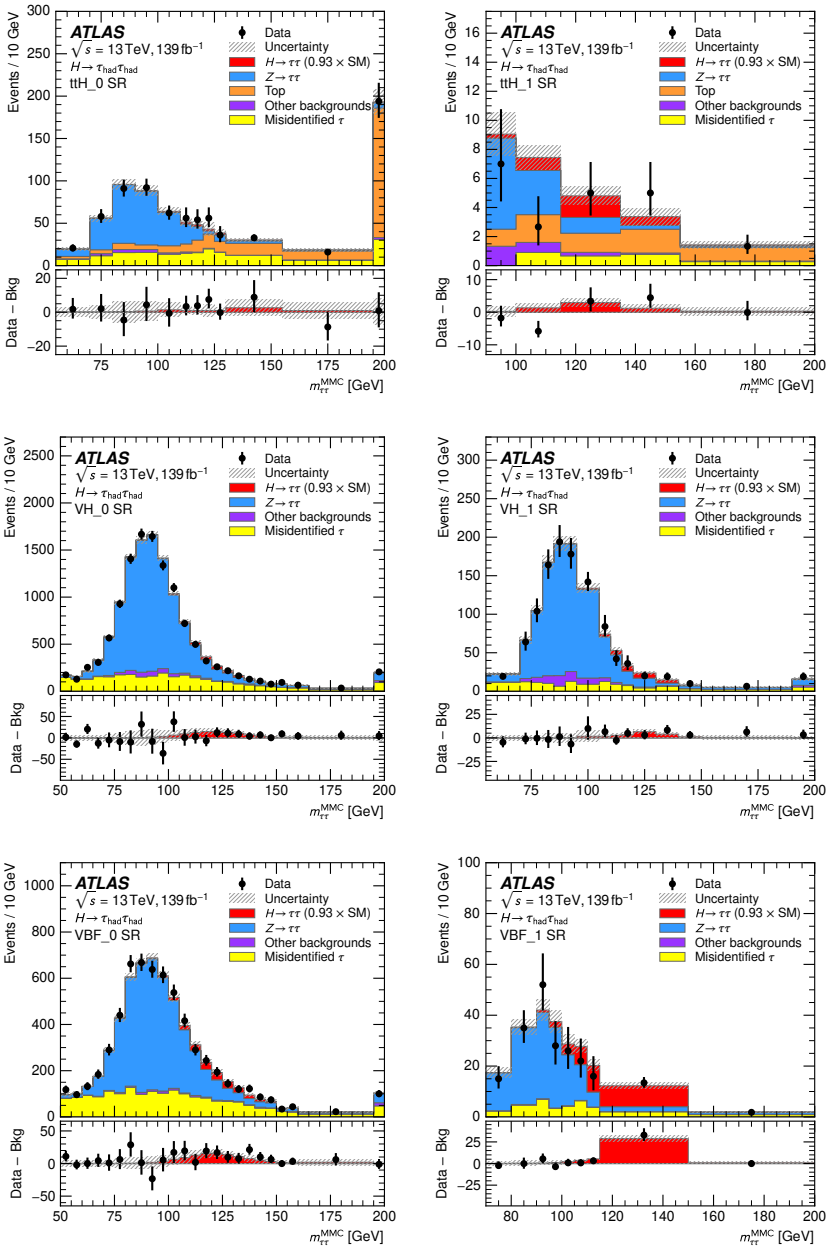

Figure 19: Distribution of the reconstructed di-τ invariant mass ($m_{\tau\tau}^{\mathrm{MMC}}$) for all events in the ttH, V(had)H and VBF categories of the $\tau_{\mathrm{had}}\tau_{\mathrm{had}}$ channel. The bottom panel shows the differences between the numbers of observed data events and expected background events (black points). The observed Higgs boson signal, corresponding to $(\sigma \times B)/(\sigma \times B)_{\mathrm{SM}} = 0.93$, is shown with a filled red histogram. Entries with values above the x-axis range are shown in the last bin of each distributions. The dashed band indicates the total uncertainty on the total predicted yields. The prediction for each sample is determined from the likelihood fit performed to measure the $pp \to H \to \tau\tau$ cross-section.

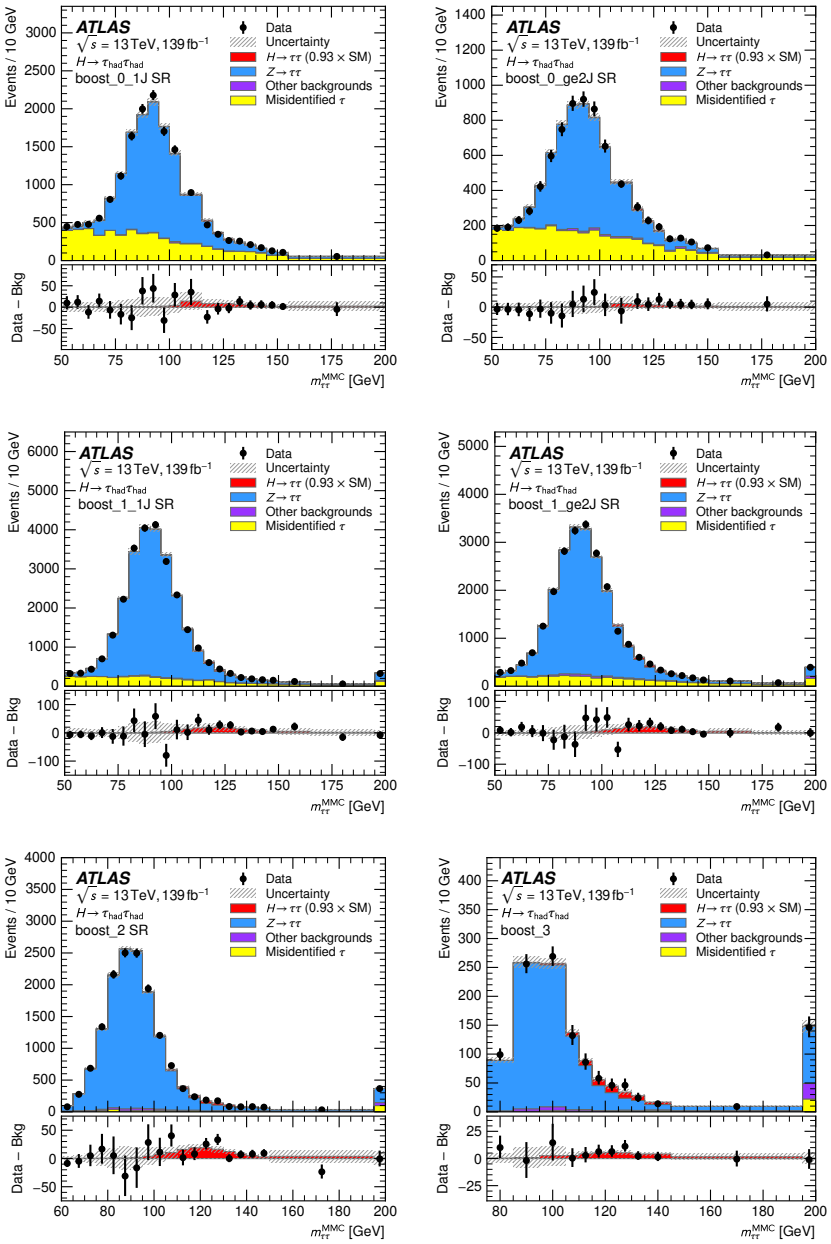

Figure 20: Distribution of the reconstructed di-τ invariant mass ($m_{\tau\tau}^{\mathrm{MMC}}$) for all events in the boost categories of the $\tau_{\mathrm{had}}\tau_{\mathrm{had}}$ channel. The bottom panel shows the differences between the numbers of observed data events and expected background events (black points). The observed Higgs boson signal, corresponding to $(\sigma \times B)/(\sigma \times B)_{\mathrm{SM}} = 0.93$, is shown with a filled red histogram. Entries with values above the x-axis range are shown in the last bin of each distributions. The dashed band indicates the total uncertainty on the total predicted yields. The prediction for each sample is determined from the likelihood fit performed to measure the $pp \to H \to \tau\tau$ cross-section.

References

[1] F. Englert and R. Brout, *Broken Symmetry and the Mass of Gauge Vector Mesons*, Phys. Rev. Lett. **13** (1964) 321.

[2] P. W. Higgs, *Broken symmetries, massless particles and gauge fields*, Phys. Lett. **12** (1964) 132.

[3] P. W. Higgs, *Broken Symmetries and the Masses of Gauge Bosons*, Phys. Rev. Lett. **13** (1964) 508.

[4] G. Guralnik, C. Hagen and T. Kibble, *Global Conservation Laws and Massless Particles*, Phys. Rev. Lett. **13** (1964) 585.

[5] P. W. Higgs, *Spontaneous Symmetry Breakdown without Massless Bosons*, Phys. Rev. **145** (1966) 1156.

[6] T. Kibble, *Symmetry Breaking in Non-Abelian Gauge Theories*, Phys. Rev. **155** (1967) 1554.

[7] ATLAS Collaboration, *Observation of a new particle in the search for the Standard Model Higgs boson with the ATLAS detector at the LHC*, Phys. Lett. B **716** (2012) 1, arXiv: 1207.7214 [hep-ex].

[8] CMS Collaboration, *Observation of a new boson at a mass of 125 GeV with the CMS experiment at the LHC*, Phys. Lett. B **716** (2012) 30, arXiv: 1207.7235 [hep-ex].

[9] L. Evans and P. Bryant, *LHC Machine*, JINST **3** (2008) S08001.

[10] ATLAS and CMS Collaborations, *Combined Measurement of the Higgs Boson Mass in pp Collisions at $\sqrt{s} = 7$ and 8 TeV with the ATLAS and CMS Experiments*, Phys. Rev. Lett. **114** (2015) 191803, arXiv: 1503.07589 [hep-ex].

[11] ATLAS Collaboration, *Measurements of Higgs boson properties in the diphoton decay channel with $36\,fb^{-1}$ of pp collision data at $\sqrt{s} = 13$ TeV with the ATLAS detector*, Phys. Rev. D **98** (2018) 052005, arXiv: 1802.04146 [hep-ex].

[12] ATLAS Collaboration, *Measurement of the Higgs boson coupling properties in the $H \to ZZ^* \to 4\ell$ decay channel at $\sqrt{s} = 13$ TeV with the ATLAS detector*, JHEP **03** (2018) 095, arXiv: 1712.02304 [hep-ex].

[13] ATLAS Collaboration, *Measurement of inclusive and differential cross sections in the $H \to ZZ^* \to 4\ell$ decay channel in pp collisions at $\sqrt{s} = 13$ TeV with the ATLAS detector*, JHEP **10** (2017) 132, arXiv: 1708.02810 [hep-ex].

[14] ATLAS Collaboration, *Measurement of the Higgs boson mass in the $H \to ZZ^* \to 4\ell$ and $H \to \gamma\gamma$ channels with $\sqrt{s} = 13$ TeV pp collisions using the ATLAS detector*, Phys. Lett. B **784** (2018) 345, arXiv: 1806.00242 [hep-ex].

[15] ATLAS Collaboration, *Combined measurement of differential and total cross sections in the $H \to \gamma\gamma$ and the $H \to ZZ^* \to 4\ell$ decay channels at $\sqrt{s} = 13$ TeV with the ATLAS detector*, Phys. Lett. B **786** (2018) 114, arXiv: 1805.10197 [hep-ex].

[16] ATLAS Collaboration, *Measurements of gluon-gluon fusion and vector-boson fusion Higgs boson production cross-sections in the $H \to WW^* \to e\nu\mu\nu$ decay channel in pp collisions at $\sqrt{s} = 13$ TeV with the ATLAS detector*, Phys. Lett. B **789** (2019) 508, arXiv: 1808.09054 [hep-ex].

[17] CMS Collaboration, *Measurement of inclusive and differential Higgs boson production cross sections in the diphoton decay channel in proton–proton collisions at $\sqrt{s} = 13$ TeV*, JHEP **01** (2019) 183, arXiv: 1807.03825 [hep-ex].

[18] CMS Collaboration, *Measurements of Higgs boson properties in the diphoton decay channel in proton–proton collisions at* $\sqrt{s} = 13$ *TeV*, JHEP **11** (2018) 185, arXiv: 1804.02716 [hep-ex].

[19] CMS Collaboration, *Measurements of properties of the Higgs boson decaying into the four-lepton final state in pp collisions at* $\sqrt{s} = 13$ *TeV*, JHEP **11** (2017) 047, arXiv: 1706.09936 [hep-ex].

[20] CMS Collaboration, *Measurements of properties of the Higgs boson decaying to a W boson pair in pp collisions at* $\sqrt{s} = 13$ *TeV*, Phys. Lett. B **791** (2019) 96, arXiv: 1806.05246 [hep-ex].

[21] ATLAS and CMS Collaborations,
Measurements of the Higgs boson production and decay rates and constraints on its couplings from a combined ATLAS and CMS analysis of the LHC pp collision data at $\sqrt{s} = 7$ *and* 8 *TeV*, JHEP **08** (2016) 045, arXiv: 1606.02266 [hep-ex].

[22] ATLAS Collaboration, *Cross-section measurements of the Higgs boson decaying into a pair of* τ*-leptons in proton–proton collisions at* $\sqrt{s} = 13$ *TeV with the ATLAS detector*,
Phys. Rev. D **99** (2019) 072001, arXiv: 1811.08856 [hep-ex].

[23] CMS Collaboration,
Observation of the Higgs boson decay to a pair of τ *leptons with the CMS detector*,
Phys. Lett. B **779** (2018) 283, arXiv: 1708.00373 [hep-ex].

[24] ATLAS Collaboration, *Observation of Higgs boson production in association with a top quark pair at the LHC with the ATLAS detector*, Phys. Lett. B **784** (2018) 173,
arXiv: 1806.00425 [hep-ex].

[25] CMS Collaboration, *Observation of* $t\bar{t}H$ *Production*, Phys. Rev. Lett. **120** (2018) 231801,
arXiv: 1804.02610 [hep-ex].

[26] A. Djouadi, J. Kalinowski and M. Spira, *HDECAY: A program for Higgs boson decays in the Standard Model and its supersymmetric extension*, Comput. Phys. Commun. **108** (1998) 56,
arXiv: hep-ph/9704448.

[27] D. de Florian et al.,
Handbook of LHC Higgs Cross Sections: 4. Deciphering the Nature of the Higgs Sector, (2016),
arXiv: 1610.07922 [hep-ph].

[28] ATLAS Collaboration,
Evidence for the Higgs-boson Yukawa coupling to tau leptons with the ATLAS detector,
JHEP **04** (2015) 117, arXiv: 1501.04943 [hep-ex].

[29] CMS Collaboration, *Evidence for the* 125 *GeV Higgs boson decaying to a pair of* τ *leptons*,
JHEP **05** (2014) 104, arXiv: 1401.5041 [hep-ex].

[30] ATLAS Collaboration, *Test of CP invariance in vector-boson fusion production of the Higgs boson in the* $H \to \tau\tau$ *channel in proton–proton collisions at* $\sqrt{s} = 13$ *TeV with the ATLAS detector*,
Phys. Lett. B **805** (2020) 135426, arXiv: 2002.05315 [hep-ex].

[31] CMS Collaboration, *Search for the associated production of the Higgs boson and a vector boson in proton–proton collisions at* $\sqrt{s} = 13$ *TeV via Higgs boson decays to* τ *leptons*, JHEP **06** (2019) 093,
arXiv: 1809.03590 [hep-ex].

[32] CMS Collaboration, *Measurement of the inclusive and differential Higgs boson production cross sections in the decay mode to a pair of* τ *leptons in pp collisions at* $\sqrt{s} = 13$ *TeV*, (2021),
arXiv: 2107.11486 [hep-ex].

[33] N. Berger et al., *Simplified Template Cross Sections - Stage 1.1*, 2019, arXiv: 1906.02754 [hep-ph].

[34] ATLAS Collaboration, *Search for the associated production of the Higgs boson with a top quark pair in multilepton final states with the ATLAS detector*, Phys. Lett. B **749** (2015) 519, arXiv: 1506.05988 [hep-ex].

[35] ATLAS Collaboration, *Search for the standard model Higgs boson produced in association with a vector boson and decaying into a tau pair in pp collisions at $\sqrt{s} = 8$ TeV with the ATLAS detector*, Phys. Rev. D **93** (2016) 092005, arXiv: 1511.08352 [hep-ex].

[36] ATLAS Collaboration, *Modelling $Z \to \tau\tau$ processes in ATLAS with τ-embedded $Z \to \mu\mu$ data*, JINST **10** (2015) P09018, arXiv: 1506.05623 [hep-ex].

[37] CMS Collaboration, *An embedding technique to determine $\tau\tau$ backgrounds in proton–proton collision data*, JINST **14** (2019) P06032, arXiv: 1903.01216 [hep-ex].

[38] ATLAS Collaboration, *The ATLAS Experiment at the CERN Large Hadron Collider*, JINST **3** (2008) S08003.

[39] ATLAS Collaboration, *ATLAS Insertable B-Layer: Technical Design Report*, ATLAS-TDR-19; CERN-LHCC-2010-013, 2010, URL: https://cds.cern.ch/record/1291633, Addendum: ATLAS-TDR-19-ADD-1; CERN-LHCC-2012-009, 2012, URL: https://cds.cern.ch/record/1451888.

[40] B. Abbott et al., *Production and integration of the ATLAS Insertable B-Layer*, JINST **13** (2018) T05008, arXiv: 1803.00844 [physics.ins-det].

[41] ATLAS Collaboration, *Performance of the ATLAS trigger system in 2015*, Eur. Phys. J. C **77** (2017) 317, arXiv: 1611.09661 [hep-ex].

[42] ATLAS Collaboration, *The ATLAS Collaboration Software and Firmware*, ATL-SOFT-PUB-2021-001, 2021, URL: https://cds.cern.ch/record/2767187.

[43] ATLAS Collaboration, *Performance of electron and photon triggers in ATLAS during LHC Run 2*, Eur. Phys. J. C **80** (2020) 47, arXiv: 1909.00761 [hep-ex].

[44] ATLAS Collaboration, *Performance of the ATLAS muon triggers in Run 2*, JINST **15** (2020) P09015, arXiv: 2004.13447 [hep-ex].

[45] ATLAS Collaboration, *The ATLAS Inner Detector Trigger performance in pp collisions at 13 TeV during LHC Run 2*, (2021), arXiv: 2107.02485 [hep-ex].

[46] ATLAS Collaboration, *Performance of the ATLAS Level-1 topological trigger in Run 2*, (2021), arXiv: 2105.01416 [hep-ex].

[47] ATLAS Collaboration, *ATLAS data quality operations and performance for 2015–2018 data-taking*, JINST **15** (2020) P04003, arXiv: 1911.04632 [physics.ins-det].

[48] ATLAS Collaboration, *The ATLAS Simulation Infrastructure*, Eur. Phys. J. C **70** (2010) 823, arXiv: 1005.4568 [physics.ins-det].

[49] S. Agostinelli et al., *GEANT4: a simulation toolkit*, Nucl. Instrum. Meth. A **506** (2003) 250.

[50] T. Sjöstrand, S. Mrenna and P. Z. Skands, *A brief introduction to PYTHIA 8.1*, Comput. Phys. Commun. **178** (2008) 852, arXiv: 0710.3820 [hep-ph].

[51] ATLAS Collaboration, *The Pythia 8 A3 tune description of ATLAS minimum bias and inelastic measurements incorporating the Donnachie–Landshoff diffractive model*, ATL-PHYS-PUB-2016-017, 2016, URL: https://cds.cern.ch/record/2206965.

[52] R. D. Ball et al., *Parton distributions with LHC data*, Nucl. Phys. B **867** (2013) 244, arXiv: 1207.1303 [hep-ph].

[53] P. Ilten, *Tau Decays in Pythia 8*, Nucl. Phys. Proc. Suppl. **253-255** (2014) 77, The Twelfth International Workshop on Tau-Lepton Physics (TAU2012).

[54] P. Golonka et al., *The tauola-photos-F environment for the TAUOLA and PHOTOS packages, release II*, Comput. Phys. Commun. **174** (2006) 818.

[55] S. Frixione, P. Nason and G. Ridolfi, *A positive-weight next-to-leading-order Monte Carlo for heavy flavour hadroproduction*, JHEP **09** (2007) 126, arXiv: 0707.3088 [hep-ph].

[56] P. Nason, *A new method for combining NLO QCD with shower Monte Carlo algorithms*, JHEP **11** (2004) 040, arXiv: hep-ph/0409146.

[57] S. Frixione, P. Nason and C. Oleari, *Matching NLO QCD computations with parton shower simulations: the POWHEG method*, JHEP **11** (2007) 070, arXiv: 0709.2092 [hep-ph].

[58] S. Alioli, P. Nason, C. Oleari and E. Re, *A general framework for implementing NLO calculations in shower Monte Carlo programs: the POWHEG BOX*, JHEP **06** (2010) 043, arXiv: 1002.2581 [hep-ph].

[59] H. B. Hartanto, B. Jäger, L. Reina and D. Wackeroth, *Higgs boson production in association with top quarks in the POWHEG BOX*, Phys. Rev. D **91** (2015) 094003, arXiv: 1501.04498 [hep-ph].

[60] J. Alwall et al., *The automated computation of tree-level and next-to-leading order differential cross sections, and their matching to parton shower simulations*, JHEP **07** (2014) 079, arXiv: 1405.0301 [hep-ph].

[61] J. Butterworth et al., *PDF4LHC recommendations for LHC Run II*, J. Phys. G **43** (2016) 023001, arXiv: 1510.03865 [hep-ph].

[62] R. D. Ball et al., *Parton distributions for the LHC run II*, JHEP **04** (2015) 040, arXiv: 1410.8849 [hep-ph].

[63] H.-L. Lai et al., *New parton distributions for collider physics*, Phys. Rev. D **82** (2010) 074024, arXiv: 1007.2241 [hep-ph].

[64] T. Sjöstrand et al., *An introduction to PYTHIA 8.2*, Comput. Phys. Commun. **191** (2015) 159, arXiv: 1410.3012 [hep-ph].

[65] ATLAS Collaboration, *Measurement of the Z/γ^* boson transverse momentum distribution in pp collisions at $\sqrt{s} = 7$ TeV with the ATLAS detector*, JHEP **09** (2014) 145, arXiv: 1406.3660 [hep-ex].

[66] ATLAS Collaboration, *ATLAS Pythia 8 tunes to 7 TeV data*, ATL-PHYS-PUB-2014-021, 2014, URL: https://cds.cern.ch/record/1966419.

[67] K. Hamilton, P. Nason and G. Zanderighi, *MINLO: multi-scale improved NLO*, JHEP **10** (2012) 155, arXiv: 1206.3572 [hep-ph].

[68] J. M. Campbell et al., *NLO Higgs boson production plus one and two jets using the POWHEG BOX, MadGraph4 and MCFM*, JHEP **07** (2012) 092, arXiv: 1202.5475 [hep-ph].

[69] K. Hamilton, P. Nason, C. Oleari and G. Zanderighi, *Merging H/W/Z + 0 and 1 jet at NLO with no merging scale: a path to parton shower + NNLO matching*, JHEP **05** (2013) 082, arXiv: 1212.4504 [hep-ph].

[70] S. Catani and M. Grazzini, *Next-to-Next-to-Leading-Order Subtraction Formalism in Hadron Collisions and its Application to Higgs-boson Production at the Large Hadron Collider*, Phys. Rev. Lett. **98** (2007) 222002, arXiv: hep-ph/0703012 [hep-ph].

[71] C. Anastasiou et al., *High precision determination of the gluon fusion Higgs boson cross-section at the LHC*, JHEP **05** (2016) 058, arXiv: 1602.00695 [hep-ph].

[72] C. Anastasiou, C. Duhr, F. Dulat, F. Herzog and B. Mistlberger, *Higgs Boson Gluon-Fusion Production in QCD at Three Loops*, Phys. Rev. Lett. **114** (2015) 212001, arXiv: 1503.06056 [hep-ph].

[73] F. Dulat, A. Lazopoulos and B. Mistlberger, *iHixs 2 – Inclusive Higgs cross sections*, Comput. Phys. Commun. **233** (2018) 243, arXiv: 1802.00827 [hep-ph].

[74] R. V. Harlander and K. J. Ozeren, *Finite top mass effects for hadronic Higgs production at next-to-next-to-leading order*, JHEP **11** (2009) 088, arXiv: 0909.3420 [hep-ph].

[75] R. V. Harlander and K. J. Ozeren, *Top mass effects in Higgs production at next-to-next-to-leading order QCD: Virtual corrections*, Phys. Lett. B **679** (2009) 467, arXiv: 0907.2997 [hep-ph].

[76] R. V. Harlander, H. Mantler, S. Marzani and K. J. Ozeren, *Higgs production in gluon fusion at next-to-next-to-leading order QCD for finite top mass*, Eur. Phys. J. C **66** (2010) 359, arXiv: 0912.2104 [hep-ph].

[77] A. Pak, M. Rogal and M. Steinhauser, *Finite top quark mass effects in NNLO Higgs boson production at LHC*, JHEP **02** (2010) 025, arXiv: 0911.4662 [hep-ph].

[78] S. Actis, G. Passarino, C. Sturm and S. Uccirati, *NLO electroweak corrections to Higgs boson production at hadron colliders*, Phys. Lett. B **670** (2008) 12, arXiv: 0809.1301 [hep-ph].

[79] S. Actis, G. Passarino, C. Sturm and S. Uccirati, *NNLO computational techniques: The cases $H \to \gamma\gamma$ and $H \to gg$*, Nucl. Phys. B **811** (2009) 182, arXiv: 0809.3667 [hep-ph].

[80] M. Bonetti, K. Melnikov and L. Tancredi, *Higher order corrections to mixed QCD-EW contributions to Higgs boson production in gluon fusion*, Phys. Rev. D **97** (2018) 056017, arXiv: 1801.10403 [hep-ph], Erratum: Phys. Rev. D **97** (2018) 099906.

[81] M. Ciccolini, A. Denner and S. Dittmaier, *Strong and Electroweak Corrections to the Production of a Higgs Boson + 2 Jets via Weak Interactions at the Large Hadron Collider*, Phys. Rev. Lett. **99** (2007) 161803, arXiv: 0707.0381 [hep-ph].

[82] M. Ciccolini, A. Denner and S. Dittmaier, *Electroweak and QCD corrections to Higgs production via vector-boson fusion at the CERN LHC*, Phys. Rev. D **77** (2008) 013002, arXiv: 0710.4749 [hep-ph].

[83] P. Bolzoni, F. Maltoni, S.-O. Moch and M. Zaro,
Higgs Boson Production via Vector-Boson Fusion at Next-to-Next-to-Leading Order in QCD,
Phys. Rev. Lett. **105** (2010) 011801, arXiv: 1003.4451 [hep-ph].

[84] M. L. Ciccolini, S. Dittmaier and M. Krämer,
Electroweak radiative corrections to associated WH and ZH production at hadron colliders,
Phys. Rev. D **68** (2003) 073003, arXiv: hep-ph/0306234 [hep-ph].

[85] O. Brein, A. Djouadi and R. Harlander,
NNLO QCD corrections to the Higgs-strahlung processes at hadron colliders,
Phys. Lett. B **579** (2004) 149, arXiv: hep-ph/0307206.

[86] O. Brein, R. Harlander, M. Wiesemann and T. Zirke,
Top-quark mediated effects in hadronic Higgs-Strahlung, Eur. Phys. J. C **72** (2012) 1868,
arXiv: 1111.0761 [hep-ph].

[87] L. Altenkamp, S. Dittmaier, R. V. Harlander, H. Rzehak and T. J. E. Zirke,
Gluon-induced Higgs-strahlung at next-to-leading order QCD, JHEP **02** (2013) 078,
arXiv: 1211.5015 [hep-ph].

[88] A. Denner, S. Dittmaier, S. Kallweit and A. Mück, *HAWK 2.0: A Monte Carlo program for Higgs production in vector-boson fusion and Higgs strahlung at hadron colliders*,
Comput. Phys. Commun. **195** (2015) 161, arXiv: 1412.5390 [hep-ph].

[89] O. Brein, R. V. Harlander and T. J. E. Zirke, *vh@nnlo – Higgs Strahlung at hadron colliders*,
Comput. Phys. Commun. **184** (2013) 998, arXiv: 1210.5347 [hep-ph].

[90] R. V. Harlander, A. Kulesza, V. Theeuwes and T. Zirke,
Soft gluon resummation for gluon-induced Higgs Strahlung, JHEP **11** (2014) 082,
arXiv: 1410.0217 [hep-ph].

[91] D. J. Lange, *The EvtGen particle decay simulation package*,
Nucl. Instrum. Meth. A **462** (2001) 152.

[92] W. Beenakker, S. Dittmaier, M. Krämer, B. Plumper, M. Spira et al.,
NLO QCD corrections to $t\bar{t}H$ production in hadron collisions, Nucl. Phys. B **653** (2003) 151,
arXiv: hep-ph/0211352 [hep-ph].

[93] S. Dawson, C. Jackson, L. Orr, L. Reina and D. Wackeroth, *Associated Higgs boson production with top quarks at the CERN Large Hadron Collider: NLO QCD corrections*,
Phys. Rev. D **68** (2003) 034022, arXiv: hep-ph/0305087 [hep-ph].

[94] Y. Zhang, W.-G. Ma, R.-Y. Zhang, C. Chen and L. Guo,
QCD NLO and EW NLO corrections to $t\bar{t}H$ production with top quark decays at hadron collider,
Phys. Lett. B **738** (2014) 1, arXiv: 1407.1110 [hep-ph].

[95] S. Frixione, V. Hirschi, D. Pagani, H. S. Shao and M. Zaro,
Weak corrections to Higgs hadroproduction in association with a top-quark pair,
JHEP **09** (2014) 065, arXiv: 1407.0823 [hep-ph].

[96] B. Jager, L. Reina and D. Wackeroth,
Higgs boson production in association with b jets in the POWHEG BOX,
Phys. Rev. D **93** (2016) 014030, arXiv: 1509.05843 [hep-ph].

[97] F. Demartin, F. Maltoni, K. Mawatari and M. Zaro,
Higgs production in association with a single top quark at the LHC, Eur. Phys. J. C **75** (2015) 267,
arXiv: 1504.00611 [hep-ph].

[98] F. Demartin, B. Maier, F. Maltoni, K. Mawatari and M. Zaro,
tWH associated production at the LHC, Eur. Phys. J. C **77** (2017) 34,
arXiv: 1607.05862 [hep-ph].

[99] M. Spira, *QCD Effects in Higgs physics*, Fortsch. Phys. **46** (1998) 203, arXiv: hep-ph/9705337.

[100] A. Djouadi, M. M. Mühlleitner and M. Spira,
Decays of Supersymmetric particles: The Program SUSY-HIT (SUspect-SdecaY-Hdecay-InTerface),
Acta Phys. Polon. B **38** (2007) 635, arXiv: hep-ph/0609292.

[101] A. Bredenstein, A. Denner, S. Dittmaier and M. M. Weber, *Radiative corrections to the semileptonic and hadronic Higgs-boson decays $H \to WW/ZZ \to 4$ fermions*,
JHEP **02** (2007) 080, arXiv: hep-ph/0611234.

[102] A. Bredenstein, A. Denner, S. Dittmaier and M. M. Weber,
Precise predictions for the Higgs-boson decay $H \to WW/ZZ \to 4$ leptons,
Phys. Rev. D **74** (2006) 013004, arXiv: hep-ph/0604011 [hep-ph].

[103] A. Bredenstein, A. Denner, S. Dittmaier and M. M. Weber,
Precision calculations for the Higgs decay $H \to ZZ/WW \to 4$ leptons,
Nucl. Phys. Proc. Suppl. **160** (2006) 131, arXiv: hep-ph/0607060 [hep-ph].

[104] E. Bothmann et al., *Event generation with Sherpa 2.2*, SciPost Phys. **7** (2019) 034,
arXiv: 1905.09127 [hep-ph].

[105] T. Gleisberg and S. Höche, *Comix, a new matrix element generator*, JHEP **12** (2008) 039,
arXiv: 0808.3674 [hep-ph].

[106] F. Buccioni et al., *OpenLoops 2*, Eur. Phys. J. C **79** (2019) 866, arXiv: 1907.13071 [hep-ph].

[107] F. Cascioli, P. Maierhöfer and S. Pozzorini, *Scattering Amplitudes with Open Loops*,
Phys. Rev. Lett. **108** (2012) 111601, arXiv: 1111.5206 [hep-ph].

[108] A. Denner, S. Dittmaier and L. Hofer,
Collier: A fortran-based complex one-loop library in extended regularizations,
Comput. Phys. Commun. **212** (2017) 220, arXiv: 1604.06792 [hep-ph].

[109] S. Schumann and F. Krauss,
A parton shower algorithm based on Catani–Seymour dipole factorisation, JHEP **03** (2008) 038,
arXiv: 0709.1027 [hep-ph].

[110] S. Höche, F. Krauss, M. Schönherr and F. Siegert,
A critical appraisal of NLO+PS matching methods, JHEP **09** (2012) 049,
arXiv: 1111.1220 [hep-ph].

[111] S. Höche, F. Krauss, M. Schönherr and F. Siegert,
QCD matrix elements + parton showers. The NLO case, JHEP **04** (2013) 027,
arXiv: 1207.5030 [hep-ph].

[112] S. Catani, F. Krauss, B. R. Webber and R. Kuhn, *QCD Matrix Elements + Parton Showers*,
JHEP **11** (2001) 063, arXiv: hep-ph/0109231.

[113] S. Höche, F. Krauss, S. Schumann and F. Siegert, *QCD matrix elements and truncated showers*,
JHEP **05** (2009) 053, arXiv: 0903.1219 [hep-ph].

[114] C. Anastasiou, L. J. Dixon, K. Melnikov and F. Petriello, *High precision QCD at hadron colliders: Electroweak gauge boson rapidity distributions at next-to-next-to leading order*,
Phys. Rev. D **69** (2004) 094008, arXiv: hep-ph/0312266.

[115] ATLAS Collaboration, *Studies on top-quark Monte Carlo modelling for Top2016*, ATL-PHYS-PUB-2016-020, 2016, URL: https://cds.cern.ch/record/2216168.

[116] M. Beneke, P. Falgari, S. Klein and C. Schwinn, *Hadronic top-quark pair production with NNLL threshold resummation*, Nucl. Phys. B **855** (2012) 695, arXiv: 1109.1536 [hep-ph].

[117] M. Cacciari, M. Czakon, M. Mangano, A. Mitov and P. Nason, *Top-pair production at hadron colliders with next-to-next-to-leading logarithmic soft-gluon resummation*, Phys. Lett. B **710** (2012) 612, arXiv: 1111.5869 [hep-ph].

[118] P. Bärnreuther, M. Czakon and A. Mitov, *Percent-Level-Precision Physics at the Tevatron: Next-to-Next-to-Leading Order QCD Corrections to $q\bar{q} \to t\bar{t} + X$*, Phys. Rev. Lett. **109** (2012) 132001, arXiv: 1204.5201 [hep-ph].

[119] M. Czakon and A. Mitov, *NNLO corrections to top-pair production at hadron colliders: the all-fermionic scattering channels*, JHEP **12** (2012) 054, arXiv: 1207.0236 [hep-ph].

[120] M. Czakon and A. Mitov, *NNLO corrections to top pair production at hadron colliders: the quark-gluon reaction*, JHEP **01** (2013) 080, arXiv: 1210.6832 [hep-ph].

[121] M. Czakon, P. Fiedler and A. Mitov, *Total Top-Quark Pair-Production Cross Section at Hadron Colliders Through $O(\alpha_S^4)$*, Phys. Rev. Lett. **110** (2013) 252004, arXiv: 1303.6254 [hep-ph].

[122] M. Czakon and A. Mitov, *Top++: A program for the calculation of the top-pair cross-section at hadron colliders*, Comput. Phys. Commun. **185** (2014) 2930, arXiv: 1112.5675 [hep-ph].

[123] M. Aliev et al., *HATHOR – HAdronic Top and Heavy quarks crOss section calculatoR*, Comput. Phys. Commun. **182** (2011) 1034, arXiv: 1007.1327 [hep-ph].

[124] P. Kant et al., *HatHor for single top-quark production: Updated predictions and uncertainty estimates for single top-quark production in hadronic collisions*, Comput. Phys. Commun. **191** (2015) 74, arXiv: 1406.4403 [hep-ph].

[125] F. Cascioli et al., *Precise Higgs-background predictions: Merging NLO QCD and squared quark-loop corrections to four-lepton + 0,1 jet production*, JHEP **046** (2014).

[126] ATLAS Collaboration, *Reconstruction of primary vertices at the ATLAS experiment in Run 1 proton–proton collisions at the LHC*, Eur. Phys. J. C **77** (2017) 332, arXiv: 1611.10235 [hep-ex].

[127] ATLAS Collaboration, *Electron and photon performance measurements with the ATLAS detector using the 2015–2017 LHC proton–proton collision data*, JINST **14** (2019) P12006, arXiv: 1908.00005 [hep-ex].

[128] ATLAS Collaboration, *2015 start-up trigger menu and initial performance assessment of the ATLAS trigger using Run-2 data*, ATL-DAQ-PUB-2016-001, 2016, URL: https://cds.cern.ch/record/2136007.

[129] ATLAS Collaboration, *Trigger Menu in 2016*, ATL-DAQ-PUB-2017-001, 2017, URL: https://cds.cern.ch/record/2242069.

[130] ATLAS Collaboration, *Trigger Menu in 2017*, ATL-DAQ-PUB-2018-002, 2018, URL: https://cds.cern.ch/record/2625986.

[131] ATLAS Collaboration, *Trigger Menu in 2018*, ATL-DAQ-PUB-2019-001, 2019, URL: https://cds.cern.ch/record/2693402.

[132] ATLAS Collaboration, *Muon reconstruction and identification efficiency in ATLAS using the full Run 2 pp collision data set at* $\sqrt{s}$ = 13 *TeV*, Eur. Phys. J. C **81** (2020) 578, arXiv: 2012.00578 [hep-ex].

[133] M. Cacciari, G. P. Salam and G. Soyez, *The anti-*k_t *jet clustering algorithm*, JHEP **04** (2008) 063, arXiv: 0802.1189 [hep-ph].

[134] ATLAS Collaboration, *Topological cell clustering in the ATLAS calorimeters and its performance in LHC Run 1*, Eur. Phys. J. C **77** (2017) 490, arXiv: 1603.02934 [hep-ex].

[135] ATLAS Collaboration, *Measurement of the tau lepton reconstruction and identification performance in the ATLAS experiment using pp collisions at* $\sqrt{s}$ = 13 *TeV*, ATLAS-CONF-2017-029, 2017, URL: https://cds.cern.ch/record/2261772.

[136] ATLAS Collaboration, *Reconstruction of hadronic decay products of tau leptons with the ATLAS experiment*, Eur. Phys. J. C **76** (2016) 295, arXiv: 1512.05955 [hep-ex].

[137] ATLAS Collaboration, *Identification of hadronic tau lepton decays using neural networks in the ATLAS experiment*, ATL-PHYS-PUB-2019-033, 2019, URL: https://cds.cern.ch/record/2688062.

[138] ATLAS Collaboration, *Jet reconstruction and performance using particle flow with the ATLAS Detector*, Eur. Phys. J. C **77** (2017) 466, arXiv: 1703.10485 [hep-ex].

[139] ATLAS Collaboration, *Selection of jets produced in* 13 *TeV proton–proton collisions with the ATLAS detector*, ATLAS-CONF-2015-029, 2015, URL: https://cds.cern.ch/record/2037702.

[140] ATLAS Collaboration, *Performance of pile-up mitigation techniques for jets in pp collisions at* $\sqrt{s}$ = 8 *TeV using the ATLAS detector*, Eur. Phys. J. C **76** (2016) 581, arXiv: 1510.03823 [hep-ex].

[141] ATLAS Collaboration, *Identification and rejection of pile-up jets at high pseudorapidity with the ATLAS detector*, Eur. Phys. J. C **77** (2017) 580, arXiv: 1705.02211 [hep-ex], Erratum: Eur. Phys. J. C **77** (2017) 712.

[142] ATLAS Collaboration, *ATLAS b-jet identification performance and efficiency measurement with* $t\bar{t}$ *events in pp collisions at* $\sqrt{s}$ = 13 *TeV*, Eur. Phys. J. C **79** (2019) 970, arXiv: 1907.05120 [hep-ex].

[143] ATLAS Collaboration, *Optimisation and performance studies of the ATLAS b-tagging algorithms for the 2017-18 LHC run*, ATL-PHYS-PUB-2017-013, 2017, URL: https://cds.cern.ch/record/2273281.

[144] ATLAS Collaboration, *Performance of missing transverse momentum reconstruction with the ATLAS detector using proton–proton collisions at* $\sqrt{s}$ = 13 *TeV*, Eur. Phys. J. C **78** (2018) 903, arXiv: 1802.08168 [hep-ex].

[145] A. Elagin, P. Murat, A. Pranko and A. Safonov,
A new mass reconstruction technique for resonances decaying to $\tau\tau$,
Nucl. Instrum. Meth. **A 654** (2011) 481, arXiv: 1012.4686 [hep-ex].

[146] R. Ellis, I. Hinchliffe, M. Soldate and J. van der Bij, *Higgs decay to $\tau^+\tau^-$: A possible signature of intermediate mass Higgs bosons at high energy hadron colliders*, Nucl. Phys. B **297** (1988) 221.

[147] ATLAS Collaboration,
Measurements of gluon fusion and vector-boson-fusion production of the Higgs boson in $H \to WW^* \to e\nu\mu\nu$ decays using pp collisions at $\sqrt{s} = 13$ TeV with the ATLAS detector,
ATLAS-CONF-2021-014, 2021, URL: https://cds.cern.ch/record/2759651.

[148] ATLAS Collaboration, *Formulae for Estimating Significance*, ATL-PHYS-PUB-2020-025, 2020, URL: https://cds.cern.ch/record/2736148.

[149] ATLAS Collaboration, *Measurements of the production cross section of a Z boson in association with jets in pp collisions at $\sqrt{s} = 13$ TeV with the ATLAS detector*, Eur. Phys. J. C **77** (2017) 361, arXiv: 1702.05725 [hep-ex].

[150] ATLAS Collaboration, *Measurement of the cross-section for electroweak production of dijets in association with a Z boson in pp collisions at $\sqrt{s} = 13$ TeV with the ATLAS detector*, Phys. Lett. B **775** (2017) 206, arXiv: 1709.10264 [hep-ex].

[151] ATLAS Collaboration, *Estimation of non-prompt and fake lepton backgrounds in final states with top quarks produced in proton–proton collisions at $\sqrt{s} = 8$ TeV with the ATLAS Detector*, ATLAS-CONF-2014-058, 2014, URL: https://cds.cern.ch/record/1951336.

[152] ATLAS Collaboration, *Measurements of Higgs boson production and couplings in the four-lepton channel in pp collisions at center-of-mass energies of 7 and 8 TeV with the ATLAS detector*, Phys. Rev. D **91** (2015) 012006, arXiv: 1408.5191 [hep-ex].

[153] ATLAS Collaboration, *Jet energy scale and resolution measured in proton–proton collisions at $\sqrt{s} = 13$ TeV with the ATLAS detector*, Eur. Phys. J. C **81** (2020) 689, arXiv: 2007.02645 [hep-ex].

[154] ATLAS Collaboration,
Luminosity determination in pp collisions at $\sqrt{s} = 13$ TeV using the ATLAS detector at the LHC,
ATLAS-CONF-2019-021, 2019, URL: https://cds.cern.ch/record/2677054.

[155] G. Avoni et al., *The new LUCID-2 detector for luminosity measurement and monitoring in ATLAS*, JINST **13** (2018) P07017.

[156] E. Bothmann, M. Schönherr and S. Schumann,
Reweighting QCD matrix-element and parton-shower calculations, Eur. Phys. J. C **76** (2016) 590, arXiv: 1606.08753 [hep-ph].

[157] ATLAS Collaboration,
Studies on top-quark Monte Carlo modelling with Sherpa and MG5_aMC@NLO,
ATL-PHYS-PUB-2017-007, 2017, URL: https://cds.cern.ch/record/2261938.

[158] M. Bähr et al., *Herwig++ physics and manual*, Eur. Phys. J. C **58** (2008) 639, arXiv: 0803.0883 [hep-ph].

[159] J. Bellm et al., *Herwig 7.0/Herwig++ 3.0 release note*, Eur. Phys. J. C **76** (2016) 196, arXiv: 1512.01178 [hep-ph].

[160] L. Harland-Lang, A. Martin, P. Motylinski and R. Thorne,
Parton distributions in the LHC era: MMHT 2014 PDFs, Eur. Phys. J. C **75** (2015) 204, arXiv: 1412.3989 [hep-ph].

[161] S. Dulat et al.,
New parton distribution functions from a global analysis of quantum chromodynamics, Phys. Rev. D **93** (2016) 033006, arXiv: 1506.07443 [hep-ph].

[162] J. Bendavid et al.,
Les Houches 2017: Physics at TeV Colliders Standard Model Working Group Report, 2018, arXiv: 1803.07977 [hep-ph].

[163] I. W. Stewart and F. J. Tackmann,
Theory uncertainties for Higgs mass and other searches using jet bins, Phys. Rev. D **85** (2012) 034011, arXiv: 1107.2117 [hep-ph].

[164] S. Gangal and F. J. Tackmann,
Next-to-leading-order uncertainties in Higgs+2 jets from gluon fusion, Phys. Rev. D **87** (2013) 093008, arXiv: 1302.5437 [hep-ph].

[165] R. Frederix and S. Frixione, *Merging meets matching in MC@NLO*, JHEP **12** (2012) 061, arXiv: 1209.6215 [hep-ph].

[166] G. Cowan, K. Cranmer, E. Gross and O. Vitells,
Asymptotic formulae for likelihood-based tests of new physics, Eur. Phys. J. C **71** (2011) 1554, arXiv: 1007.1727 [physics.data-an], Erratum: Eur. Phys. J. C **73** (2013) 2501.

[167] ATLAS Collaboration, *Measurements of Higgs boson production cross-sections in the $H \to \tau^+\tau^-$ decay channel in pp collisions at $\sqrt{s} = 13$ TeV with the ATLAS detector*, HEPData, 2022, URL: https://www.hepdata.net/record/115994.

[168] ATLAS Collaboration, *ATLAS Computing Acknowledgements*, ATL-SOFT-PUB-2021-003, URL: https://cds.cern.ch/record/2776662.

The ATLAS Collaboration

G. Aad[98], B. Abbott[124], D.C. Abbott[99], A. Abed Abud[34], K. Abeling[51], D.K. Abhayasinghe[91], S.H. Abidi[27], A. Aboulhorma[33e], H. Abramowicz[157], H. Abreu[156], Y. Abulaiti[5], A.C. Abusleme Hoffman[142a], B.S. Acharya[64a,64b,o], B. Achkar[51], L. Adam[96], C. Adam Bourdarios[4], L. Adamczyk[81a], L. Adamek[162], S.V. Addepalli[24], J. Adelman[116], A. Adiguzel[11c,ac], S. Adorni[52], T. Adye[139], A.A. Affolder[141], Y. Afik[34], C. Agapopoulou[62], M.N. Agaras[12], J. Agarwala[68a,68b], A. Aggarwal[114], C. Agheorghiesei[25c], J.A. Aguilar-Saavedra[135f,135a,ab], A. Ahmad[34], F. Ahmadov[77], W.S. Ahmed[100], X. Ai[44], G. Aielli[71a,71b], I. Aizenberg[175], S. Akatsuka[83], M. Akbiyik[96], T.P.A. Åkesson[94], A.V. Akimov[107], K. Al Khoury[37], G.L. Alberghi[21b], J. Albert[171], P. Albicocco[49], M.J. Alconada Verzini[86], S. Alderweireldt[48], M. Aleksa[34], I.N. Aleksandrov[77], C. Alexa[25b], T. Alexopoulos[9], A. Alfonsi[115], F. Alfonsi[21b], M. Alhroob[124], B. Ali[137], S. Ali[154], M. Aliev[161], G. Alimonti[66a], C. Allaire[34], B.M.M. Allbrooke[152], P.P. Allport[19], A. Aloisio[67a,67b], F. Alonso[86], C. Alpigiani[144], E. Alunno Camelia[71a,71b], M. Alvarez Estevez[95], M.G. Alviggi[67a,67b], Y. Amaral Coutinho[78b], A. Ambler[100], L. Ambroz[130], C. Amelung[34], D. Amidei[102], S.P. Amor Dos Santos[135a], S. Amoroso[44], K.R. Amos[169], C.S. Amrouche[52], V. Ananiev[129], C. Anastopoulos[145], N. Andari[140], T. Andeen[10], J.K. Anders[18], S.Y. Andrean[43a,43b], A. Andreazza[66a,66b], S. Angelidakis[8], A. Angerami[37], A.V. Anisenkov[117b,117a], A. Annovi[69a], C. Antel[52], M.T. Anthony[145], E. Antipov[125], M. Antonelli[49], D.J.A. Antrim[16], F. Anulli[70a], M. Aoki[79], J.A. Aparisi Pozo[169], M.A. Aparo[152], L. Aperio Bella[44], N. Aranzabal[34], V. Araujo Ferraz[78a], C. Arcangeletti[49], A.T.H. Arce[47], E. Arena[88], J-F. Arguin[106], S. Argyropoulos[50], J.-H. Arling[44], A.J. Armbruster[34], A. Armstrong[166], O. Arnaez[162], H. Arnold[34], Z.P. Arrubarrena Tame[110], G. Artoni[130], H. Asada[112], K. Asai[122], S. Asai[159], N.A. Asbah[57], E.M. Asimakopoulou[167], L. Asquith[152], J. Assahsah[33d], K. Assamagan[27], R. Astalos[26a], R.J. Atkin[31a], M. Atkinson[168], N.B. Atlay[17], H. Atmani[58b], P.A. Atmasiddha[102], K. Augsten[137], S. Auricchio[67a,67b], V.A. Austrup[177], G. Avner[156], G. Avolio[34], M.K. Ayoub[13c], G. Azuelos[106,aj], D. Babal[26a], H. Bachacou[140], K. Bachas[158], A. Bachiu[32], F. Backman[43a,43b], A. Badea[57], P. Bagnaia[70a,70b], H. Bahrasemani[148], A.J. Bailey[169], V.R. Bailey[168], J.T. Baines[139], C. Bakalis[9], O.K. Baker[178], P.J. Bakker[115], E. Bakos[14], D. Bakshi Gupta[7], S. Balaji[153], R. Balasubramanian[115], E.M. Baldin[117b,117a], P. Balek[138], E. Ballabene[66a,66b], F. Balli[140], L.M. Baltes[59a], W.K. Balunas[130], J. Balz[96], E. Banas[82], M. Bandieramonte[134], A. Bandyopadhyay[22], S. Bansal[22], L. Barak[157], E.L. Barberio[101], D. Barberis[53b,53a], M. Barbero[98], G. Barbour[92], K.N. Barends[31a], T. Barillari[111], M-S. Barisits[34], J. Barkeloo[127], T. Barklow[149], B.M. Barnett[139], R.M. Barnett[16], A. Baroncelli[58a], G. Barone[27], A.J. Barr[130], L. Barranco Navarro[43a,43b], F. Barreiro[95], J. Barreiro Guimarães da Costa[13a], U. Barron[157], S. Barsov[133], F. Bartels[59a], R. Bartoldus[149], G. Bartolini[98], A.E. Barton[87], P. Bartos[26a], A. Basalaev[44], A. Basan[96], M. Baselga[44], I. Bashta[72a,72b], A. Bassalat[62,ag], M.J. Basso[162], C.R. Basson[97], R.L. Bates[55], S. Batlamous[33e], J.R. Batley[30], B. Batool[147], M. Battaglia[141], M. Bauce[70a,70b], F. Bauer[140,*], P. Bauer[22], H.S. Bawa[29], A. Bayirli[11c], J.B. Beacham[47], T. Beau[131], P.H. Beauchemin[165], F. Becherer[50], P. Bechtle[22], H.P. Beck[18,q], K. Becker[173], C. Becot[44], A.J. Beddall[11a], V.A. Bednyakov[77], C.P. Bee[151], T.A. Beermann[34], M. Begalli[78b], M. Begel[27], A. Behera[151], J.K. Behr[44], C. Beirao Da Cruz E Silva[34], J.F. Beirer[51,34], F. Beisiegel[22], M. Belfkir[4], G. Bella[157], L. Bellagamba[21b], A. Bellerive[32], P. Bellos[19], K. Beloborodov[117b,117a], K. Belotskiy[108], N.L. Belyaev[108], D. Benchekroun[33a], Y. Benhammou[157], D.P. Benjamin[27], M. Benoit[27], J.R. Bensinger[24], S. Bentvelsen[115], L. Beresford[34], M. Beretta[49], D. Berge[17], E. Bergeaas Kuutmann[167], N. Berger[4], B. Bergmann[137], L.J. Bergsten[24], J. Beringer[16], S. Berlendis[6], G. Bernardi[131], C. Bernius[149], F.U. Bernlochner[22], T. Berry[91], P. Berta[138], A. Berthold[46], I.A. Bertram[87], O. Bessidskaia Bylund[177], S. Bethke[111], A. Betti[40], A.J. Bevan[90], S. Bhatta[151], D.S. Bhattacharya[172], P. Bhattarai[24], V.S. Bhopatkar[5], R. Bi[134], R.M. Bianchi[134], O. Biebel[110],

R. Bielski[127], N.V. Biesuz[69a,69b], M. Biglietti[72a], T.R.V. Billoud[137], M. Bindi[51], A. Bingul[11d], C. Bini[70a,70b], S. Biondi[21b,21a], A. Biondini[88], C.J. Birch-sykes[97], G.A. Bird[19,139], M. Birman[175], T. Bisanz[34], J.P. Biswal[2], D. Biswas[176,j], A. Bitadze[97], C. Bittrich[46], K. Bjørke[129], I. Bloch[44], C. Blocker[24], A. Blue[55], U. Blumenschein[90], J. Blumenthal[96], G.J. Bobbink[115], V.S. Bobrovnikov[117b,117a], M. Boehler[50], D. Bogavac[12], A.G. Bogdanchikov[117b,117a], C. Bohm[43a], V. Boisvert[91], P. Bokan[44], T. Bold[81a], M. Bomben[131], M. Bona[90], M. Boonekamp[140], C.D. Booth[91], A.G. Borbély[55], H.M. Borecka-Bielska[106], L.S. Borgna[92], G. Borissov[87], D. Bortoletto[130], D. Boscherini[21b], M. Bosman[12], J.D. Bossio Sola[34], K. Bouaouda[33a], J. Boudreau[134], E.V. Bouhova-Thacker[87], D. Boumediene[36], R. Bouquet[131], A. Boveia[123], J. Boyd[34], D. Boye[27], I.R. Boyko[77], A.J. Bozson[91], J. Bracinik[19], N. Brahimi[58d,58c], G. Brandt[177], O. Brandt[30], F. Braren[44], B. Brau[99], J.E. Brau[127], W.D. Breaden Madden[55], K. Brendlinger[44], R. Brener[175], L. Brenner[34], R. Brenner[167], S. Bressler[175], B. Brickwedde[96], D.L. Briglin[19], D. Britton[55], D. Britzger[111], I. Brock[22], R. Brock[103], G. Brooijmans[37], W.K. Brooks[142e], E. Brost[27], P.A. Bruckman de Renstrom[82], B. Brüers[44], D. Bruncko[26b], A. Bruni[21b], G. Bruni[21b], M. Bruschi[21b], N. Bruscino[70a,70b], L. Bryngemark[149], T. Buanes[15], Q. Buat[151], P. Buchholz[147], A.G. Buckley[55], I.A. Budagov[77], M.K. Bugge[129], O. Bulekov[108], B.A. Bullard[57], S. Burdin[88], C.D. Burgard[44], A.M. Burger[125], B. Burghgrave[7], J.T.P. Burr[44], C.D. Burton[10], J.C. Burzynski[148], E.L. Busch[37], V. Büscher[96], P.J. Bussey[55], J.M. Butler[23], C.M. Buttar[55], J.M. Butterworth[92], W. Buttinger[139], C.J. Buxo Vazquez[103], A.R. Buzykaev[117b,117a], G. Cabras[21b], S. Cabrera Urbán[169], D. Caforio[54], H. Cai[134], V.M.M. Cairo[149], O. Cakir[3a], N. Calace[34], P. Calafiura[16], G. Calderini[131], P. Calfayan[63], G. Callea[55], L.P. Caloba[78b], D. Calvet[36], S. Calvet[36], T.P. Calvet[98], M. Calvetti[69a,69b], R. Camacho Toro[131], S. Camarda[34], D. Camarero Munoz[95], P. Camarri[71a,71b], M.T. Camerlingo[72a,72b], D. Cameron[129], C. Camincher[171], M. Campanelli[92], A. Camplani[38], V. Canale[67a,67b], A. Canesse[100], M. Cano Bret[75], J. Cantero[125], Y. Cao[168], F. Capocasa[24], M. Capua[39b,39a], A. Carbone[66a,66b], R. Cardarelli[71a], J.C.J. Cardenas[7], F. Cardillo[169], G. Carducci[39b,39a], T. Carli[34], G. Carlino[67a], B.T. Carlson[134], E.M. Carlson[171,163a], L. Carminati[66a,66b], M. Carnesale[70a,70b], R.M.D. Carney[149], S. Caron[114], E. Carquin[142e], S. Carrá[44], G. Carratta[21b,21a], J.W.S. Carter[162], T.M. Carter[48], D. Casadei[31c], M.P. Casado[12,g], A.F. Casha[162], E.G. Castiglia[178], F.L. Castillo[59a], L. Castillo Garcia[12], V. Castillo Gimenez[169], N.F. Castro[135a,135e], A. Catinaccio[34], J.R. Catmore[129], A. Cattai[34], V. Cavaliere[27], N. Cavalli[21b,21a], V. Cavasinni[69a,69b], E. Celebi[11b], F. Celli[130], M.S. Centonze[65a,65b], K. Cerny[126], A.S. Cerqueira[78a], A. Cerri[152], L. Cerrito[71a,71b], F. Cerutti[16], A. Cervelli[21b], S.A. Cetin[11b], Z. Chadi[33a], D. Chakraborty[116], M. Chala[135f], J. Chan[176], W.S. Chan[115], W.Y. Chan[88], J.D. Chapman[30], B. Chargeishvili[155b], D.G. Charlton[19], T.P. Charman[90], M. Chatterjee[18], S. Chekanov[5], S.V. Chekulaev[163a], G.A. Chelkov[77,ae], A. Chen[102], B. Chen[157], B. Chen[171], C. Chen[58a], C.H. Chen[76], H. Chen[13c], H. Chen[27], J. Chen[58c], J. Chen[24], S. Chen[132], S.J. Chen[13c], X. Chen[58c], X. Chen[13b], Y. Chen[58a], Y-H. Chen[44], C.L. Cheng[176], H.C. Cheng[60a], A. Cheplakov[77], E. Cheremushkina[44], E. Cherepanova[77], R. Cherkaoui El Moursli[33e], E. Cheu[6], K. Cheung[61], L. Chevalier[140], V. Chiarella[49], G. Chiarelli[69a], G. Chiodini[65a], A.S. Chisholm[19], A. Chitan[25b], Y.H. Chiu[171], M.V. Chizhov[77,s], K. Choi[10], A.R. Chomont[70a,70b], Y. Chou[99], Y.S. Chow[115], T. Chowdhury[31f], L.D. Christopher[31f], M.C. Chu[60a], X. Chu[13a,13d], J. Chudoba[136], J.J. Chwastowski[82], D. Cieri[111], K.M. Ciesla[82], V. Cindro[89], I.A. Cioară[25b], A. Ciocio[16], F. Cirotto[67a,67b], Z.H. Citron[175,k], M. Citterio[66a], D.A. Ciubotaru[25b], B.M. Ciungu[162], A. Clark[52], P.J. Clark[48], J.M. Clavijo Columbie[44], S.E. Clawson[97], C. Clement[43a,43b], L. Clissa[21b,21a], Y. Coadou[98], M. Cobal[64a,64c], A. Coccaro[53b], J. Cochran[76], R.F. Coelho Barrue[135a], R. Coelho Lopes De Sa[99], S. Coelli[66a], H. Cohen[157], A.E.C. Coimbra[34], B. Cole[37], J. Collot[56], P. Conde Muiño[135a,135g], S.H. Connell[31c], I.A. Connelly[55], E.I. Conroy[130], F. Conventi[67a,ak], H.G. Cooke[19], A.M. Cooper-Sarkar[130], F. Cormier[170], L.D. Corpe[34], M. Corradi[70a,70b], E.E. Corrigan[94], F. Corriveau[100,y], M.J. Costa[169], F. Costanza[4], D. Costanzo[145], B.M. Cote[123], G. Cowan[91], J.W. Cowley[30], K. Cranmer[121], S. Crépé-Renaudin[56], F. Crescioli[131], M. Cristinziani[147], M. Cristoforetti[73a,73b,b], V. Croft[165], G. Crosetti[39b,39a], A. Cueto[34],

T. Cuhadar Donszelmann[166], H. Cui[13a,13d], A.R. Cukierman[149], W.R. Cunningham[55], F. Curcio[39b,39a], P. Czodrowski[34], M.M. Czurylo[59b], M.J. Da Cunha Sargedas De Sousa[58a], J.V. Da Fonseca Pinto[78b], C. Da Via[97], W. Dabrowski[81a], T. Dado[45], S. Dahbi[31f], T. Dai[102], C. Dallapiccola[99], M. Dam[38], G. D'amen[27], V. D'Amico[72a,72b], J. Damp[96], J.R. Dandoy[132], M.F. Daneri[28], M. Danninger[148], V. Dao[34], G. Darbo[53b], S. Darmora[5], A. Dattagupta[127], S. D'Auria[66a,66b], C. David[163b], T. Davidek[138], D.R. Davis[47], B. Davis-Purcell[32], I. Dawson[90], K. De[7], R. De Asmundis[67a], M. De Beurs[115], S. De Castro[21b,21a], N. De Groot[114], P. de Jong[115], H. De la Torre[103], A. De Maria[13c], D. De Pedis[70a], A. De Salvo[70a], U. De Sanctis[71a,71b], M. De Santis[71a,71b], A. De Santo[152], J.B. De Vivie De Regie[56], D.V. Dedovich[77], J. Degens[115], A.M. Deiana[40], J. Del Peso[95], Y. Delabat Diaz[44], F. Deliot[140], C.M. Delitzsch[6], M. Della Pietra[67a,67b], D. Della Volpe[52], A. Dell'Acqua[34], L. Dell'Asta[66a,66b], M. Delmastro[4], P.A. Delsart[56], S. Demers[178], M. Demichev[77], S.P. Denisov[118], L. D'Eramo[116], D. Derendarz[82], J.E. Derkaoui[33d], F. Derue[131], P. Dervan[88], K. Desch[22], K. Dette[162], C. Deutsch[22], P.O. Deviveiros[34], F.A. Di Bello[70a,70b], A. Di Ciaccio[71a,71b], L. Di Ciaccio[4], A. Di Domenico[70a,70b], C. Di Donato[67a,67b], A. Di Girolamo[34], G. Di Gregorio[69a,69b], A. Di Luca[73a,73b], B. Di Micco[72a,72b], R. Di Nardo[72a,72b], C. Diaconu[98], F.A. Dias[115], T. Dias Do Vale[135a], M.A. Diaz[142a], F.G. Diaz Capriles[22], J. Dickinson[16], M. Didenko[169], E.B. Diehl[102], J. Dietrich[17], S. Díez Cornell[44], C. Diez Pardos[147], A. Dimitrievska[16], W. Ding[13b], J. Dingfelder[22], I-M. Dinu[25b], S.J. Dittmeier[59b], F. Dittus[34], F. Djama[98], T. Djobava[155b], J.I. Djuvsland[15], M.A.B. Do Vale[143], D. Dodsworth[24], C. Doglioni[94], J. Dolejsi[138], Z. Dolezal[138], M. Donadelli[78c], B. Dong[58c], J. Donini[36], A. D'onofrio[13c], M. D'Onofrio[88], J. Dopke[139], A. Doria[67a], M.T. Dova[86], A.T. Doyle[55], E. Drechsler[148], E. Dreyer[148], T. Dreyer[51], A.S. Drobac[165], D. Du[58a], T.A. du Pree[115], F. Dubinin[107], M. Dubovsky[26a], A. Dubreuil[52], E. Duchovni[175], G. Duckeck[110], O.A. Ducu[34,25b], D. Duda[111], A. Dudarev[34], M. D'uffizi[97], L. Duflot[62], M. Dührssen[34], C. Dülsen[177], A.E. Dumitriu[25b], M. Dunford[59a], S. Dungs[45], K. Dunne[43a,43b], A. Duperrin[98], H. Duran Yildiz[3a], M. Düren[54], A. Durglishvili[155b], B. Dutta[44], G.I. Dyckes[16], M. Dyndal[81a], S. Dysch[97], B.S. Dziedzic[82], B. Eckerova[26a], M.G. Eggleston[47], E. Egidio Purcino De Souza[78b], L.F. Ehrke[52], T. Eifert[7], G. Eigen[15], K. Einsweiler[16], T. Ekelof[167], Y. El Ghazali[33b], H. El Jarrari[33e], A. El Moussaouy[33a], V. Ellajosyula[167], M. Ellert[167], F. Ellinghaus[177], A.A. Elliot[90], N. Ellis[34], J. Elmsheuser[27], M. Elsing[34], D. Emeliyanov[139], A. Emerman[37], Y. Enari[159], J. Erdmann[45], A. Ereditato[18], P.A. Erland[82], M. Errenst[177], M. Escalier[62], C. Escobar[169], O. Estrada Pastor[169], E. Etzion[157], G. Evans[135a], H. Evans[63], M.O. Evans[152], A. Ezhilov[133], F. Fabbri[55], L. Fabbri[21b,21a], G. Facini[173], V. Fadeyev[141], R.M. Fakhrutdinov[118], S. Falciano[70a], P.J. Falke[22], S. Falke[34], J. Faltova[138], Y. Fan[13a], Y. Fang[13a], G. Fanourakis[42], M. Fanti[66a,66b], M. Faraj[58c], A. Farbin[7], A. Farilla[72a], E.M. Farina[68a,68b], T. Farooque[103], S.M. Farrington[48], P. Farthouat[34], F. Fassi[33e], D. Fassouliotis[8], M. Faucci Giannelli[71a,71b], W.J. Fawcett[30], L. Fayard[62], O.L. Fedin[133,p], M. Feickert[168], L. Feligioni[98], A. Fell[145], C. Feng[58b], M. Feng[13b], M.J. Fenton[166], A.B. Fenyuk[118], S.W. Ferguson[41], J. Ferrando[44], A. Ferrari[167], P. Ferrari[115], R. Ferrari[68a], D. Ferrere[52], C. Ferretti[102], F. Fiedler[96], A. Filipčič[89], F. Filthaut[114], M.C.N. Fiolhais[135a,135c,a], L. Fiorini[169], F. Fischer[147], W.C. Fisher[103], T. Fitschen[19], I. Fleck[147], P. Fleischmann[102], T. Flick[177], B.M. Flierl[110], L. Flores[132], M. Flores[31d], L.R. Flores Castillo[60a], F.M. Follega[73a,73b], N. Fomin[15], J.H. Foo[162], B.C. Forland[63], A. Formica[140], F.A. Förster[12], A.C. Forti[97], E. Fortin[98], M.G. Foti[130], L. Fountas[8], D. Fournier[62], H. Fox[87], P. Francavilla[69a,69b], S. Francescato[57], M. Franchini[21b,21a], S. Franchino[59a], D. Francis[34], L. Franco[4], L. Franconi[18], M. Franklin[57], G. Frattari[70a,70b], A.C. Freegard[90], P.M. Freeman[19], W.S. Freund[78b], E.M. Freundlich[45], D. Froidevaux[34], J.A. Frost[130], Y. Fu[58a], M. Fujimoto[122], E. Fullana Torregrosa[169], J. Fuster[169], A. Gabrielli[21b,21a], A. Gabrielli[34], P. Gadow[44], G. Gagliardi[53b,53a], L.G. Gagnon[16], G.E. Gallardo[130], E.J. Gallas[130], B.J. Gallop[139], R. Gamboa Goni[90], K.K. Gan[123], S. Ganguly[159], J. Gao[58a], Y. Gao[48], Y.S. Gao[29,m], F.M. Garay Walls[142a], C. García[169], J.E. García Navarro[169], J.A. García Pascual[13a], M. Garcia-Sciveres[16], R.W. Gardner[35], D. Garg[75], R.B. Garg[149], S. Gargiulo[50], C.A. Garner[162], V. Garonne[129], S.J. Gasiorowski[144], P. Gaspar[78b], G. Gaudio[68a], P. Gauzzi[70a,70b], I.L. Gavrilenko[107],

A. Gavrilyuk[119], C. Gay[170], G. Gaycken[44], E.N. Gazis[9], A.A. Geanta[25b], C.M. Gee[141], C.N.P. Gee[139], J. Geisen[94], M. Geisen[96], C. Gemme[53b], M.H. Genest[56], S. Gentile[70a,70b], S. George[91], W.F. George[19], T. Geralis[42], L.O. Gerlach[51], P. Gessinger-Befurt[34], M. Ghasemi Bostanabad[171], A. Ghosh[166], A. Ghosh[75], B. Giacobbe[21b], S. Giagu[70a,70b], N. Giangiacomi[162], P. Giannetti[69a], A. Giannini[67a,67b], S.M. Gibson[91], M. Gignac[141], D.T. Gil[81b], B.J. Gilbert[37], D. Gillberg[32], G. Gilles[115], N.E.K. Gillwald[44], D.M. Gingrich[2,aj], M.P. Giordani[64a,64c], P.F. Giraud[140], G. Giugliarelli[64a,64c], D. Giugni[66a], F. Giuli[71a,71b], I. Gkialas[8,h], P. Gkountoumis[9], L.K. Gladilin[109], C. Glasman[95], G.R. Gledhill[127], M. Glisic[127], I. Gnesi[39b,d], M. Goblirsch-Kolb[24], D. Godin[106], S. Goldfarb[101], T. Golling[52], D. Golubkov[118], J.P. Gombas[103], A. Gomes[135a,135b], R. Goncalves Gama[51], R. Gonçalo[135a,135c], G. Gonella[127], L. Gonella[19], A. Gongadze[77], F. Gonnella[19], J.L. Gonski[37], S. González de la Hoz[169], S. Gonzalez Fernandez[12], R. Gonzalez Lopez[88], C. Gonzalez Renteria[16], R. Gonzalez Suarez[167], S. Gonzalez-Sevilla[52], G.R. Gonzalvo Rodriguez[169], R.Y. González Andana[142a], L. Goossens[34], N.A. Gorasia[19], P.A. Gorbounov[119], H.A. Gordon[27], B. Gorini[34], E. Gorini[65a,65b], A. Gorišek[89], A.T. Goshaw[47], M.I. Gostkin[77], C.A. Gottardo[114], M. Gouighri[33b], V. Goumarre[44], A.G. Goussiou[144], N. Govender[31c], C. Goy[4], I. Grabowska-Bold[81a], K. Graham[32], E. Gramstad[129], S. Grancagnolo[17], M. Grandi[152], V. Gratchev[133], P.M. Gravila[25f], F.G. Gravili[65a,65b], H.M. Gray[16], C. Grefe[22], I.M. Gregor[44], P. Grenier[149], K. Grevtsov[44], C. Grieco[12], N.A. Grieser[124], A.A. Grillo[141], K. Grimm[29,l], S. Grinstein[12,v], J.-F. Grivaz[62], S. Groh[96], E. Gross[175], J. Grosse-Knetter[51], C. Grud[102], A. Grummer[113], J.C. Grundy[130], L. Guan[102], W. Guan[176], C. Gubbels[170], J. Guenther[34], J.G.R. Guerrero Rojas[169], F. Guescini[111], D. Guest[17], R. Gugel[96], A. Guida[44], T. Guillemin[4], S. Guindon[34], J. Guo[58c], L. Guo[62], Y. Guo[102], R. Gupta[44], S. Gurbuz[22], G. Gustavino[124], M. Guth[52], P. Gutierrez[124], L.F. Gutierrez Zagazeta[132], C. Gutschow[92], C. Guyot[140], C. Gwenlan[130], C.B. Gwilliam[88], E.S. Haaland[129], A. Haas[121], M. Habedank[44], C. Haber[16], H.K. Hadavand[7], A. Hadef[96], S. Hadzic[111], M. Haleem[172], J. Haley[125], J.J. Hall[145], G. Halladjian[103], G.D. Hallewell[98], L. Halser[18], K. Hamano[171], H. Hamdaoui[33e], M. Hamer[22], G.N. Hamity[48], K. Han[58a], L. Han[13c], L. Han[58a], S. Han[16], Y.F. Han[162], K. Hanagaki[79,t], M. Hance[141], M.D. Hank[35], R. Hankache[97], E. Hansen[94], J.B. Hansen[38], J.D. Hansen[38], M.C. Hansen[22], P.H. Hansen[38], K. Hara[164], T. Harenberg[177], S. Harkusha[104], Y.T. Harris[130], P.F. Harrison[173], N.M. Hartman[149], N.M. Hartmann[110], Y. Hasegawa[146], A. Hasib[48], S. Hassani[140], S. Haug[18], R. Hauser[103], M. Havranek[137], C.M. Hawkes[19], R.J. Hawkings[34], S. Hayashida[112], D. Hayden[103], C. Hayes[102], R.L. Hayes[170], C.P. Hays[130], J.M. Hays[90], H.S. Hayward[88], S.J. Haywood[139], F. He[58a], Y. He[160], Y. He[131], M.P. Heath[48], V. Hedberg[94], A.L. Heggelund[129], N.D. Hehir[90], C. Heidegger[50], K.K. Heidegger[50], W.D. Heidorn[76], J. Heilman[32], S. Heim[44], T. Heim[16], B. Heinemann[44,ah], J.G. Heinlein[132], J.J. Heinrich[127], L. Heinrich[34], J. Hejbal[136], L. Helary[44], A. Held[121], C.M. Helling[141], S. Hellman[43a,43b], C. Helsens[34], R.C.W. Henderson[87], L. Henkelmann[30], A.M. Henriques Correia[34], H. Herde[149], Y. Hernández Jiménez[151], H. Herr[96], M.G. Herrmann[110], T. Herrmann[46], G. Herten[50], R. Hertenberger[110], L. Hervas[34], N.P. Hessey[163a], H. Hibi[80], S. Higashino[79], E. Higón-Rodriguez[169], K.H. Hiller[44], S.J. Hillier[19], M. Hils[46], I. Hinchliffe[16], F. Hinterkeuser[22], M. Hirose[128], S. Hirose[164], D. Hirschbuehl[177], B. Hiti[89], O. Hladik[136], J. Hobbs[151], R. Hobincu[25e], N. Hod[175], M.C. Hodgkinson[145], B.H. Hodkinson[30], A. Hoecker[34], J. Hofer[44], D. Hohn[50], T. Holm[22], T.R. Holmes[35], M. Holzbock[111], L.B.A.H. Hommels[30], B.P. Honan[97], J. Hong[58c], T.M. Hong[134], Y. Hong[51], J.C. Honig[50], A. Hönle[111], B.H. Hooberman[168], W.H. Hopkins[5], Y. Horii[112], L.A. Horyn[35], S. Hou[154], J. Howarth[55], J. Hoya[86], M. Hrabovsky[126], A. Hrynevich[105], T. Hryn'ova[4], P.J. Hsu[61], S.-C. Hsu[144], Q. Hu[37], S. Hu[58c], Y.F. Hu[13a,13d,al], D.P. Huang[92], X. Huang[13c], Y. Huang[58a], Y. Huang[13a], Z. Hubacek[137], F. Hubaut[98], M. Huebner[22], F. Huegging[22], T.B. Huffman[130], M. Huhtinen[34], S.K. Huiberts[15], R. Hulsken[56], N. Huseynov[77,z], J. Huston[103], J. Huth[57], R. Hyneman[149], S. Hyrych[26a], G. Iacobucci[52], G. Iakovidis[27], I. Ibragimov[147], L. Iconomidou-Fayard[62], P. Iengo[34], R. Iguchi[159], T. Iizawa[52], Y. Ikegami[79], A. Ilg[18], N. Ilic[162], H. Imam[33a], T. Ingebretsen Carlson[43a,43b], G. Introzzi[68a,68b], M. Iodice[72a], V. Ippolito[70a,70b], M. Ishino[159], W. Islam[176], C. Issever[17,44], S. Istin[11c,am],

J.M. Iturbe Ponce[60a], R. Iuppa[73a,73b], A. Ivina[175], J.M. Izen[41], V. Izzo[67a], P. Jacka[136], P. Jackson[1], R.M. Jacobs[44], B.P. Jaeger[148], C.S. Jagfeld[110], G. Jäkel[177], K. Jakobs[50], T. Jakoubek[175], J. Jamieson[55], K.W. Janas[81a], G. Jarlskog[94], A.E. Jaspan[88], N. Javadov[77,z], T. Javůrek[34], M. Javurkova[99], F. Jeanneau[140], L. Jeanty[127], J. Jejelava[155a,aa], P. Jenni[50,e], S. Jézéquel[4], J. Jia[151], Z. Jia[13c], Y. Jiang[58a], S. Jiggins[48], J. Jimenez Pena[111], S. Jin[13c], A. Jinaru[25b], O. Jinnouchi[160], H. Jivan[31f], P. Johansson[145], K.A. Johns[6], C.A. Johnson[63], D.M. Jones[30], E. Jones[173], R.W.L. Jones[87], T.J. Jones[88], J. Jovicevic[14], X. Ju[16], J.J. Junggeburth[34], A. Juste Rozas[12,v], S. Kabana[142d], A. Kaczmarska[82], M. Kado[70a,70b], H. Kagan[123], M. Kagan[149], A. Kahn[37], A. Kahn[132], C. Kahra[96], T. Kaji[174], E. Kajomovitz[156], C.W. Kalderon[27], A. Kamenshchikov[118], M. Kaneda[159], N.J. Kang[141], S. Kang[76], Y. Kano[112], D. Kar[31f], K. Karava[130], M.J. Kareem[163b], I. Karkanias[158], S.N. Karpov[77], Z.M. Karpova[77], V. Kartvelishvili[87], A.N. Karyukhin[118], E. Kasimi[158], C. Kato[58d], J. Katzy[44], K. Kawade[146], K. Kawagoe[85], T. Kawaguchi[112], T. Kawamoto[140], G. Kawamura[51], E.F. Kay[171], F.I. Kaya[165], S. Kazakos[12], V.F. Kazanin[117b,117a], Y. Ke[151], J.M. Keaveney[31a], R. Keeler[171], J.S. Keller[32], A.S. Kelly[92], D. Kelsey[152], J.J. Kempster[19], J. Kendrick[19], K.E. Kennedy[37], O. Kepka[136], S. Kersten[177], B.P. Kerševan[89], S. Ketabchi Haghighat[162], M. Khandoga[131], A. Khanov[125], A.G. Kharlamov[117b,117a], T. Kharlamova[117b,117a], E.E. Khoda[144], T.J. Khoo[17], G. Khoriauli[172], E. Khramov[77], J. Khubua[155b], S. Kido[80], M. Kiehn[34], A. Kilgallon[127], E. Kim[160], Y.K. Kim[35], N. Kimura[92], A. Kirchhoff[51], D. Kirchmeier[46], C. Kirfel[22], J. Kirk[139], A.E. Kiryunin[111], T. Kishimoto[159], D.P. Kisliuk[162], C. Kitsaki[9], O. Kivernyk[22], T. Klapdor-Kleingrothaus[50], M. Klassen[59a], C. Klein[32], L. Klein[172], M.H. Klein[102], M. Klein[88], U. Klein[88], P. Klimek[34], A. Klimentov[27], F. Klimpel[111], T. Klingl[22], T. Klioutchnikova[34], F.F. Klitzner[110], P. Kluit[115], S. Kluth[111], E. Kneringer[74], T.M. Knight[162], A. Knue[50], D. Kobayashi[85], R. Kobayashi[83], M. Kobel[46], M. Kocian[149], T. Kodama[159], P. Kodys[138], D.M. Koeck[152], P.T. Koenig[22], T. Koffas[32], N.M. Köhler[34], M. Kolb[140], I. Koletsou[4], T. Komarek[126], K. Köneke[50], A.X.Y. Kong[1], T. Kono[122], V. Konstantinides[92], N. Konstantinidis[92], B. Konya[94], R. Kopeliansky[63], S. Koperny[81a], K. Korcyl[82], K. Kordas[158], G. Koren[157], A. Korn[92], S. Korn[51], I. Korolkov[12], E.V. Korolkova[145], N. Korotkova[109], B. Kortman[115], O. Kortner[111], S. Kortner[111], W.H. Kostecka[116], V.V. Kostyukhin[147,161], A. Kotsokechagia[62], A. Kotwal[47], A. Koulouris[34], A. Kourkoumeli-Charalampidi[68a,68b], C. Kourkoumelis[8], E. Kourlitis[5], O. Kovanda[152], R. Kowalewski[171], W. Kozanecki[140], A.S. Kozhin[118], V.A. Kramarenko[109], G. Kramberger[89], P. Kramer[96], D. Krasnopevtsev[58a], M.W. Krasny[131], A. Krasznahorkay[34], J.A. Kremer[96], J. Kretzschmar[88], K. Kreul[17], P. Krieger[162], F. Krieter[110], S. Krishnamurthy[99], A. Krishnan[59b], M. Krivos[138], K. Krizka[16], K. Kroeninger[45], H. Kroha[111], J. Kroll[136], J. Kroll[132], K.S. Krowpman[103], U. Kruchonak[77], H. Krüger[22], N. Krumnack[76], M.C. Kruse[47], J.A. Krzysiak[82], A. Kubota[160], O. Kuchinskaia[161], S. Kuday[3a], D. Kuechler[44], J.T. Kuechler[44], S. Kuehn[34], T. Kuhl[44], V. Kukhtin[77], Y. Kulchitsky[104,ad], S. Kuleshov[142c], M. Kumar[31f], N. Kumari[98], M. Kuna[56], A. Kupco[136], T. Kupfer[45], O. Kuprash[50], H. Kurashige[80], L.L. Kurchaninov[163a], Y.A. Kurochkin[104], A. Kurova[108], M.G. Kurth[13a,13d], E.S. Kuwertz[34], M. Kuze[160], A.K. Kvam[144], J. Kvita[126], T. Kwan[100], K.W. Kwok[60a], C. Lacasta[169], F. Lacava[70a,70b], H. Lacker[17], D. Lacour[131], N.N. Lad[92], E. Ladygin[77], R. Lafaye[4], B. Laforge[131], T. Lagouri[142d], S. Lai[51], I.K. Lakomiec[81a], N. Lalloue[56], J.E. Lambert[124], S. Lammers[63], W. Lampl[6], C. Lampoudis[158], E. Lançon[27], U. Landgraf[50], M.P.J. Landon[90], V.S. Lang[50], J.C. Lange[51], R.J. Langenberg[99], A.J. Lankford[166], F. Lanni[27], K. Lantzsch[22], A. Lanza[68a], A. Lapertosa[53b,53a], J.F. Laporte[140], T. Lari[66a], F. Lasagni Manghi[21b], M. Lassnig[34], V. Latonova[136], T.S. Lau[60a], A. Laudrain[96], A. Laurier[32], M. Lavorgna[67a,67b], S.D. Lawlor[91], Z. Lawrence[97], M. Lazzaroni[66a,66b], B. Le[97], B. Leban[89], A. Lebedev[76], M. LeBlanc[34], T. LeCompte[5], F. Ledroit-Guillon[56], A.C.A. Lee[92], G.R. Lee[15], L. Lee[57], S.C. Lee[154], S. Lee[76], L.L. Leeuw[31c], B. Lefebvre[163a], H.P. Lefebvre[91], M. Lefebvre[171], C. Leggett[16], K. Lehmann[148], N. Lehmann[18], G. Lehmann Miotto[34], W.A. Leight[44], A. Leisos[158,u], M.A.L. Leite[78c], C.E. Leitgeb[44], R. Leitner[138], K.J.C. Leney[40], T. Lenz[22], S. Leone[69a], C. Leonidopoulos[48], A. Leopold[150], C. Leroy[106], R. Les[103], C.G. Lester[30], M. Levchenko[133], J. Levêque[4], D. Levin[102], L.J. Levinson[175],

D.J. Lewis[19], B. Li[13b], B. Li[58b], C. Li[58a], C-Q. Li[58c,58d], H. Li[58a], H. Li[58b], H. Li[58b], J. Li[58c], K. Li[144], L. Li[58c], M. Li[13a,13d], Q.Y. Li[58a], S. Li[58d,58c,c], T. Li[58b], X. Li[44], Y. Li[44], Z. Li[58b], Z. Li[130], Z. Li[100], Z. Li[88], Z. Liang[13a], M. Liberatore[44], B. Liberti[71a], K. Lie[60c], J. Lieber Marin[78b], K. Lin[103], R.A. Linck[63], R.E. Lindley[6], J.H. Lindon[2], A. Linss[44], E. Lipeles[132], A. Lipniacka[15], T.M. Liss[168,ai], A. Lister[170], J.D. Little[7], B. Liu[13a], B.X. Liu[148], J.B. Liu[58a], J.K.K. Liu[35], K. Liu[58d,58c], M. Liu[58a], M.Y. Liu[58a], P. Liu[13a], X. Liu[58a], Y. Liu[44], Y. Liu[13c,13d], Y.L. Liu[102], Y.W. Liu[58a], M. Livan[68a,68b], J. Llorente Merino[148], S.L. Lloyd[90], E.M. Lobodzinska[44], P. Loch[6], S. Loffredo[71a,71b], T. Lohse[17], K. Lohwasser[145], M. Lokajicek[136], J.D. Long[168], I. Longarini[70a,70b], L. Longo[34], R. Longo[168], I. Lopez Paz[12], A. Lopez Solis[44], J. Lorenz[110], N. Lorenzo Martinez[4], A.M. Lory[110], A. Lösle[50], X. Lou[43a,43b], X. Lou[13a], A. Lounis[62], J. Love[5], P.A. Love[87], J.J. Lozano Bahilo[169], G. Lu[13a], M. Lu[58a], S. Lu[132], Y.J. Lu[61], H.J. Lubatti[144], C. Luci[70a,70b], F.L. Lucio Alves[13c], A. Lucotte[56], F. Luehring[63], I. Luise[151], L. Luminari[70a], O. Lundberg[150], B. Lund-Jensen[150], N.A. Luongo[127], M.S. Lutz[157], D. Lynn[27], H. Lyons[88], R. Lysak[136], E. Lytken[94], F. Lyu[13a], V. Lyubushkin[77], T. Lyubushkina[77], H. Ma[27], L.L. Ma[58b], Y. Ma[92], D.M. Mac Donell[171], G. Maccarrone[49], C.M. Macdonald[145], J.C. MacDonald[145], R. Madar[36], W.F. Mader[46], M. Madugoda Ralalage Don[125], N. Madysa[46], J. Maeda[80], T. Maeno[27], M. Maerker[46], V. Magerl[50], J. Magro[64a,64c], D.J. Mahon[37], C. Maidantchik[78b], A. Maio[135a,135b,135d], K. Maj[81a], O. Majersky[26a], S. Majewski[127], N. Makovec[62], V. Maksimovic[14], B. Malaescu[131], Pa. Malecki[82], V.P. Maleev[133], F. Malek[56], D. Malito[39b,39a], U. Mallik[75], C. Malone[30], S. Maltezos[9], S. Malyukov[77], J. Mamuzic[169], G. Mancini[49], J.P. Mandalia[90], I. Mandić[89], L. Manhaes de Andrade Filho[78a], I.M. Maniatis[158], M. Manisha[140], J. Manjarres Ramos[46], K.H. Mankinen[94], A. Mann[110], A. Manousos[74], B. Mansoulie[140], I. Manthos[158], S. Manzoni[115], A. Marantis[158,u], G. Marchiori[131], M. Marcisovsky[136], L. Marcoccia[71a,71b], C. Marcon[94], M. Marjanovic[124], Z. Marshall[16], S. Marti-Garcia[169], T.A. Martin[173], V.J. Martin[48], B. Martin dit Latour[15], L. Martinelli[70a,70b], M. Martinez[12,v], P. Martinez Agullo[169], V.I. Martinez Outschoorn[99], S. Martin-Haugh[139], V.S. Martoiu[25b], A.C. Martyniuk[92], A. Marzin[34], S.R. Maschek[111], L. Masetti[96], T. Mashimo[159], J. Masik[97], A.L. Maslennikov[117b,117a], L. Massa[21b], P. Massarotti[67a,67b], P. Mastrandrea[69a,69b], A. Mastroberardino[39b,39a], T. Masubuchi[159], D. Matakias[27], T. Mathisen[167], A. Matic[110], N. Matsuzawa[159], J. Maurer[25b], B. Maček[89], D.A. Maximov[117b,117a], R. Mazini[154], I. Maznas[158], S.M. Mazza[141], C. Mc Ginn[27], J.P. Mc Gowan[100], S.P. Mc Kee[102], T.G. McCarthy[111], W.P. McCormack[16], E.F. McDonald[101], A.E. McDougall[115], J.A. Mcfayden[152], G. Mchedlidze[155b], M.A. McKay[40], K.D. McLean[171], S.J. McMahon[139], P.C. McNamara[101], R.A. McPherson[171,y], J.E. Mdhluli[31f], Z.A. Meadows[99], S. Meehan[34], T. Megy[36], S. Mehlhase[110], A. Mehta[88], B. Meirose[41], D. Melini[156], B.R. Mellado Garcia[31f], A.H. Melo[51], F. Meloni[44], A. Melzer[22], E.D. Mendes Gouveia[135a], A.M. Mendes Jacques Da Costa[19], H.Y. Meng[162], L. Meng[34], S. Menke[111], M. Mentink[34], E. Meoni[39b,39a], C. Merlassino[130], P. Mermod[52,*], L. Merola[67a,67b], C. Meroni[66a], G. Merz[102], O. Meshkov[107,109], J.K.R. Meshreki[147], J. Metcalfe[5], A.S. Mete[5], C. Meyer[63], J-P. Meyer[140], M. Michetti[17], R.P. Middleton[139], L. Mijović[48], G. Mikenberg[175], M. Mikestikova[136], M. Mikuž[89], H. Mildner[145], A. Milic[162], C.D. Milke[40], D.W. Miller[35], L.S. Miller[32], A. Milov[175], D.A. Milstead[43a,43b], T. Min[13c], A.A. Minaenko[118], I.A. Minashvili[155b], L. Mince[55], A.I. Mincer[121], B. Mindur[81a], M. Mineev[77], Y. Minegishi[159], Y. Mino[83], L.M. Mir[12], M. Miralles Lopez[169], M. Mironova[130], T. Mitani[174], V.A. Mitsou[169], M. Mittal[58c], O. Miu[162], P.S. Miyagawa[90], Y. Miyazaki[85], A. Mizukami[79], J.U. Mjörnmark[94], T. Mkrtchyan[59a], M. Mlynarikova[116], T. Moa[43a,43b], S. Mobius[51], K. Mochizuki[106], P. Moder[44], P. Mogg[110], A.F. Mohammed[13a], S. Mohapatra[37], G. Mokgatitswane[31f], B. Mondal[147], S. Mondal[137], K. Mönig[44], E. Monnier[98], L. Monsonis Romero[169], A. Montalbano[148], J. Montejo Berlingen[34], M. Montella[123], F. Monticelli[86], N. Morange[62], A.L. Moreira De Carvalho[135a], M. Moreno Llácer[169], C. Moreno Martinez[12], P. Morettini[53b], S. Morgenstern[173], D. Mori[148], M. Morii[57], M. Morinaga[159], V. Morisbak[129], A.K. Morley[34], A.P. Morris[92], L. Morvaj[34], P. Moschovakos[34], B. Moser[115], M. Mosidze[155b], T. Moskalets[50], P. Moskvitina[114], J. Moss[29,n], E.J.W. Moyse[99], S. Muanza[98],

J. Mueller[134], R. Mueller[18], D. Muenstermann[87], G.A. Mullier[94], J.J. Mullin[132], D.P. Mungo[66a,66b], J.L. Munoz Martinez[12], F.J. Munoz Sanchez[97], M. Murin[97], P. Murin[26b], W.J. Murray[173,139], A. Murrone[66a,66b], J.M. Muse[124], M. Muškinja[16], C. Mwewa[27], A.G. Myagkov[118,ae], A.J. Myers[7], A.A. Myers[134], G. Myers[63], M. Myska[137], B.P. Nachman[16], O. Nackenhorst[45], A.Nag Nag[46], K. Nagai[130], K. Nagano[79], J.L. Nagle[27], E. Nagy[98], A.M. Nairz[34], Y. Nakahama[112], K. Nakamura[79], H. Nanjo[128], F. Napolitano[59a], R. Narayan[40], E.A. Narayanan[113], I. Naryshkin[133], M. Naseri[32], C. Nass[22], T. Naumann[44], G. Navarro[20a], J. Navarro-Gonzalez[169], R. Nayak[157], P.Y. Nechaeva[107], F. Nechansky[44], T.J. Neep[19], A. Negri[68a,68b], M. Negrini[21b], C. Nellist[114], C. Nelson[100], K. Nelson[102], S. Nemecek[136], M. Nessi[34,f], M.S. Neubauer[168], F. Neuhaus[96], J. Neundorf[44], R. Newhouse[170], P.R. Newman[19], C.W. Ng[134], Y.S. Ng[17], Y.W.Y. Ng[166], B. Ngair[33e], H.D.N. Nguyen[106], R.B. Nickerson[130], R. Nicolaidou[140], D.S. Nielsen[38], J. Nielsen[141], M. Niemeyer[51], N. Nikiforou[10], V. Nikolaenko[118,ae], I. Nikolic-Audit[131], K. Nikolopoulos[19], P. Nilsson[27], H.R. Nindhito[52], A. Nisati[70a], N. Nishu[2], R. Nisius[111], T. Nitta[174], T. Nobe[159], D.L. Noel[30], Y. Noguchi[83], I. Nomidis[131], M.A. Nomura[27], M.B. Norfolk[145], R.R.B. Norisam[92], J. Novak[89], T. Novak[44], O. Novgorodova[46], L. Novotny[137], R. Novotny[113], L. Nozka[126], K. Ntekas[166], E. Nurse[92], F.G. Oakham[32,aj], J. Ocariz[131], A. Ochi[80], I. Ochoa[135a], J.P. Ochoa-Ricoux[142a], S. Oda[85], S. Odaka[79], S. Oerdek[167], A. Ogrodnik[81a], A. Oh[97], C.C. Ohm[150], H. Oide[160], R. Oishi[159], M.L. Ojeda[44], Y. Okazaki[83], M.W. O'Keefe[88], Y. Okumura[159], A. Olariu[25b], L.F. Oleiro Seabra[135a], S.A. Olivares Pino[142d], D. Oliveira Damazio[27], D. Oliveira Goncalves[78a], J.L. Oliver[166], M.J.R. Olsson[166], A. Olszewski[82], J. Olszowska[82], Ö.O. Öncel[22], D.C. O'Neil[148], A.P. O'neill[130], A. Onofre[135a,135e], P.U.E. Onyisi[10], R.G. Oreamuno Madriz[116], M.J. Oreglia[35], G.E. Orellana[86], D. Orestano[72a,72b], N. Orlando[12], R.S. Orr[162], V. O'Shea[55], R. Ospanov[58a], G. Otero y Garzon[28], H. Otono[85], P.S. Ott[59a], G.J. Ottino[16], M. Ouchrif[33d], J. Ouellette[27], F. Ould-Saada[129], A. Ouraou[140,*], Q. Ouyang[13a], M. Owen[55], R.E. Owen[139], K.Y. Oyulmaz[11c], V.E. Ozcan[11c], N. Ozturk[7], S. Ozturk[11c], J. Pacalt[126], H.A. Pacey[30], K. Pachal[47], A. Pacheco Pages[12], C. Padilla Aranda[12], S. Pagan Griso[16], G. Palacino[63], S. Palazzo[48], S. Palestini[34], M. Palka[81b], P. Palni[81a], D.K. Panchal[10], C.E. Pandini[52], J.G. Panduro Vazquez[91], P. Pani[44], G. Panizzo[64a,64c], L. Paolozzi[52], C. Papadatos[106], S. Parajuli[40], A. Paramonov[5], C. Paraskevopoulos[9], D. Paredes Hernandez[60b], S.R. Paredes Saenz[130], B. Parida[175], T.H. Park[162], A.J. Parker[29], M.A. Parker[30], F. Parodi[53b,53a], E.W. Parrish[116], J.A. Parsons[37], U. Parzefall[50], L. Pascual Dominguez[157], V.R. Pascuzzi[16], F. Pasquali[115], E. Pasqualucci[70a], S. Passaggio[53b], F. Pastore[91], P. Pasuwan[43a,43b], J.R. Pater[97], A. Pathak[176], J. Patton[88], T. Pauly[34], J. Pearkes[149], M. Pedersen[129], L. Pedraza Diaz[114], R. Pedro[135a], T. Peiffer[51], S.V. Peleganchuk[117b,117a], O. Penc[136], C. Peng[60b], H. Peng[58a], M. Penzin[161], B.S. Peralva[78a], A.P. Pereira Peixoto[135a], L. Pereira Sanchez[43a,43b], D.V. Perepelitsa[27], E. Perez Codina[163a], M. Perganti[9], L. Perini[66a,66b], H. Pernegger[34], S. Perrella[34], A. Perrevoort[115], K. Peters[44], R.F.Y. Peters[97], B.A. Petersen[34], T.C. Petersen[38], E. Petit[98], V. Petousis[137], C. Petridou[158], P. Petroff[62], F. Petrucci[72a,72b], A. Petrukhin[147], M. Pettee[178], N.E. Pettersson[34], K. Petukhova[138], A. Peyaud[140], R. Pezoa[142e], L. Pezzotti[34], G. Pezzullo[178], T. Pham[101], P.W. Phillips[139], M.W. Phipps[168], G. Piacquadio[151], E. Pianori[16], F. Piazza[66a,66b], A. Picazio[99], R. Piegaia[28], D. Pietreanu[25b], J.E. Pilcher[35], A.D. Pilkington[97], M. Pinamonti[64a,64c], J.L. Pinfold[2], C. Pitman Donaldson[92], D.A. Pizzi[32], L. Pizzimento[71a,71b], A. Pizzini[115], M.-A. Pleier[27], V. Plesanovs[50], V. Pleskot[138], E. Plotnikova[77], P. Podberezko[117b,117a], R. Poettgen[94], R. Poggi[52], L. Poggioli[131], I. Pogrebnyak[103], D. Pohl[22], I. Pokharel[51], G. Polesello[68a], A. Poley[148,163a], A. Policicchio[70a,70b], R. Polifka[138], A. Polini[21b], C.S. Pollard[130], Z.B. Pollock[123], V. Polychronakos[27], D. Ponomarenko[108], L. Pontecorvo[34], S. Popa[25a], G.A. Popeneciu[25d], L. Portales[4], D.M. Portillo Quintero[163a], S. Pospisil[137], P. Postolache[25c], K. Potamianos[130], I.N. Potrap[77], C.J. Potter[30], H. Potti[1], T. Poulsen[44], J. Poveda[169], T.D. Powell[145], G. Pownall[44], M.E. Pozo Astigarraga[34], A. Prades Ibanez[169], P. Pralavorio[98], M.M. Prapa[42], S. Prell[76], D. Price[97], M. Primavera[65a], M.A. Principe Martin[95], M.L. Proffitt[144], N. Proklova[108], K. Prokofiev[60c], F. Prokoshin[77], S. Protopopescu[27], J. Proudfoot[5], M. Przybycien[81a], D. Pudzha[133], P. Puzo[62], D. Pyatiizbyantseva[108],

J. Qian[102], Y. Qin[97], T. Qiu[90], A. Quadt[51], M. Queitsch-Maitland[34], G. Rabanal Bolanos[57], F. Ragusa[66a,66b], J.A. Raine[52], S. Rajagopalan[27], K. Ran[13a,13d], D.F. Rassloff[59a], D.M. Rauch[44], S. Rave[96], B. Ravina[55], I. Ravinovich[175], M. Raymond[34], A.L. Read[129], N.P. Readioff[145], D.M. Rebuzzi[68a,68b], G. Redlinger[27], K. Reeves[41], D. Reikher[157], A. Reiss[96], A. Rej[147], C. Rembser[34], A. Renardi[44], M. Renda[25b], M.B. Rendel[111], A.G. Rennie[55], S. Resconi[66a], M. Ressegotti[53b,53a], E.D. Resseguie[16], S. Rettie[92], B. Reynolds[123], E. Reynolds[19], M. Rezaei Estabragh[177], O.L. Rezanova[117b,117a], P. Reznicek[138], E. Ricci[73a,73b], R. Richter[111], S. Richter[44], E. Richter-Was[81b], M. Ridel[131], P. Rieck[111], P. Riedler[34], O. Rifki[44], M. Rijssenbeek[151], A. Rimoldi[68a,68b], M. Rimoldi[44], L. Rinaldi[21b,21a], T.T. Rinn[168], M.P. Rinnagel[110], G. Ripellino[150], I. Riu[12], P. Rivadeneira[44], J.C. Rivera Vergara[171], F. Rizatdinova[125], E. Rizvi[90], C. Rizzi[52], B.A. Roberts[173], B.R. Roberts[16], S.H. Robertson[100,y], M. Robin[44], D. Robinson[30], C.M. Robles Gajardo[142e], M. Robles Manzano[96], A. Robson[55], A. Rocchi[71a,71b], C. Roda[69a,69b], S. Rodriguez Bosca[59a], A. Rodriguez Rodriguez[50], A.M. Rodríguez Vera[163b], S. Roe[34], A.R. Roepe[124], J. Roggel[177], O. Røhne[129], R.A. Rojas[171], B. Roland[50], C.P.A. Roland[63], J. Roloff[27], A. Romaniouk[108], M. Romano[21b], A.C. Romero Hernandez[168], N. Rompotis[88], M. Ronzani[121], L. Roos[131], S. Rosati[70a], B.J. Rosser[132], E. Rossi[162], E. Rossi[4], E. Rossi[67a,67b], L.P. Rossi[53b], L. Rossini[44], R. Rosten[123], M. Rotaru[25b], B. Rottler[50], D. Rousseau[62], D. Rousso[30], G. Rovelli[68a,68b], A. Roy[10], A. Rozanov[98], Y. Rozen[156], X. Ruan[31f], A.J. Ruby[88], T.A. Ruggeri[1], F. Rühr[50], A. Ruiz-Martinez[169], A. Rummler[34], Z. Rurikova[50], N.A. Rusakovich[77], H.L. Russell[34], L. Rustige[36], J.P. Rutherfoord[6], E.M. Rüttinger[145], M. Rybar[138], E.B. Rye[129], A. Ryzhov[118], J.A. Sabater Iglesias[44], P. Sabatini[169], L. Sabetta[70a,70b], H.F-W. Sadrozinski[141], R. Sadykov[77], F. Safai Tehrani[70a], B. Safarzadeh Samani[152], M. Safdari[149], S. Saha[100], M. Sahinsoy[111], A. Sahu[177], M. Saimpert[140], M. Saito[159], T. Saito[159], D. Salamani[34], G. Salamanna[72a,72b], A. Salnikov[149], J. Salt[169], A. Salvador Salas[12], D. Salvatore[39b,39a], F. Salvatore[152], A. Salzburger[34], D. Sammel[50], D. Sampsonidis[158], D. Sampsonidou[58d,58c], J. Sánchez[169], A. Sanchez Pineda[4], V. Sanchez Sebastian[169], H. Sandaker[129], C.O. Sander[44], I.G. Sanderswood[87], J.A. Sandesara[99], M. Sandhoff[177], C. Sandoval[20b], D.P.C. Sankey[139], M. Sannino[53b,53a], A. Sansoni[49], C. Santoni[36], H. Santos[135a,135b], S.N. Santpur[16], A. Santra[175], K.A. Saoucha[145], A. Sapronov[77], J.G. Saraiva[135a,135d], J. Sardain[98], O. Sasaki[79], K. Sato[164], C. Sauer[59b], F. Sauerburger[50], E. Sauvan[4], P. Savard[162,aj], R. Sawada[159], C. Sawyer[139], L. Sawyer[93], I. Sayago Galvan[169], C. Sbarra[21b], A. Sbrizzi[21b,21a], T. Scanlon[92], J. Schaarschmidt[144], P. Schacht[111], D. Schaefer[35], U. Schäfer[96], A.C. Schaffer[62], D. Schaile[110], R.D. Schamberger[151], E. Schanet[110], C. Scharf[17], N. Scharmberg[97], V.A. Schegelsky[133], D. Scheirich[138], F. Schenck[17], M. Schernau[166], C. Schiavi[53b,53a], L.K. Schildgen[22], Z.M. Schillaci[24], E.J. Schioppa[65a,65b], M. Schioppa[39b,39a], B. Schlag[96], K.E. Schleicher[50], S. Schlenker[34], K. Schmieden[96], C. Schmitt[96], S. Schmitt[44], L. Schoeffel[140], A. Schoening[59b], P.G. Scholer[50], E. Schopf[130], M. Schott[96], J. Schovancova[34], S. Schramm[52], F. Schroeder[177], H-C. Schultz-Coulon[59a], M. Schumacher[50], B.A. Schumm[141], Ph. Schune[140], A. Schwartzman[149], T.A. Schwarz[102], Ph. Schwemling[140], R. Schwienhorst[103], A. Sciandra[141], G. Sciolla[24], F. Scuri[69a], F. Scutti[101], C.D. Sebastiani[88], K. Sedlaczek[45], P. Seema[17], S.C. Seidel[113], A. Seiden[141], B.D. Seidlitz[27], T. Seiss[35], C. Seitz[44], J.M. Seixas[78b], G. Sekhniaidze[67a], S.J. Sekula[40], L. Selem[4], N. Semprini-Cesari[21b,21a], S. Sen[47], C. Serfon[27], L. Serin[62], L. Serkin[64a,64b], M. Sessa[72a,72b], H. Severini[124], S. Sevova[149], F. Sforza[53b,53a], A. Sfyrla[52], E. Shabalina[51], R. Shaheen[150], J.D. Shahinian[132], N.W. Shaikh[43a,43b], D. Shaked Renous[175], L.Y. Shan[13a], M. Shapiro[16], A. Sharma[34], A.S. Sharma[1], S. Sharma[44], P.B. Shatalov[119], K. Shaw[152], S.M. Shaw[97], P. Sherwood[92], L. Shi[92], C.O. Shimmin[178], Y. Shimogama[174], J.D. Shinner[91], I.P.J. Shipsey[130], S. Shirabe[52], M. Shiyakova[77], J. Shlomi[175], M.J. Shochet[35], J. Shojaii[101], D.R. Shope[150], S. Shrestha[123], E.M. Shrif[31f], M.J. Shroff[171], E. Shulga[175], P. Sicho[136], A.M. Sickles[168], E. Sideras Haddad[31f], O. Sidiropoulou[34], A. Sidoti[21b], F. Siegert[46], Dj. Sijacki[14], J.M. Silva[19], M.V. Silva Oliveira[34], S.B. Silverstein[43a], S. Simion[62], R. Simoniello[34], N.D. Simpson[94], S. Simsek[11b], P. Sinervo[162], V. Sinetckii[109], S. Singh[148], S. Singh[162],

S. Sinha[44], S. Sinha[31f], M. Sioli[21b,21a], I. Siral[127], S.Yu. Sivoklokov[109], J. Sjölin[43a,43b], A. Skaf[51], E. Skorda[94], P. Skubic[124], M. Slawinska[82], K. Sliwa[165], V. Smakhtin[175], B.H. Smart[139], J. Smiesko[138], S.Yu. Smirnov[108], Y. Smirnov[108], L.N. Smirnova[109,r], O. Smirnova[94], E.A. Smith[35], H.A. Smith[130], M. Smizanska[87], K. Smolek[137], A. Smykiewicz[82], A.A. Snesarev[107], H.L. Snoek[115], S. Snyder[27], R. Sobie[171,y], A. Soffer[157], F. Sohns[51], C.A. Solans Sanchez[34], E.Yu. Soldatov[108], U. Soldevila[169], A.A. Solodkov[118], S. Solomon[50], A. Soloshenko[77], O.V. Solovyanov[118], V. Solovyev[133], P. Sommer[145], H. Son[165], A. Sonay[12], W.Y. Song[163b], A. Sopczak[137], A.L. Sopio[92], F. Sopkova[26b], S. Sottocornola[68a,68b], R. Soualah[64a,64c], A.M. Soukharev[117b,117a], Z. Soumaimi[33e], D. South[44], S. Spagnolo[65a,65b], M. Spalla[111], M. Spangenberg[173], F. Spanò[91], D. Sperlich[50], T.M. Spieker[59a], G. Spigo[34], M. Spina[152], D.P. Spiteri[55], M. Spousta[138], A. Stabile[66a,66b], B.L. Stamas[116], R. Stamen[59a], M. Stamenkovic[115], A. Stampekis[19], M. Standke[22], E. Stanecka[82], B. Stanislaus[34], M.M. Stanitzki[44], M. Stankaityte[130], B. Stapf[44], E.A. Starchenko[118], G.H. Stark[141], J. Stark[98], D.M. Starko[163b], P. Staroba[136], P. Starovoitov[59a], S. Stärz[100], R. Staszewski[82], G. Stavropoulos[42], P. Steinberg[27], A.L. Steinhebel[127], B. Stelzer[148,163a], H.J. Stelzer[134], O. Stelzer-Chilton[163a], H. Stenzel[54], T.J. Stevenson[152], G.A. Stewart[34], M.C. Stockton[34], G. Stoicea[25b], M. Stolarski[135a], S. Stonjek[111], A. Straessner[46], J. Strandberg[150], S. Strandberg[43a,43b], M. Strauss[124], T. Strebler[98], P. Strizenec[26b], R. Ströhmer[172], D.M. Strom[127], L.R. Strom[44], R. Stroynowski[40], A. Strubig[43a,43b], S.A. Stucci[27], B. Stugu[15], J. Stupak[124], N.A. Styles[44], D. Su[149], S. Su[58a], W. Su[58d,144,58c], X. Su[58a], K. Sugizaki[159], V.V. Sulin[107], M.J. Sullivan[88], D.M.S. Sultan[52], L. Sultanaliyeva[107], S. Sultansoy[3c], T. Sumida[83], S. Sun[102], S. Sun[176], X. Sun[97], O. Sunneborn Gudnadottir[167], C.J.E. Suster[153], M.R. Sutton[152], M. Svatos[136], M. Swiatlowski[163a], T. Swirski[172], I. Sykora[26a], M. Sykora[138], T. Sykora[138], D. Ta[96], K. Tackmann[44,w], A. Taffard[166], R. Tafirout[163a], R.H.M. Taibah[131], R. Takashima[84], K. Takeda[80], T. Takeshita[146], E.P. Takeva[48], Y. Takubo[79], M. Talby[98], A.A. Talyshev[117b,117a], K.C. Tam[60b], N.M. Tamir[157], A. Tanaka[159], J. Tanaka[159], R. Tanaka[62], J. Tang[58c], Z. Tao[170], S. Tapia Araya[76], S. Tapprogge[96], A. Tarek Abouelfadl Mohamed[103], S. Tarem[156], K. Tariq[58b], G. Tarna[25b], G.F. Tartarelli[66a], P. Tas[138], M. Tasevsky[136], E. Tassi[39b,39a], G. Tateno[159], Y. Tayalati[33e], G.N. Taylor[101], W. Taylor[163b], H. Teagle[88], A.S. Tee[176], R. Teixeira De Lima[149], P. Teixeira-Dias[91], H. Ten Kate[34], J.J. Teoh[115], K. Terashi[159], J. Terron[95], S. Terzo[12], M. Testa[49], R.J. Teuscher[162,y], N. Themistokleous[48], T. Theveneaux-Pelzer[17], O. Thielmann[177], D.W. Thomas[91], J.P. Thomas[19], E.A. Thompson[44], P.D. Thompson[19], E. Thomson[132], E.J. Thorpe[90], Y. Tian[51], V.O. Tikhomirov[107,af], Yu.A. Tikhonov[117b,117a], S. Timoshenko[108], P. Tipton[178], S. Tisserant[98], S.H. Tlou[31f], A. Tnourji[36], K. Todome[21b,21a], S. Todorova-Nova[138], S. Todt[46], M. Togawa[79], J. Tojo[85], S. Tokár[26a], K. Tokushuku[79], E. Tolley[123], R. Tombs[30], M. Tomoto[79,112], L. Tompkins[149], P. Tornambe[99], E. Torrence[127], H. Torres[46], E. Torró Pastor[169], M. Toscani[28], C. Tosciri[35], M. Tost[10], J. Toth[98,x], D.R. Tovey[145], A. Traeet[15], C.J. Treado[121], T. Trefzger[172], A. Tricoli[27], I.M. Trigger[163a], S. Trincaz-Duvoid[131], D.A. Trischuk[170], W. Trischuk[162], B. Trocmé[56], A. Trofymov[62], C. Troncon[66a], F. Trovato[152], L. Truong[31c], M. Trzebinski[82], A. Trzupek[82], F. Tsai[151], A. Tsiamis[158], P.V. Tsiareshka[104,ad], A. Tsirigotis[158,u], V. Tsiskaridze[151], E.G. Tskhadadze[155a], M. Tsopoulou[158], Y. Tsujikawa[83], I.I. Tsukerman[119], V. Tsulaia[16], S. Tsuno[79], O. Tsur[156], D. Tsybychev[151], Y. Tu[60b], A. Tudorache[25b], V. Tudorache[25b], A.N. Tuna[34], S. Turchikhin[77], I. Turk Cakir[3a], R.J. Turner[19], R. Turra[66a], P.M. Tuts[37], S. Tzamarias[158], P. Tzanis[9], E. Tzovara[96], K. Uchida[159], F. Ukegawa[164], P.A. Ulloa Poblete[142c], G. Unal[34], M. Unal[10], A. Undrus[27], G. Unel[166], F.C. Ungaro[101], K. Uno[159], J. Urban[26b], P. Urquijo[101], G. Usai[7], R. Ushioda[160], M. Usman[106], Z. Uysal[11d], V. Vacek[137], B. Vachon[100], K.O.H. Vadla[129], T. Vafeiadis[34], C. Valderanis[110], E. Valdes Santurio[43a,43b], M. Valente[163a], S. Valentinetti[21b,21a], A. Valero[169], R.A. Vallance[19], A. Vallier[98], J.A. Valls Ferrer[169], T.R. Van Daalen[144], P. Van Gemmeren[5], S. Van Stroud[92], I. Van Vulpen[115], M. Vanadia[71a,71b], W. Vandelli[34], M. Vandenbroucke[140], E.R. Vandewall[125], D. Vannicola[157], L. Vannoli[53b,53a], R. Vari[70a], E.W. Varnes[6], C. Varni[16], T. Varol[154], D. Varouchas[62], K.E. Varvell[153], M.E. Vasile[25b], L. Vaslin[36], G.A. Vasquez[171], F. Vazeille[36], D. Vazquez Furelos[12], T. Vazquez Schroeder[34], J. Veatch[51], V. Vecchio[97],

M.J. Veen[115], I. Veliscek[130], L.M. Veloce[162], F. Veloso[135a,135c], S. Veneziano[70a], A. Ventura[65a,65b], A. Verbytskyi[111], M. Verducci[69a,69b], C. Vergis[22], M. Verissimo De Araujo[78b], W. Verkerke[115], A.T. Vermeulen[115], J.C. Vermeulen[115], C. Vernieri[149], P.J. Verschuuren[91], M. Vessella[99], M.L. Vesterbacka[121], M.C. Vetterli[148,aj], A. Vgenopoulos[158], N. Viaux Maira[142e], T. Vickey[145], O.E. Vickey Boeriu[145], G.H.A. Viehhauser[130], L. Vigani[59b], M. Villa[21b,21a], M. Villaplana Perez[169], E.M. Villhauer[48], E. Vilucchi[49], M.G. Vincter[32], G.S. Virdee[19], A. Vishwakarma[48], C. Vittori[21b,21a], I. Vivarelli[152], V. Vladimirov[173], E. Voevodina[111], M. Vogel[177], P. Vokac[137], J. Von Ahnen[44], E. Von Toerne[22], V. Vorobel[138], K. Vorobev[108], M. Vos[169], J.H. Vossebeld[88], M. Vozak[97], L. Vozdecky[90], N. Vranjes[14], M. Vranjes Milosavljevic[14], V. Vrba[137,*], M. Vreeswijk[115], N.K. Vu[98], R. Vuillermet[34], O.V. Vujinovic[96], I. Vukotic[35], S. Wada[164], C. Wagner[99], W. Wagner[177], S. Wahdan[177], H. Wahlberg[86], R. Wakasa[164], M. Wakida[112], V.M. Walbrecht[111], J. Walder[139], R. Walker[110], S.D. Walker[91], W. Walkowiak[147], A.M. Wang[57], A.Z. Wang[176], C. Wang[58a], C. Wang[58c], H. Wang[16], J. Wang[60a], P. Wang[40], R.-J. Wang[96], R. Wang[57], R. Wang[116], S.M. Wang[154], S. Wang[58b], T. Wang[58a], W.T. Wang[75], W.X. Wang[58a], X. Wang[13c], X. Wang[168], X. Wang[58c], Y. Wang[58a], Z. Wang[102], C. Wanotayaroj[34], A. Warburton[100], C.P. Ward[30], R.J. Ward[19], N. Warrack[55], A.T. Watson[19], M.F. Watson[19], G. Watts[144], B.M. Waugh[92], A.F. Webb[10], C. Weber[27], M.S. Weber[18], S.A. Weber[32], S.M. Weber[59a], C. Wei[58a], Y. Wei[130], A.R. Weidberg[130], J. Weingarten[45], M. Weirich[96], C. Weiser[50], T. Wenaus[27], B. Wendland[45], T. Wengler[34], S. Wenig[34], N. Wermes[22], M. Wessels[59a], K. Whalen[127], A.M. Wharton[87], A.S. White[57], A. White[7], M.J. White[1], D. Whiteson[166], L. Wickremasinghe[128], W. Wiedenmann[176], C. Wiel[46], M. Wielers[139], N. Wieseotte[96], C. Wiglesworth[38], L.A.M. Wiik-Fuchs[50], D.J. Wilbern[124], H.G. Wilkens[34], L.J. Wilkins[91], D.M. Williams[37], H.H. Williams[132], S. Williams[30], S. Willocq[99], P.J. Windischhofer[130], I. Wingerter-Seez[4], F. Winklmeier[127], B.T. Winter[50], M. Wittgen[149], M. Wobisch[93], A. Wolf[96], R. Wölker[130], J. Wollrath[166], M.W. Wolter[82], H. Wolters[135a,135c], V.W.S. Wong[170], A.F. Wongel[44], S.D. Worm[44], B.K. Wosiek[82], K.W. Woźniak[82], K. Wraight[55], J. Wu[13a,13d], S.L. Wu[176], X. Wu[52], Y. Wu[58a], Z. Wu[140,58a], J. Wuerzinger[130], T.R. Wyatt[97], B.M. Wynne[48], S. Xella[38], L. Xia[13c], M. Xia[13b], J. Xiang[60c], X. Xiao[102], M. Xie[58a], X. Xie[58a], I. Xiotidis[152], D. Xu[13a], H. Xu[58a], H. Xu[58a], L. Xu[58a], R. Xu[132], T. Xu[58a], W. Xu[102], Y. Xu[13b], Z. Xu[58b], Z. Xu[149], B. Yabsley[153], S. Yacoob[31a], N. Yamaguchi[85], Y. Yamaguchi[160], M. Yamatani[159], H. Yamauchi[164], T. Yamazaki[16], Y. Yamazaki[80], J. Yan[58c], S. Yan[130], Z. Yan[23], H.J. Yang[58c,58d], H.T. Yang[16], S. Yang[58a], T. Yang[60c], X. Yang[58a], X. Yang[13a], Y. Yang[159], Z. Yang[102,58a], W-M. Yao[16], Y.C. Yap[44], H. Ye[13c], J. Ye[40], S. Ye[27], I. Yeletskikh[77], M.R. Yexley[87], P. Yin[37], K. Yorita[174], K. Yoshihara[76], C.J.S. Young[50], C. Young[149], M. Yuan[102], R. Yuan[58b,i], X. Yue[59a], M. Zaazoua[33e], B. Zabinski[82], G. Zacharis[9], E. Zaid[48], A.M. Zaitsev[118,ae], T. Zakareishvili[155b], N. Zakharchuk[32], S. Zambito[34], D. Zanzi[50], S.V. Zeißner[45], C. Zeitnitz[177], J.C. Zeng[168], D.T. Zenger Jr[24], O. Zenin[118], T. Ženiš[26a], S. Zenz[90], S. Zerradi[33a], D. Zerwas[62], B. Zhang[13c], D.F. Zhang[145], G. Zhang[13b], J. Zhang[5], K. Zhang[13a], L. Zhang[13c], M. Zhang[168], R. Zhang[176], S. Zhang[102], X. Zhang[58c], X. Zhang[58b], Z. Zhang[62], P. Zhao[47], T. Zhao[58b], Y. Zhao[141], Z. Zhao[58a], A. Zhemchugov[77], Z. Zheng[149], D. Zhong[168], B. Zhou[102], C. Zhou[176], H. Zhou[6], N. Zhou[58c], Y. Zhou[6], C.G. Zhu[58b], C. Zhu[13a,13d], H.L. Zhu[58a], H. Zhu[13a], J. Zhu[102], Y. Zhu[58a], X. Zhuang[13a], K. Zhukov[107], V. Zhulanov[117b,117a], D. Zieminska[63], N.I. Zimine[77], S. Zimmermann[50,*], J. Zinsser[59b], M. Ziolkowski[147], L. Živković[14], A. Zoccoli[21b,21a], K. Zoch[52], T.G. Zorbas[145], O. Zormpa[42], W. Zou[37], L. Zwalinski[34].

[1]Department of Physics, University of Adelaide, Adelaide; Australia.
[2]Department of Physics, University of Alberta, Edmonton AB; Canada.
[3(a)]Department of Physics, Ankara University, Ankara;[(b)]Istanbul Aydin University, Application and Research Center for Advanced Studies, Istanbul;[(c)]Division of Physics, TOBB University of Economics and Technology, Ankara; Turkey.
[4]LAPP, Univ. Savoie Mont Blanc, CNRS/IN2P3, Annecy ; France.

[5]High Energy Physics Division, Argonne National Laboratory, Argonne IL; United States of America.
[6]Department of Physics, University of Arizona, Tucson AZ; United States of America.
[7]Department of Physics, University of Texas at Arlington, Arlington TX; United States of America.
[8]Physics Department, National and Kapodistrian University of Athens, Athens; Greece.
[9]Physics Department, National Technical University of Athens, Zografou; Greece.
[10]Department of Physics, University of Texas at Austin, Austin TX; United States of America.
[11(a)]Bahcesehir University, Faculty of Engineering and Natural Sciences, Istanbul;[(b)]Istanbul Bilgi University, Faculty of Engineering and Natural Sciences, Istanbul;[(c)]Department of Physics, Bogazici University, Istanbul;[(d)]Department of Physics Engineering, Gaziantep University, Gaziantep; Turkey.
[12]Institut de Física d'Altes Energies (IFAE), Barcelona Institute of Science and Technology, Barcelona; Spain.
[13(a)]Institute of High Energy Physics, Chinese Academy of Sciences, Beijing;[(b)]Physics Department, Tsinghua University, Beijing;[(c)]Department of Physics, Nanjing University, Nanjing;[(d)]University of Chinese Academy of Science (UCAS), Beijing; China.
[14]Institute of Physics, University of Belgrade, Belgrade; Serbia.
[15]Department for Physics and Technology, University of Bergen, Bergen; Norway.
[16]Physics Division, Lawrence Berkeley National Laboratory and University of California, Berkeley CA; United States of America.
[17]Institut für Physik, Humboldt Universität zu Berlin, Berlin; Germany.
[18]Albert Einstein Center for Fundamental Physics and Laboratory for High Energy Physics, University of Bern, Bern; Switzerland.
[19]School of Physics and Astronomy, University of Birmingham, Birmingham; United Kingdom.
[20(a)]Facultad de Ciencias y Centro de Investigaciónes, Universidad Antonio Nariño, Bogotá;[(b)]Departamento de Física, Universidad Nacional de Colombia, Bogotá; Colombia.
[21(a)]Dipartimento di Fisica e Astronomia A. Righi, Università di Bologna, Bologna;[(b)]INFN Sezione di Bologna; Italy.
[22]Physikalisches Institut, Universität Bonn, Bonn; Germany.
[23]Department of Physics, Boston University, Boston MA; United States of America.
[24]Department of Physics, Brandeis University, Waltham MA; United States of America.
[25(a)]Transilvania University of Brasov, Brasov;[(b)]Horia Hulubei National Institute of Physics and Nuclear Engineering, Bucharest;[(c)]Department of Physics, Alexandru Ioan Cuza University of Iasi, Iasi;[(d)]National Institute for Research and Development of Isotopic and Molecular Technologies, Physics Department, Cluj-Napoca;[(e)]University Politehnica Bucharest, Bucharest;[(f)]West University in Timisoara, Timisoara; Romania.
[26(a)]Faculty of Mathematics, Physics and Informatics, Comenius University, Bratislava;[(b)]Department of Subnuclear Physics, Institute of Experimental Physics of the Slovak Academy of Sciences, Kosice; Slovak Republic.
[27]Physics Department, Brookhaven National Laboratory, Upton NY; United States of America.
[28]Departamento de Física (FCEN) and IFIBA, Universidad de Buenos Aires and CONICET, Buenos Aires; Argentina.
[29]California State University, CA; United States of America.
[30]Cavendish Laboratory, University of Cambridge, Cambridge; United Kingdom.
[31(a)]Department of Physics, University of Cape Town, Cape Town;[(b)]iThemba Labs, Western Cape;[(c)]Department of Mechanical Engineering Science, University of Johannesburg, Johannesburg;[(d)]National Institute of Physics, University of the Philippines Diliman (Philippines);[(e)]University of South Africa, Department of Physics, Pretoria;[(f)]School of Physics, University of the Witwatersrand, Johannesburg; South Africa.

[32]Department of Physics, Carleton University, Ottawa ON; Canada.
[33(a)]Faculté des Sciences Ain Chock, Réseau Universitaire de Physique des Hautes Energies - Université Hassan II, Casablanca;[(b)]Faculté des Sciences, Université Ibn-Tofail, Kénitra;[(c)]Faculté des Sciences Semlalia, Université Cadi Ayyad, LPHEA-Marrakech;[(d)]LPMR, Faculté des Sciences, Université Mohamed Premier, Oujda;[(e)]Faculté des sciences, Université Mohammed V, Rabat;[(f)]Mohammed VI Polytechnic University, Ben Guerir; Morocco.
[34]CERN, Geneva; Switzerland.
[35]Enrico Fermi Institute, University of Chicago, Chicago IL; United States of America.
[36]LPC, Université Clermont Auvergne, CNRS/IN2P3, Clermont-Ferrand; France.
[37]Nevis Laboratory, Columbia University, Irvington NY; United States of America.
[38]Niels Bohr Institute, University of Copenhagen, Copenhagen; Denmark.
[39(a)]Dipartimento di Fisica, Università della Calabria, Rende;[(b)]INFN Gruppo Collegato di Cosenza, Laboratori Nazionali di Frascati; Italy.
[40]Physics Department, Southern Methodist University, Dallas TX; United States of America.
[41]Physics Department, University of Texas at Dallas, Richardson TX; United States of America.
[42]National Centre for Scientific Research "Demokritos", Agia Paraskevi; Greece.
[43(a)]Department of Physics, Stockholm University;[(b)]Oskar Klein Centre, Stockholm; Sweden.
[44]Deutsches Elektronen-Synchrotron DESY, Hamburg and Zeuthen; Germany.
[45]Fakultät Physik , Technische Universität Dortmund, Dortmund; Germany.
[46]Institut für Kern- und Teilchenphysik, Technische Universität Dresden, Dresden; Germany.
[47]Department of Physics, Duke University, Durham NC; United States of America.
[48]SUPA - School of Physics and Astronomy, University of Edinburgh, Edinburgh; United Kingdom.
[49]INFN e Laboratori Nazionali di Frascati, Frascati; Italy.
[50]Physikalisches Institut, Albert-Ludwigs-Universität Freiburg, Freiburg; Germany.
[51]II. Physikalisches Institut, Georg-August-Universität Göttingen, Göttingen; Germany.
[52]Département de Physique Nucléaire et Corpusculaire, Université de Genève, Genève; Switzerland.
[53(a)]Dipartimento di Fisica, Università di Genova, Genova;[(b)]INFN Sezione di Genova; Italy.
[54]II. Physikalisches Institut, Justus-Liebig-Universität Giessen, Giessen; Germany.
[55]SUPA - School of Physics and Astronomy, University of Glasgow, Glasgow; United Kingdom.
[56]LPSC, Université Grenoble Alpes, CNRS/IN2P3, Grenoble INP, Grenoble; France.
[57]Laboratory for Particle Physics and Cosmology, Harvard University, Cambridge MA; United States of America.
[58(a)]Department of Modern Physics and State Key Laboratory of Particle Detection and Electronics, University of Science and Technology of China, Hefei;[(b)]Institute of Frontier and Interdisciplinary Science and Key Laboratory of Particle Physics and Particle Irradiation (MOE), Shandong University, Qingdao;[(c)]School of Physics and Astronomy, Shanghai Jiao Tong University, Key Laboratory for Particle Astrophysics and Cosmology (MOE), SKLPPC, Shanghai;[(d)]Tsung-Dao Lee Institute, Shanghai; China.
[59(a)]Kirchhoff-Institut für Physik, Ruprecht-Karls-Universität Heidelberg, Heidelberg;[(b)]Physikalisches Institut, Ruprecht-Karls-Universität Heidelberg, Heidelberg; Germany.
[60(a)]Department of Physics, Chinese University of Hong Kong, Shatin, N.T., Hong Kong;[(b)]Department of Physics, University of Hong Kong, Hong Kong;[(c)]Department of Physics and Institute for Advanced Study, Hong Kong University of Science and Technology, Clear Water Bay, Kowloon, Hong Kong; China.
[61]Department of Physics, National Tsing Hua University, Hsinchu; Taiwan.
[62]IJCLab, Université Paris-Saclay, CNRS/IN2P3, 91405, Orsay; France.
[63]Department of Physics, Indiana University, Bloomington IN; United States of America.
[64(a)]INFN Gruppo Collegato di Udine, Sezione di Trieste, Udine;[(b)]ICTP, Trieste;[(c)]Dipartimento Politecnico di Ingegneria e Architettura, Università di Udine, Udine; Italy.

[65(a)]INFN Sezione di Lecce;[(b)]Dipartimento di Matematica e Fisica, Università del Salento, Lecce; Italy.
[66(a)]INFN Sezione di Milano;[(b)]Dipartimento di Fisica, Università di Milano, Milano; Italy.
[67(a)]INFN Sezione di Napoli;[(b)]Dipartimento di Fisica, Università di Napoli, Napoli; Italy.
[68(a)]INFN Sezione di Pavia;[(b)]Dipartimento di Fisica, Università di Pavia, Pavia; Italy.
[69(a)]INFN Sezione di Pisa;[(b)]Dipartimento di Fisica E. Fermi, Università di Pisa, Pisa; Italy.
[70(a)]INFN Sezione di Roma;[(b)]Dipartimento di Fisica, Sapienza Università di Roma, Roma; Italy.
[71(a)]INFN Sezione di Roma Tor Vergata;[(b)]Dipartimento di Fisica, Università di Roma Tor Vergata, Roma; Italy.
[72(a)]INFN Sezione di Roma Tre;[(b)]Dipartimento di Matematica e Fisica, Università Roma Tre, Roma; Italy.
[73(a)]INFN-TIFPA;[(b)]Università degli Studi di Trento, Trento; Italy.
[74]Institut für Astro- und Teilchenphysik, Leopold-Franzens-Universität, Innsbruck; Austria.
[75]University of Iowa, Iowa City IA; United States of America.
[76]Department of Physics and Astronomy, Iowa State University, Ames IA; United States of America.
[77]Joint Institute for Nuclear Research, Dubna; Russia.
[78(a)]Departamento de Engenharia Elétrica, Universidade Federal de Juiz de Fora (UFJF), Juiz de Fora;[(b)]Universidade Federal do Rio De Janeiro COPPE/EE/IF, Rio de Janeiro;[(c)]Instituto de Física, Universidade de São Paulo, São Paulo; Brazil.
[79]KEK, High Energy Accelerator Research Organization, Tsukuba; Japan.
[80]Graduate School of Science, Kobe University, Kobe; Japan.
[81(a)]AGH University of Science and Technology, Faculty of Physics and Applied Computer Science, Krakow;[(b)]Marian Smoluchowski Institute of Physics, Jagiellonian University, Krakow; Poland.
[82]Institute of Nuclear Physics Polish Academy of Sciences, Krakow; Poland.
[83]Faculty of Science, Kyoto University, Kyoto; Japan.
[84]Kyoto University of Education, Kyoto; Japan.
[85]Research Center for Advanced Particle Physics and Department of Physics, Kyushu University, Fukuoka ; Japan.
[86]Instituto de Física La Plata, Universidad Nacional de La Plata and CONICET, La Plata; Argentina.
[87]Physics Department, Lancaster University, Lancaster; United Kingdom.
[88]Oliver Lodge Laboratory, University of Liverpool, Liverpool; United Kingdom.
[89]Department of Experimental Particle Physics, Jožef Stefan Institute and Department of Physics, University of Ljubljana, Ljubljana; Slovenia.
[90]School of Physics and Astronomy, Queen Mary University of London, London; United Kingdom.
[91]Department of Physics, Royal Holloway University of London, Egham; United Kingdom.
[92]Department of Physics and Astronomy, University College London, London; United Kingdom.
[93]Louisiana Tech University, Ruston LA; United States of America.
[94]Fysiska institutionen, Lunds universitet, Lund; Sweden.
[95]Departamento de Física Teorica C-15 and CIAFF, Universidad Autónoma de Madrid, Madrid; Spain.
[96]Institut für Physik, Universität Mainz, Mainz; Germany.
[97]School of Physics and Astronomy, University of Manchester, Manchester; United Kingdom.
[98]CPPM, Aix-Marseille Université, CNRS/IN2P3, Marseille; France.
[99]Department of Physics, University of Massachusetts, Amherst MA; United States of America.
[100]Department of Physics, McGill University, Montreal QC; Canada.
[101]School of Physics, University of Melbourne, Victoria; Australia.
[102]Department of Physics, University of Michigan, Ann Arbor MI; United States of America.
[103]Department of Physics and Astronomy, Michigan State University, East Lansing MI; United States of America.

[104]B.I. Stepanov Institute of Physics, National Academy of Sciences of Belarus, Minsk; Belarus.
[105]Research Institute for Nuclear Problems of Byelorussian State University, Minsk; Belarus.
[106]Group of Particle Physics, University of Montreal, Montreal QC; Canada.
[107]P.N. Lebedev Physical Institute of the Russian Academy of Sciences, Moscow; Russia.
[108]National Research Nuclear University MEPhI, Moscow; Russia.
[109]D.V. Skobeltsyn Institute of Nuclear Physics, M.V. Lomonosov Moscow State University, Moscow; Russia.
[110]Fakultät für Physik, Ludwig-Maximilians-Universität München, München; Germany.
[111]Max-Planck-Institut für Physik (Werner-Heisenberg-Institut), München; Germany.
[112]Graduate School of Science and Kobayashi-Maskawa Institute, Nagoya University, Nagoya; Japan.
[113]Department of Physics and Astronomy, University of New Mexico, Albuquerque NM; United States of America.
[114]Institute for Mathematics, Astrophysics and Particle Physics, Radboud University/Nikhef, Nijmegen; Netherlands.
[115]Nikhef National Institute for Subatomic Physics and University of Amsterdam, Amsterdam; Netherlands.
[116]Department of Physics, Northern Illinois University, DeKalb IL; United States of America.
[117(a)]Budker Institute of Nuclear Physics and NSU, SB RAS, Novosibirsk;[(b)]Novosibirsk State University Novosibirsk; Russia.
[118]Institute for High Energy Physics of the National Research Centre Kurchatov Institute, Protvino; Russia.
[119]Institute for Theoretical and Experimental Physics named by A.I. Alikhanov of National Research Centre "Kurchatov Institute", Moscow; Russia.
[120(a)]New York University Abu Dhabi, Abu Dhabi;[(b)]United Arab Emirates University, Al Ain;[(c)]University of Sharjah, Sharjah; United Arab Emirates.
[121]Department of Physics, New York University, New York NY; United States of America.
[122]Ochanomizu University, Otsuka, Bunkyo-ku, Tokyo; Japan.
[123]Ohio State University, Columbus OH; United States of America.
[124]Homer L. Dodge Department of Physics and Astronomy, University of Oklahoma, Norman OK; United States of America.
[125]Department of Physics, Oklahoma State University, Stillwater OK; United States of America.
[126]Palacký University, Joint Laboratory of Optics, Olomouc; Czech Republic.
[127]Institute for Fundamental Science, University of Oregon, Eugene, OR; United States of America.
[128]Graduate School of Science, Osaka University, Osaka; Japan.
[129]Department of Physics, University of Oslo, Oslo; Norway.
[130]Department of Physics, Oxford University, Oxford; United Kingdom.
[131]LPNHE, Sorbonne Université, Université de Paris, CNRS/IN2P3, Paris; France.
[132]Department of Physics, University of Pennsylvania, Philadelphia PA; United States of America.
[133]Konstantinov Nuclear Physics Institute of National Research Centre "Kurchatov Institute", PNPI, St. Petersburg; Russia.
[134]Department of Physics and Astronomy, University of Pittsburgh, Pittsburgh PA; United States of America.
[135(a)]Laboratório de Instrumentação e Física Experimental de Partículas - LIP, Lisboa;[(b)]Departamento de Física, Faculdade de Ciências, Universidade de Lisboa, Lisboa;[(c)]Departamento de Física, Universidade de Coimbra, Coimbra;[(d)]Centro de Física Nuclear da Universidade de Lisboa, Lisboa;[(e)]Departamento de Física, Universidade do Minho, Braga;[(f)]Departamento de Física Teórica y del Cosmos, Universidad de Granada, Granada (Spain);[(g)]Instituto Superior Técnico, Universidade de Lisboa, Lisboa; Portugal.
[136]Institute of Physics of the Czech Academy of Sciences, Prague; Czech Republic.

[137]Czech Technical University in Prague, Prague; Czech Republic.
[138]Charles University, Faculty of Mathematics and Physics, Prague; Czech Republic.
[139]Particle Physics Department, Rutherford Appleton Laboratory, Didcot; United Kingdom.
[140]IRFU, CEA, Université Paris-Saclay, Gif-sur-Yvette; France.
[141]Santa Cruz Institute for Particle Physics, University of California Santa Cruz, Santa Cruz CA; United States of America.
[142(a)]Departamento de Física, Pontificia Universidad Católica de Chile, Santiago;[(b)]Instituto de Investigación Multidisciplinario en Ciencia y Tecnología, y Departamento de Física, Universidad de La Serena;[(c)]Universidad Andres Bello, Department of Physics, Santiago;[(d)]Instituto de Alta Investigación, Universidad de Tarapacá, Arica;[(e)]Departamento de Física, Universidad Técnica Federico Santa María, Valparaíso; Chile.
[143]Universidade Federal de São João del Rei (UFSJ), São João del Rei; Brazil.
[144]Department of Physics, University of Washington, Seattle WA; United States of America.
[145]Department of Physics and Astronomy, University of Sheffield, Sheffield; United Kingdom.
[146]Department of Physics, Shinshu University, Nagano; Japan.
[147]Department Physik, Universität Siegen, Siegen; Germany.
[148]Department of Physics, Simon Fraser University, Burnaby BC; Canada.
[149]SLAC National Accelerator Laboratory, Stanford CA; United States of America.
[150]Department of Physics, Royal Institute of Technology, Stockholm; Sweden.
[151]Departments of Physics and Astronomy, Stony Brook University, Stony Brook NY; United States of America.
[152]Department of Physics and Astronomy, University of Sussex, Brighton; United Kingdom.
[153]School of Physics, University of Sydney, Sydney; Australia.
[154]Institute of Physics, Academia Sinica, Taipei; Taiwan.
[155(a)]E. Andronikashvili Institute of Physics, Iv. Javakhishvili Tbilisi State University, Tbilisi;[(b)]High Energy Physics Institute, Tbilisi State University, Tbilisi; Georgia.
[156]Department of Physics, Technion, Israel Institute of Technology, Haifa; Israel.
[157]Raymond and Beverly Sackler School of Physics and Astronomy, Tel Aviv University, Tel Aviv; Israel.
[158]Department of Physics, Aristotle University of Thessaloniki, Thessaloniki; Greece.
[159]International Center for Elementary Particle Physics and Department of Physics, University of Tokyo, Tokyo; Japan.
[160]Department of Physics, Tokyo Institute of Technology, Tokyo; Japan.
[161]Tomsk State University, Tomsk; Russia.
[162]Department of Physics, University of Toronto, Toronto ON; Canada.
[163(a)]TRIUMF, Vancouver BC;[(b)]Department of Physics and Astronomy, York University, Toronto ON; Canada.
[164]Division of Physics and Tomonaga Center for the History of the Universe, Faculty of Pure and Applied Sciences, University of Tsukuba, Tsukuba; Japan.
[165]Department of Physics and Astronomy, Tufts University, Medford MA; United States of America.
[166]Department of Physics and Astronomy, University of California Irvine, Irvine CA; United States of America.
[167]Department of Physics and Astronomy, University of Uppsala, Uppsala; Sweden.
[168]Department of Physics, University of Illinois, Urbana IL; United States of America.
[169]Instituto de Física Corpuscular (IFIC), Centro Mixto Universidad de Valencia - CSIC, Valencia; Spain.
[170]Department of Physics, University of British Columbia, Vancouver BC; Canada.
[171]Department of Physics and Astronomy, University of Victoria, Victoria BC; Canada.
[172]Fakultät für Physik und Astronomie, Julius-Maximilians-Universität Würzburg, Würzburg; Germany.

[173]Department of Physics, University of Warwick, Coventry; United Kingdom.
[174]Waseda University, Tokyo; Japan.
[175]Department of Particle Physics and Astrophysics, Weizmann Institute of Science, Rehovot; Israel.
[176]Department of Physics, University of Wisconsin, Madison WI; United States of America.
[177]Fakultät für Mathematik und Naturwissenschaften, Fachgruppe Physik, Bergische Universität Wuppertal, Wuppertal; Germany.
[178]Department of Physics, Yale University, New Haven CT; United States of America.
[a] Also at Borough of Manhattan Community College, City University of New York, New York NY; United States of America.
[b] Also at Bruno Kessler Foundation, Trento; Italy.
[c] Also at Center for High Energy Physics, Peking University; China.
[d] Also at Centro Studi e Ricerche Enrico Fermi; Italy.
[e] Also at CERN, Geneva; Switzerland.
[f] Also at Département de Physique Nucléaire et Corpusculaire, Université de Genève, Genève; Switzerland.
[g] Also at Departament de Fisica de la Universitat Autonoma de Barcelona, Barcelona; Spain.
[h] Also at Department of Financial and Management Engineering, University of the Aegean, Chios; Greece.
[i] Also at Department of Physics and Astronomy, Michigan State University, East Lansing MI; United States of America.
[j] Also at Department of Physics and Astronomy, University of Louisville, Louisville, KY; United States of America.
[k] Also at Department of Physics, Ben Gurion University of the Negev, Beer Sheva; Israel.
[l] Also at Department of Physics, California State University, East Bay; United States of America.
[m] Also at Department of Physics, California State University, Fresno; United States of America.
[n] Also at Department of Physics, California State University, Sacramento; United States of America.
[o] Also at Department of Physics, King's College London, London; United Kingdom.
[p] Also at Department of Physics, St. Petersburg State Polytechnical University, St. Petersburg; Russia.
[q] Also at Department of Physics, University of Fribourg, Fribourg; Switzerland.
[r] Also at Faculty of Physics, M.V. Lomonosov Moscow State University, Moscow; Russia.
[s] Also at Faculty of Physics, Sofia University, 'St. Kliment Ohridski', Sofia; Bulgaria.
[t] Also at Graduate School of Science, Osaka University, Osaka; Japan.
[u] Also at Hellenic Open University, Patras; Greece.
[v] Also at Institucio Catalana de Recerca i Estudis Avancats, ICREA, Barcelona; Spain.
[w] Also at Institut für Experimentalphysik, Universität Hamburg, Hamburg; Germany.
[x] Also at Institute for Particle and Nuclear Physics, Wigner Research Centre for Physics, Budapest; Hungary.
[y] Also at Institute of Particle Physics (IPP); Canada.
[z] Also at Institute of Physics, Azerbaijan Academy of Sciences, Baku; Azerbaijan.
[aa] Also at Institute of Theoretical Physics, Ilia State University, Tbilisi; Georgia.
[ab] Also at Instituto de Fisica Teorica, IFT-UAM/CSIC, Madrid; Spain.
[ac] Also at Istanbul University, Dept. of Physics, Istanbul; Turkey.
[ad] Also at Joint Institute for Nuclear Research, Dubna; Russia.
[ae] Also at Moscow Institute of Physics and Technology State University, Dolgoprudny; Russia.
[af] Also at National Research Nuclear University MEPhI, Moscow; Russia.
[ag] Also at Physics Department, An-Najah National University, Nablus; Palestine.
[ah] Also at Physikalisches Institut, Albert-Ludwigs-Universität Freiburg, Freiburg; Germany.
[ai] Also at The City College of New York, New York NY; United States of America.

[aj] Also at TRIUMF, Vancouver BC; Canada.
[ak] Also at Universita di Napoli Parthenope, Napoli; Italy.
[al] Also at University of Chinese Academy of Sciences (UCAS), Beijing; China.
[am] Also at Yeditepe University, Physics Department, Istanbul; Turkey.
[*] Deceased